Light Guidance in Müller Cells of the Vertebrate Retina

Von der Fakultät für Physik und Geowissenschaften
der Universität Leipzig
genehmigte

DISSERTATION

zur Erlangung des akademischen Grades

Doktor der Naturwissenschaften

Dr. rer. nat.

vorgelegt

von Dipl.-Phys. Silke Agte

geboren am 24. Juli 1980 in Halle (Saale)

Gutachter: Prof. Dr. Josef Käs
Prof. Dr. Erez Ribak

Tag der Verleihung: 18.03.2013

Bibliographische Beschreibung

Agte, Silke

Light Guidance in Müller Cells of the Vertebrate Retina

Universität Leipzig, Dissertation

145 S., 187 Lit., 75 Abb., 3 Tab.

Referat

Die Funktionsweise des invertierten Aufbaus der Netzhaut im Wirbeltierauge ist ein altes Rätsel der Wissenschaft. Das beim Sehvorgang auf die Netzhaut einfallende Licht muss erst alle Netzhautschichten durchdringen, bevor es die Photorezeptorzellen erreicht, welche sich auf der lichtabgewandten Seite des Gewebes befinden. Die vorgelagerten Gewebsschichten enthalten zahlreiche lichtstreuende Bestandteile und müssten den Sehvorgang der Wirbeltiere theoretisch negativ beeinflussen. Diese Annahme steht jedoch im Widerspruch zu dem beeindruckenden Sehvermögen der meisten Wirbeltiere. Die Müllerschen Radialgliazellen stellen eine Lösung für diesen scheinbaren Widerspruch dar. Aufgrund der auffälligen morphologischen Struktur dieser Gliazellen, welche die gesamte Dicke der Netzhaut säulenförmig durchspannen, wurde die Hypothese aufgestellt, dass Müllerzellen nach dem Prinzip der Lichtleitung arbeiten und so das Licht zu den Photorezeptoren transportieren. Diese Theorie konnte jedoch bisher noch nicht bewiesen werden, da die bisherigen experimentellen Messmethoden auf der Basis von isolierten Müllerzellen ungeeignet sind, um diese Funktion im lebenden Gewebe nachzuweisen.

Die vorliegende Arbeit beweist erstmalig, dass die Müllerschen Gliazellen als lebende Lichtleiter im Netzhautgewebe funktionieren. Um diese Aufgabe den Müllerzellen eindeutig zuzuordnen, wurde eine neuartige Methode entwickelt, welche gleichzeitig mehrere für den Nachweis unverzichtbare Parameter erfassen kann. Aufgrund einer fluoreszenzbasierten Visualisierung der Müllerzellen in der intakten Netzhaut konnte mit Hilfe eines auf Glasfaseroptik basierenden Aufbaus die Beleuchtung einzelner Müllerzellen erfolgen. Zeitgleich war es möglich, sowohl den Weg des Lichtes von der lichtzugewandten Seite bis zu den Photorezeptoren als auch die Transmission hinter dem Gewebe zu detektieren. Die Komplexität dieses Messverfahrens erlaubte eine detaillierte Charakterisierung des Einflusses der Müllerzelle auf die Streueigenschaften der verschiedenen retinalen Schichten sowie des sich ergebenden Lichtsignals an den Rezeptorzellen. Mittels eines speziellen Analyseverfahrens konnte umfassendes Datenmaterial erhoben und so die Müllerzelle eindeutig als Lichtleiter identifiziert werden. Darauf aufbauend wird in dieser Arbeit außerdem gezeigt, dass alle Müllerzellen gemeinsam und damit in ihrer Gesamtheit mittels ihrer Lichtleitfunktion das an den Photorezeptoren ankommende Lichtmuster beeinflussen, was zu einer verbesserten Bildqualität führt. Dies wird zusätzlich durch morphologische Untersuchungen gestützt, die zeigen, dass die für das Kontrastsehen verantwortlichen Zapfen-Photorezeptorzellen lokal hinter den Müllerzellen angeordnet sind. Demnach ist jeder Zapfen mit einem ihm vorgelagerten Lichtleiter ausgestattet. Zusammenfassend liefert diese Arbeit eine Erklärung, wie trotz des invertierten Aufbaus der Netzhaut die visuelle Information als Grundlage für das Sehen der Wirbeltiere erhalten bleibt.

Contents

List of Figures

List of Tables

1 Introduction

The vertebrate eye is built like a camera with an optical apparatus that focuses the light onto a sensitive film - the retina. There, the photoreceptor cells convert the visual information into nervous signals. These signals are able to be processed by the retinal neurons and finally can be perceived by the visual cortex of the brain (Kandel et al., 1999). However, contrary to the light-sensitive elements of a camera, the photoreceptors are located at the backside of the retina and are obscured by all other cells of the tissue. This construction of the inverted retina poses a mystery for scientists since the incoming light has to pass all retinal layers before it reaches the sensory receptor cells (Goldsmith, 1990). Biological cells are phase objects, in other words, they represent a refractive index landscape irregularly formed by the size, molecular density and shape of the intracellular organelles (Zernike, 1955). From an optical point of view, a spatial variation of refractive indices corresponds to an accumulation of scatterers, so that every interaction of light with a biological sample is principally based on microscopic scattering processes. Thus, the light on its way through the inverted retina would be subject to numerous scattering events causing an immense background noise at the photoreceptor array. In terms of sensory perception, this would lead to a reduction of the signal-to-noise ratio. However, an expected loss of visual information strongly contradicts to the visual performance of vertebrates since most of them have a well-developed contrast vision in daylight and are also sensitive to low amounts of photons in darkness. In particular, a pronounced capability for motion detection is closely linked with the survival of most species (Land and Nilsson, 2002).

Considering this paradoxon, one might wonder why scientists in the 1970's and 1980's only focused onto the optics of photoreceptor neurons without paying attention to the light path in front of them (Enoch, 1963; Tobey and Enoch, 1973; Enoch et al., 1981). Only about 30 years after this boom in photoreceptor optics, a glia researcher came up with the idea that the elongated Müller glial cells might provide an answer for the controversial situation within the retina (Reichenbach and Bringmann, 2010). This delay in time partly arose from the historical progress of neuroscience as research was preferentially concentrated on the function of neurons. Glial cells, the second cell type of the central nervous system, were rather seen as negligible support cells supplying just a passive filling matrix of the nervous tissue. The term 'glia', introduced in 1856 by Rudolf Virchow, derives from the greek word $\gamma\lambda\iota\alpha$ and simply means glue (Virchow, 1856). Hence, Müller cells as main glial cells of the retina remained virtually unexplored from their first description by the German anatomist Heinrich Müller in 1851 until the end of the 20th century when continuously improving methods in cell biology promoted a renaissance of glia research (Müller, 1851; Kandel et al., 1999). Nevertheless, already Müller's description of *"radial cylinders spanning the entire thickness of the retina"* points out the favorable morphology of Müller glial cells to transport light through the tissue to the receptor cells (Figure 1.1).

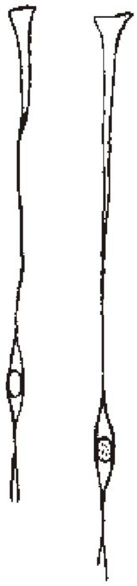

Figure 1.1: Heinrich Müller's original drawing of Müller radial glial cells. (Müller, 1851).

During the past decade, several experiments have shown a particular light permeability of Müller cells which sets them apart from the optical properties of their surrounding neuropil (Franze et al., 2007). Turning to the question of the underlying physical principle, it was the striking similarity with fiber optic cables in a plate which led scientists to assume that Müller cells act as living wave guides within the retinal tissue. However, none of the known approaches fulfilled all requirements to prove this hypothesis. This also includes the experiment from Franze et al. (2007) where it was shown that individual Müller cells, placed between two glass fibers of a modified dual-beam laser trap, are able to guide the incoming light from an input to an opposing output fiber. Generally, isolated cells embedded within homogeneous fluids do not experience the complex optical landscape of their natural environment which in turn considerably affects their optic behavior. In particular, a light guiding mechanism of a cell would not only depend on the optical properties of the single cell itself but also on its proximate surrounding material. Furthermore, if no reliable data about the microscopic refractive index distributions of the surrounding medium exist, as it is true for the various retinal tissue compartments, there is no possibility to mimic the actual conditions. To put it in other words, any arbitrary elongated cell subjected to an appropriate environment would act as light guide.

The main focus of the present thesis is to find evidence that living Müller cells within their original, optically sound, retinal tissue operate on the principle of light guidance. In order to study the retina as scattering tissue and to characterize the influence of Müller cells within each retinal layer, a new experimental setup was developed (Agte et al., 2011). The novel technique allows a simultaneous detection of all necessary information regarding the incoming, the propagating and the transmitted light and thus provides a comprehensive picture of the optical nature of all cellular components constituting the retina. The work further addresses the interesting question whether the entirety of Müller cells affects the actual visual stimulation pattern arriving at the photoreceptors. This, together with a morphological study of the spatial relationship between Müller cells and photoreceptors, provides approaches how the Müller cell light guidance contributes to the visual process of vertebrates (Agte et al., 2011).

2 Background

In the following chapter, I will give an overview about the interaction of light with biological objects. First, it provides an overall description of the microscopic scattering process as underlying mechanism of all macroscopic phenomena occurring if visible electromagnetic radiation impinges a material. Then, the microscopic composition of biological cells is introduced whereas special attention is paid to the size and the shape of subcellular structures. In line with this, the fundamental idea of light scattering on different sized particles is presented before detailed insights into the optic behavior of organelles, cells and tissues are given. Finally, the cellular composition of the inverted vertebrate retina is introduced and the main tasks of the visual system are highlighted. Known optical properties of photoreceptors and Müller cells are summarized.

2.1 Optical Properties of Cells and Tissue

2.1.1 Propagation of Light in Matter

If light is incident on matter, several basic phenomena are observed (Figure 2.1). Before light enters the medium, the incident light intensity is reduced by reflection at the surface. The remaining part gets refracted, passes the material and is detected as transmitted light. With respect to the incoming light, the transmitted light intensity is attenuated because it is partially absorbed and scattered inside the medium. The scattered light can be detected laterally. Considering all described phenomena, the following intensity balance results from reflection, absorption, scattering and transmission

$$I_0 = I_\mathrm{R} + I_\mathrm{A} + I_\mathrm{S} + I_\mathrm{T}, \tag{2.1}$$

where I_0 is the intensity of the incident light, I_R the intensity of the reflected light, I_A the intensity of the absorbed light, I_S the intensity of the scattered light and I_T the intensity of the transmitted light. Some general formulations like the law of refraction appear to be simple and plausible as they are well described by ray optic models. These models are based on a simplified macroscopic perspective which allows a basic understanding of reflection and refraction but fail in a complete description of many optical phenomena like scattering, absorption, interference and diffraction. However, to study complex tasks as the propagation of light through a biological object, one must ask for a basic principle which accounts for all macroscopic phenomena.

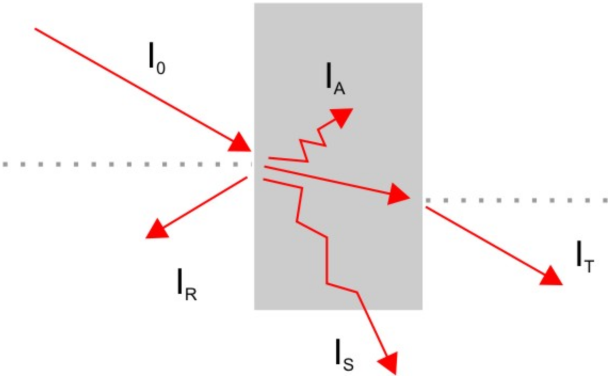

Figure 2.1: Propagation of light through a medium on a macroscopic level. (I_0, intensity of the incident light; I_R, intensity of the reflected light; I_A intensity of the absorbed light; I_S, intensity of the scattered light; I_T, intensity of the transmitted light)

To comply with those requirements, the propagation of light in matter has to be considered as an interaction of electromagnetic radiation with the structure of atoms constituting the material. A first insight into this behavior is given by the Rayleigh theory (Bergmann and Schaefer, 1998; Jackson, 1999) that describes the interaction of an electromagnetic wave with isolated, dielectric and spherical particles whose size d is much smaller than the wavelength of light ($d < \lambda/20$), such as single atoms or molecules ($d \approx 0.1$ nm). After Maxwell, light consists of oscillating electric and magnetic fields which are dependent in time and space

$$\mathbf{E}(\mathbf{r},t) = Re[\mathbf{E}_0 e^{i(\mathbf{kr}-wt)}] = \mathbf{E}_0 cos(\mathbf{kr}-wt) \tag{2.2}$$

$$\mathbf{B}(\mathbf{r},t) = Re[\mathbf{B}_0 e^{i(\mathbf{kr}-wt)}] = \mathbf{B}_0 cos(\mathbf{kr}-wt) \tag{2.3}$$

with $\mathbf{E}_0$ as electric field amplitude, $\mathbf{B}_0$ as magnetic field amplitude, w as angular frequency and $\mathbf{k}$ as wave vector (Jackson, 1999). Each atom is composed of a positively charged nucleus surrounded by a shell of negatively charged electrons whereas virtually all the mass of the atom is concentrated in the nucleus since the mass of the electrons is negligible. Thus, an oscillating electric field of the incident light forces the electron cloud to vibrate with respect to the positive nucleus that remains more or less at rest (Hoppe et al., 1982). This periodic separation of negative and positive charges induces an electric dipole moment $\mathbf{p}$ which is the vector product of the electric polarizability α of the atom (or molecule) and the electric field $\mathbf{E}$ of light

$$\mathbf{p} = \alpha \times \mathbf{E}. \tag{2.4}$$

By using equation 2.2, the dipole moment $\mathbf{p}$ is described by

$$\mathbf{p} = Re[\alpha \times \mathbf{E}_0 e^{i(\mathbf{kr}-wt)}] = \alpha \mathbf{E}_0 cos(\mathbf{kr} - wt). \tag{2.5}$$

As a result, the particle behaves like an oscillating dipole which immediately starts to radiate. The particle represents a source of a new electric field emitting light isotropically in all directions perpendicular to the E-vector (Figure 2.2). In other words, this process can be seen as a microscopic scattering event as an incoming photon gets absorbed and without delay a new photon is re-emitted in a different direction (Hoppe et al., 1982; Hecht, 2002). The electric field strength $\mathbf{E}_\mathrm{S}$ of this dipole radiation is defined as

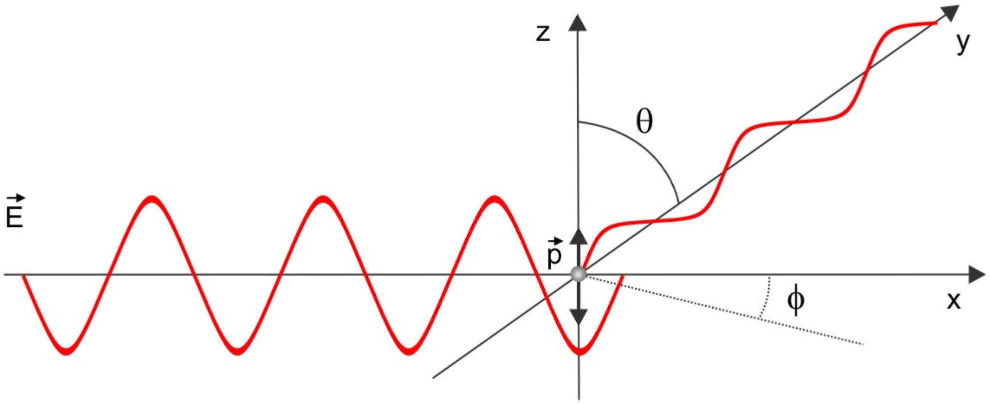

Figure 2.2: The microscopic scattering process. All macroscopic interactions of light with matter occur due to scattering events on a microscopic level with the atomic structure of the material, i.e. with particles much smaller than the wavelength of light ($d < \lambda/20$). The oscillating electric field $\mathbf{E}$ of an electromagnetic wave induces a dipole moment $\mathbf{p}$ in the particle. The particle immediately emits the light with the radiation characteristic of a Hertzian dipole. (θ, scattering angle; ϕ, azimuth angle) Image adapted from Hoppe et al. (1982).

$$\mathbf{E}_\mathrm{S} = \frac{d^2\mathbf{p}}{dt^2} \tag{2.6}$$

which reveals

$$\mathbf{E}_\mathrm{S} = \frac{4\pi^2 \alpha \mathbf{E}_0 sin\theta}{r\lambda^2} cos 2\pi \left(\nu t - \frac{x}{\lambda} \right). \tag{2.7}$$

The induced dipole oscillates with $sin\theta$ while θ describes the angle between the dipole axis and the direction of the light scattering (Figure 2.2). It should be noted, the frequency ν and wavelength λ of the emitted light are equal to the incident light, for this reason the process is called elastic scattering. Most setups that investigate light scattering are typically only sensitive to the scattering intensity I_{S}. The scattering intensity caused by scattering of light on a small isolated sphere $I_{\mathrm{S}}^{\mathrm{Single}}$ is proportional to the squared amplitude of the field strength E_{S}

$$I_{\mathrm{S}}^{\mathrm{Single}} = E_{\mathrm{S}}^2. \tag{2.8}$$

The ratio between $I_{\mathrm{S}}^{\mathrm{Single}}$ and the intensity of the incoming light I_0 reveals

$$\frac{I_{\mathrm{S}}^{\mathrm{Single}}}{I_0} = \frac{16\pi^4\alpha^2 sin^2\theta}{\lambda^4 r^2} \tag{2.9}$$

which is characterized by its strong wavelength dependence as it is proportional to the inverse fourth power of λ (Hoppe et al., 1982). Furthermore, the distribution of the light scattering depends on θ but not on the azimuth angle ϕ (Figure 2.3). For non-polarized light as sunlight equation 2.9 is changed to

$$\frac{I_{\mathrm{S}}^{\mathrm{Single}}}{I_0} = \frac{8\pi^4\alpha^2}{\lambda^4 r^2}(1 + cos^2\phi). \tag{2.10}$$

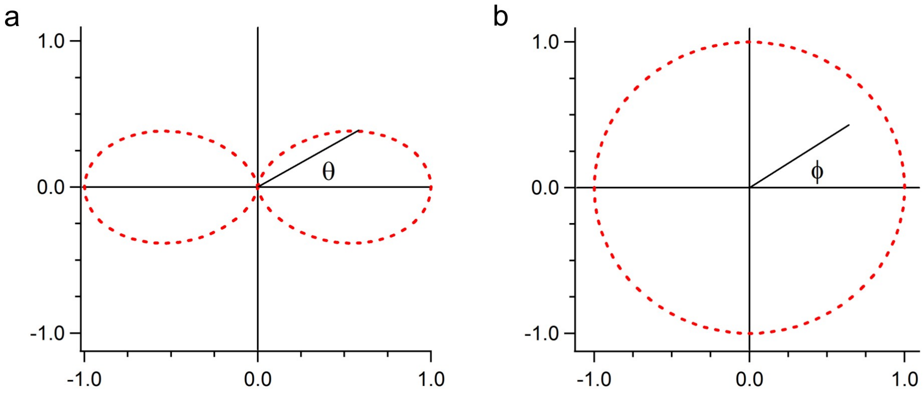

Figure 2.3: Intensity distribution of the scattered light. (a) The intensity scattered off a small particle ($d < \lambda/20$) in dependence on the angle θ. (b) In the azimuthal plane the dipole emits, i.e. the particle scatters, the light isotropically in all directions (ϕ, azimuth angle).

In conclusion, all macroscopic phenomena like reflection, refraction, absorption, scattering, transmission and diffraction of light in matter are based on scattering processes on a microscopic level (Hecht, 2002).

2.1.2 The Biological Tissue from a Microscopic View

Up to now, matter was considered an ensemble of scatterers whose scattering cross section is very small compared to the wavelength of the incident light, so that the electric field is homogeneously distributed over each particle. Additionally, a sufficient separation of the particles inside the material was assumed, thus, light scattered from neighboring particles do not further interact. This model of independent point sources, known as Rayleigh scattering, well describes the interaction of light with particles dissolved in highly diluted aqueous solutions as for example collagen fibril (Silver and Birk, 1984), membrane (Schmidt and Rayfield, 1994) or protein suspensions (Elshereef et al., 2010).

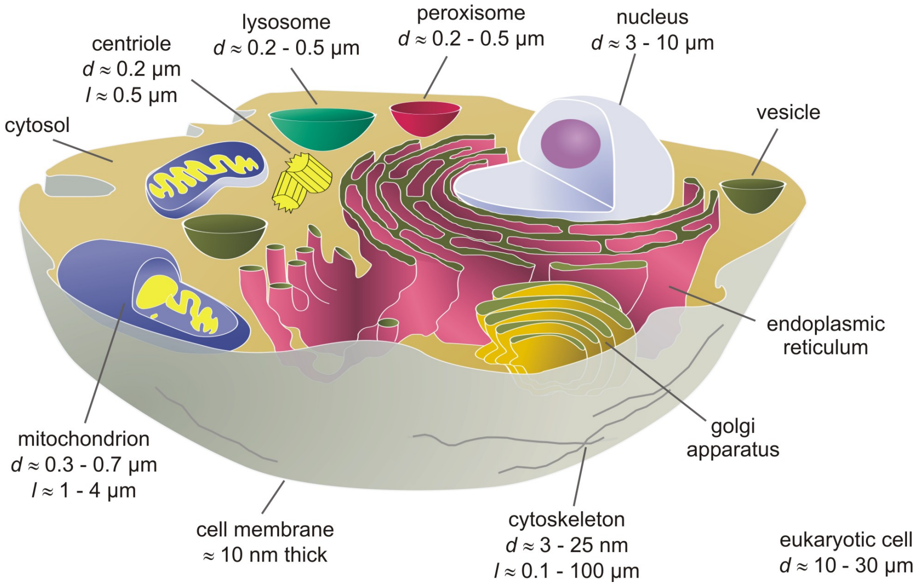

Figure 2.4: Typical structure of an eukaryotic cell. The size of the cellular structures are indicated by their diameter d and their length l (references are found in the text). Image from Wikimedia Commons, slightly modified.

However, biological tissues consist of a cellular structure which, depending on the function and localization of the tissue, can vary greatly in its composition and organization. The cell as basic functional subunit of each tissue is generally built up of the same main constituents as shown for a generalized eukaryotic cell in Figure 2.4. Eukaryotic cells are usually between 10 - 30 µm in diameter (Alberts et al., 2002). Their cell membrane, an approximately 10 nm thick double layer of phospholipids with embedded proteins, separates the interior of the cell from the extracellular fluid (Lehninger et al., 2008). In order to maintain the vitality of the organism, the cell is composed of multiple structures each responsible for its own specific task. The most obvious organelle is the control center of the cell, the nucleus. The size of the nucleus varies in relation to the cell size and is typically in the order of 3 - 10 µm in diameter (Mourant et al., 1998; Alberts et al., 2002). It is surrounded by a phospholipid bilayer. Another membrane-enclosed organelle is the mitochondrion which is often called the cell's power plant as its large volume of folded inner membranes provides the chemical energy for the cell. Depending on the energy metabolism of the tissue type, the number of mitochondria per cell ranges from one to more than thousand (Lehninger et al., 2008). Mitochondria have an ellipsoidal shape with a length of approximately 1 - 4 µm and a diameter of around 0.3 - 0.7 µm which is close to the wavelength of light (Palade, 1953). Spherical vesicles like lysosomes and peroxisomes are similar in size with diameters of about 0.2 - 0.5 µm (Alberts et al., 2002). The Golgi apparatus and the endoplasmic reticulum have no well-defined shape, their wide structures mainly consist of lipid membranes (Alberts et al., 2002). All cell organelles are embedded in a fluid intracellular matrix whose aqueous cytosol is traversed by a meshwork of biopolymers, the cytoskeleton. In eukaryotic cells the cytoskeleton is formed by three kinds of thread-like polymer filaments that are of nanometers in width and micrometers in length: actin filaments (diameter 3 - 6 nm, length 0.1 - 50 µm), microtubules (diameter 20 - 25 nm, length 1 - 100 µm) and intermediate filaments (diameter 8 - 10 nm, several micrometers in length) (Moores et al., 2006; Kreplak and Fudge, 2007; Brunner, 2011). The microtubuli grow out from two cylindrical centrioles (diameter about 0.2 µm, length about 0.5 µm) which play a crucial role in cell division. In general, the cytoskeleton is responsible for intracellular transport mechanisms and the mechanical strength of the cell (Lodish et al., 2000; Alberts et al., 2002).

2.1.3 Scattering of Light on Different Sized Particles

From a physical point of view, a biological tissue can be treated as a composition of different sized scatteres which inevitably raises the question: How does the size of an individual particle of the tissue influence the interaction of light and matter? And further, how does this interaction affect the optical properties of the entire tissue which is of fundamental importance for optical relevant tissues as for example the retina in the eye?

In order to answer these questions, I will give a first insight into a scattering process between an electromagnetic wave and a particle whose size is in the order of the wavelength of light. Figure 2.5 (a) illustrates a transmission electron micrograph of neuronal processes in the vertebrate retina which are approximately 500 nm in diameter (Palanker et al., 2004). If a light wave impinges an individual structure, electrons in distant areas of the particle are excited by different phases of the incoming electric field, so that light waves originating from multiple dipoles have constant phase relations (Figure 2.5 b). These coherent waves finally lead to interference effects dependent upon the geometrical dimensions of the particle and the direction of the light scattering (Hoppe et al., 1982). In other words, the resulting scattered field represents a superposition of all scattered wavelets. In forward direction ($\theta = 0$), i.e. in the direction of the incoming beam, no optical path differences between the wavelets occur, the amplitudes sum up and the scattered light intensity gets enhanced by constructive interference (Bohren and Huffman, 1983). For small scattering angles ($\theta = \theta_1$), the waves are no longer in phase with each other and destructive interference reduces the light intensity. Accompanied by that, large scattering angles further reduce the total scattered field amplitude up to its minimum at 180° (Hoppe et al., 1982).

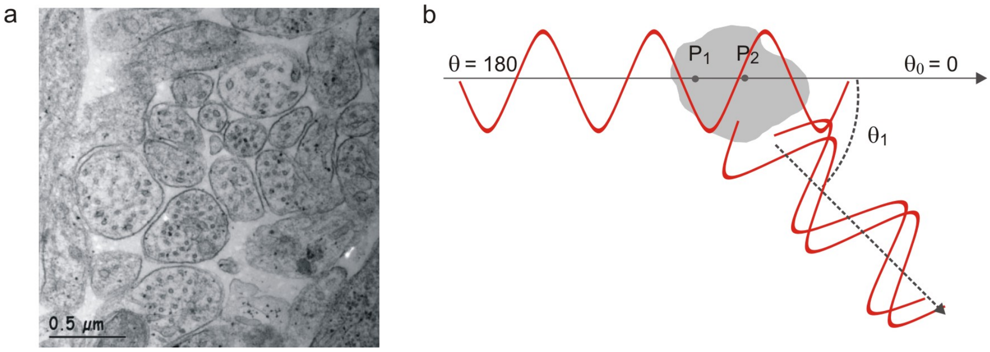

Figure 2.5: Scattering of light on large particles. (a) Cross section of neuronal processes (dendrites or axons) in the retina, recorded by transmission electron microscopy. The size of individual processes is in the order of the visible wavelength. Image taken from Palanker et al. (2004). (b) Schemata of the light scattering on a particle whose diameter is approximately $\lambda/2$. An increase of the scattering angle θ is accompanied by enhanced destructive interference effects. Image adapted from Hoppe et al. (1982).

With respect to Figure 2.5, one can imagine that scattering of light in matter requires a complex optical description considering the size of the particles and in particular the size of the particles with respect to the wavelength of light. In 1908, Gustav Mie (Mie, 1908) firstly studied the scattering processes on particles of arbitrary sizes by using Maxwell's electromagnetic theory (Stratton, 2007). The theoretical analysis of Mie provides the formal solutions of Maxwell's equations by using the appropriate boundary conditions, it completely characterizes the scattering of a plane electromagnetic wave on a spherical dielectric object as it is equally applicable to spheres of all sizes and for radiation at all wavelengths (Mie, 1908; Hulst, 1981). The above mentioned model of a Rayleigh scatterer is included in Mie's theory as it represents an approximation of the formulations for particles with dimensions much smaller than the wavelength of light (Hulst, 1981; Bohren and Huffman, 1983). The scattering processes of light, coming from direction $\mathbf{s}$, with single homogeneous spheres of different sizes are demonstrated in Figure 2.6. The new directions in which the light is travelled after the scattering event do not generally occur with equal probability. Mathematically, the angular probability of light being scattered in direction $\mathbf{s'}$ is expressed by the normalized phase function $p(\mathbf{s}, \mathbf{s'})$. For tractability, it is usually assumed that $p(\mathbf{s}, \mathbf{s'})$ is independent from the incident direction $\mathbf{s}$ and thus only a function of the angle θ between $\mathbf{s}$ and $\mathbf{s'}$ (Cheong et al., 1990). Therefore, the phase function which characterizes the angular intensity distribution for a single scattering event can be described by the cosine of the scattering angle θ (Schmidt, 1999)

$$p(\mathbf{s}, \mathbf{s}') = p(cos\theta). \tag{2.11}$$

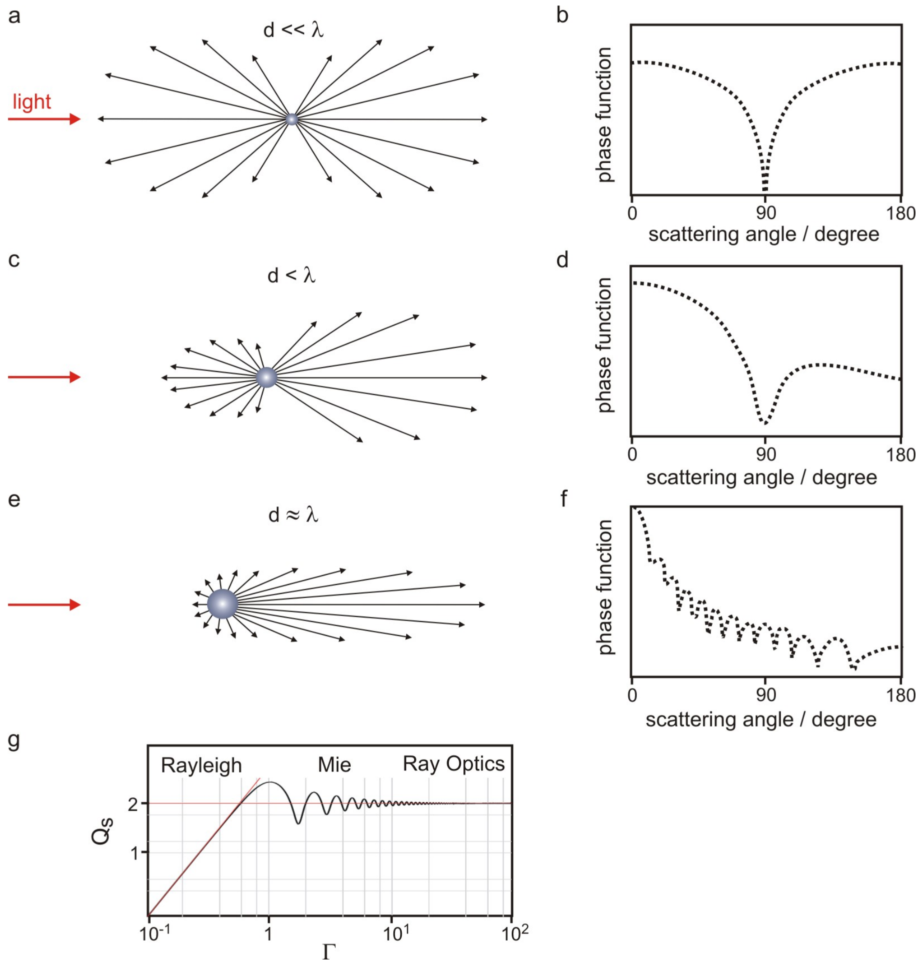

Figure 2.6: Scattering of light in dependence on the particle size. (a-f) Polar diagrams of the scattered light intensity and phase functions for homogeneous spheres with diameter d. (a, b) For $d \ll \lambda$ the particle can be treated as Rayleigh scatterer. (c-f) If d increases, the backward scattering gets reduced by destructive interferences. (g) For $d \gg \lambda$, ray optics can be used to describe the scattering process. The three scattering regimes of Mie theory are summarized in a diagram which shows the scattering efficiency Q_s (ratio between scattering cross section σ_s and the geometrical cross section πr^2) in dependence on the Mie parameter Γ. Images adapted from Mie (1908), Hielscher et al. (1997) and Wikimedia Commons.

Figure 2.6 (b) illustrates the phase function for a Rayleigh scatterer ($d \ll \lambda$) in dependence on the scattering angle θ. The light is equally scattered in forward (0°) and backward direction (180°) as seen by the symmetric scattering profile in the polar diagram (compare Figure 2.6 a with 2.3 a). In contrast, the light scattering of a particle which is departing from the Rayleigh regime, but whose size is still below the wavelength of light ($d < \lambda$), is mainly attenuated in backward direction while the forward intensity dominates (Figure 2.6, c and d). In Mie's theory, this case falls into the lower range of the so-called Mie regime. Particles with sizes close to the wavelength of light ($d \approx \lambda$) are well within this regime. Here, the forward peaked scattering is greatly enhanced and gradually decreases from 0° to 180° (Figure 2.6, e and f). Characteristic for Mie scattering are also the tremendous oscillations in the curve progression which result from the constructive and destructive interference effects along the different scattering directions, as described in Figure 2.5 (Bohren and Huffman, 1983). Thus, an analysis of light scattering within this regime requires complex theoretical calculations (Mie, 1908; Stratton, 2007). In addition, another relatively simple solution of Mie theory is given for particles much larger than the wavelength of light ($d \gg \lambda$), in this limit, classical geometrical optics is used to conveniently describe the behavior of light in matter in terms of rays. Generally, based on the ratio between particle size and wavelength, the scattering processes can be categorized in three different regimes of Mie theory. This ratio is described as the Mie or size parameter

$$\Gamma = k\lambda = \frac{2\pi a}{\lambda} \tag{2.12}$$

with k as wave number and a as particle size ($a = d$, with d as diameter for spheres). Figure 2.6 (h) illustrates the scattering efficiency Q_{s}, i.e. the scattering cross section σ_s normalized by the geometric cross section πr^2 (r, sphere radius), of a weakly absorbing homogeneous sphere as a function of the Mie parameter. The curve is clearly separated in three domains (Hulst, 1981):

- Rayleigh scattering: $\Gamma \ll 1$
- Mie scattering: $0.5 < \Gamma < 10$
- Geometrical optics: $\Gamma \gg 1$.

For a Rayleigh scatterer, Q_{s} rapidly rises with Γ which is due to the fact that σ_{s} varies with the sixth power of d and the inverse fourth power of λ. Particles of the Mie regime become more efficient light scatterers since light interacts with the particle over a cross-sectional area larger than the geometric cross section ($Q_{\mathrm{s}} > 1$). This is caused by interferences between the scattered and diffracted waves as indicated by the maxima and minima. For larger values of Γ within the ray optics regime these oscillations decay and Q_{s} asymptotically approaches the limiting value 2. Here, the narrow forward scattering is determined by light diffracted around the object and light that is directly incident on it. This is contrary to predictions from geometrical optics and thus it is referred to as extinction paradoxon, for more details see Hulst (1981) and Bohren and Huffman (1983). In general, it should be noted that particles of different sizes are able to scatter light with different angular distributions and with varying degrees of efficiency.

2.1.4 Light Scattering in Biological Tissue

In order to understand the propagation of light in a biological tissue, the underlying mechanisms need to be considered on a microscopic level (see section 2.1.1). As described in section 2.1.2, a tissue or its cellular subunits are composed of structural inhomogeneities such as membranes and organelles (Figures 2.4 and 2.7 a). Usually, morphological inhomogeneities are accompanied by optical inhomogeneities, for example, one can easily imagine that the aqueous cytosol has a lower optical density than the membrane-filled mitochondria. In general, if light travels through a medium, it slows down in dependence on the optical density of the material. This reduction in speed is used to characterize the medium by the index of refraction

$$n = \frac{c}{v} \tag{2.13}$$

where c is the speed of light in vacuum and v the speed of light in the medium. Consequently, a biological tissue can be treated as spatial distribution of the refractive index whose magnitude and spatial extent arise from the physical composition and size of the objects that make up the cell (Drezek et al., 1999). When light passes such an optically inhomogeneous tissue, it gets scattered due to the refractive index mismatches occurring at the boundaries between the intracellular structures as for example between the cytosol and the lipid membranes of the organelles (Hollis, 2002). In addition to scattering, some parts of light will always be absorbed by the material. A complex notation of the refractive index takes this into account

$$N = n + in'. \tag{2.14}$$

The refractive index of biological tissues is typically around 1.4 (Bolin et al., 1989). It represents a mean value of all refractive indices on the microscopic level that varies between 1.33 for water and 1.55 for lipids and proteins (Bennett et al., 1951; Franze, 2007). Measurements revealed slighty different values for the index of refraction for some cellular components such as the nucleus ($n \approx 1.39$; Brunsting and Mullaney, 1974), the mitochondria ($n \approx 1.41$; Liu et al., 1996) and the cytoplasm ($n \approx 1.38$; Brunsting and Mullaney, 1974). These differences are sufficient to make them potential scattering objects. As schematically illustrated for spheres in Figure 2.6, each cellular scattering object will give rise for its own scattering phase function (see equation 2.11). On a macroscopic scale, all individual phase functions are averaged and result in a spatially independent mean value (Beuthan et al., 1996), whereas the contribution of each scattering object depends on its individual scattering properties and its relative concentration in the tissue (Hollis, 2002). The use of mean optical parameters is based upon transport theory which is most popular in tissue optics as it assumes a homogeneous sample (Cheong et al., 1990). For example, the scattering cross section σ_{s} describes the effective surface of a microscopic particle from which the light gets scattered. To determine the macroscopic scattering coefficient μ_{s} of a tissue, the particle's scattering cross section needs to be multiplied with the density ρ of the particle

$$\mu_{\mathrm{s}} = \rho\sigma_{\mathrm{s}}. \tag{2.15}$$

This is equivalently true for the absorption coefficient μ_a considering the fraction of light absorbed by the medium

$$\mu_{\mathrm{a}} = \rho\sigma_{\mathrm{a}}. \tag{2.16}$$

Consequently, the total attenuation coefficient μ_{t} is given by

$$\mu_{\mathrm{t}} = \mu_{\mathrm{s}} + \mu_{\mathrm{a}}. \tag{2.17}$$

In other words, if light travels through a medium, the incident light intensity I_0 will be attenuated by scattering and absorption. Mathematically, this is expressed by

$$I = I_0 e^{-\mu_{\mathrm{t}} x} \tag{2.18}$$

where x denotes the path length and I the transmitted light intensity. The averaged phase function p of a medium is expressed by the normalized differential scattering coefficient

$$p(cos\theta) = \frac{1}{\mu_{\mathrm{s}}} d\mu_{\mathrm{s}}(cos\theta) \tag{2.19}$$

with θ as scattering angle between the incident direction **s** and the scattered direction **s'** (see section 2.1.3), so that

$$\int_{-1}^{1} p(cos\theta) dcos\theta = 1. \tag{2.20}$$

The phase function is usually characterized by the mean cosine of the scattering angle θ known as the anisotropy factor g with

$$\int_{-1}^{1} p(cos\theta) cos\theta dcos\theta = g \tag{2.21}$$

which implies the assymmetry of the scattering. It ranges between g = -1 for complete backward, and $g = 1$ for complete forward scattering while $g = 0$ corresponds to isotropic scattering processes. An expression for an effective scattering of light in a medium should include both, the scattering coefficient μ_s and the anisotropy factor g. The reduced scattering coefficient μ'_s combines these properties as follows

$$\mu'_\mathrm{s} = (1 - g)\mu_\mathrm{s} \tag{2.22}$$

where its reciprocal $1/\mu'_\mathrm{s}$ defines the reduced mean free path length. Consequently, the reduced attenuation coefficient is given by

$$\mu'_\mathrm{t} = \mu'_\mathrm{s} + \mu_\mathrm{a} \tag{2.23}$$

with $1/\mu'_\mathrm{t}$ as total mean free path (Hollis, 2002). Finally, a measurement of the optical parameters such as the scattering phase function p, the anisotropy factor g or the reduced scattering coefficient μ'_s offer the possibility to study the optical properties of biological tissues.

An extensive review, published in 1990 by Cheong et al. (1990), gave a first overall picture of the optical parameters measured by different methods on multiple types of tissues. Comparing the values of ex-vivo and in-vivo samples, it became very clear that the preparation method, i.e. the physiological state of the sample, strongly influences the interaction with light. Additionally, in most tissues absorption of light could be neglected, the absorption coefficient μ_a was usually much smaller than the scattering coefficient μ_s

$$\mu_\mathrm{a} \ll \mu_\mathrm{s}, \tag{2.24}$$

hence it will be ignored in the following. Furthermore, the anisotropy factor of all examined tissues was typically found between

$$0.69 < g < 0.99. \tag{2.25}$$

For example, the g-value for brain tissue is around 0.95 (Flock et al., 1987; Zee et al., 1993). Consequently, biological tissues preferably scatter in forward direction.

Insights into the optic behavior of the intracellular structures were given by several studies carried out on liver tissue because of its unusually high mitochondria volume fraction of approximately 23 % (Beauvoit et al., 1994; Beauvoit et al., 1995; Beauvoit and Chance, 1998). Each hepatocyte cell contains around 1000 - 2000 mitochondria (Loud, 1968; Alberts et al., 2002). Theoretical Mie calculations, based on experimental data from blood-free liver tissue, hepatocyte suspensions and isolated mitochondria, revealed that the liver light scattering was primarily evoked by its mitochondrial content (Beauvoit et al., 1994). In a later publication, the reduced scattering coefficient was shown to be proportional to the mitochondrial fraction of various rat tissue types (Beauvoit et al., 1995). The skeletal muscle and tumor tissues exhibited a low μ_s' due to their small number of mitochondria whereas a higher percental volume fraction of 8 % in the brain and 28 % in the liver led to a corresponding increase in μ_s' (Figure 2.7 b). The value for white adipose tissue (WAT) was excluded from this linear behavior which might be attributed to the huge amount of high refractive lipid droplets in the cellular volume (Loncar et al., 1988; Bolin et al., 1989). They also investigated the light scattering in dependence on the density of the cells, i.e. on the DNA content of the tissue. As a result, no correlation between μ_s' and the cell density was observed.

In order to analyze the influence of other organelles like the endoplasmic reticulum, lysosomes or peroxisomes, Beauvoit and Chance (1998) used specific drugs to induce a morphological change of the respective organelle. The data confirmed that light propagation is sensitive to such structures. Finally, Mie calculations based upon measurements of g and $\mu_s'(\lambda)$, carried out by Nilsson et al. (1998), determined the average diameter for scattering particles in the liver tissue to be about 0.6 µm. This size is consistent with mitochondria, however it also corresponds to lysosomes and peroxisomes (Figure 2.4) which is of importance for other types of mammalian tissue where mitochondria usually account for a significantly smaller fraction of the cell volume than in hepatocytes.

Mourant et al. (1998) combined experimental data from mammalian cell suspensions with simulations from Mie theory. In contrast to Nilsson et al. (1998), the analysis revealed that the volume of the scattering particles is equivalent to spheres with diameters ranging from about 0.4 to 2 µm. This relatively broad range of scatterer sizes is consistent with the narrow distribution around 0.6 µm for liver tissue as it reflects the uniform organelle composition in hepatocytes caused by numerous mitochondria. To further investigate the scattering properties of the cellular structures, they analyzed the phase functions of cell, nuclei and mitochondria suspensions. As expected from Mie theory (Figure 2.6), particles with dimensions equal or larger than the wavelength of light are forward scatters, consequently, all three phase functions show higher scattering intensities at small angles whereas the angular distribution is sensitive to the size of the particles (Figure 2.7 c). The large nuclei cause a more forward peaked scattering than the small-sized mitochondria. In addition, it should be noted that the curves for the cells and the nuclei are almost identical. In accordance with the results from Beauvoit et al. (1995), the surface of the cell seems to play only a minor role in the angular distribution of light scattering. This observation was confirmed by a later study on multicellular spheroids from Mourant et al.

(2002a) which has shown that neither the cell shape, nor cell-cell contacts influence the measured phase functions.

During the past decade, many people further analyzed the optical properties of intracellular structures. In particular, the modification of the cell morphology, followed by a subsequent measurement of the evoked changes in light scattering, turned out to be a very useful experimental approach to study the scattering of light at specific cell structures. For example, Mourant et al. (2000) quantified the contribution of the organelles by experiments on cells and nuclei at different stages of growth. They found that in an angular range above 40° roughly 55 % of the light scattering originates from intracellular structures while the nucleus contributes up to 40 % to the total amount of scattering. In addition,

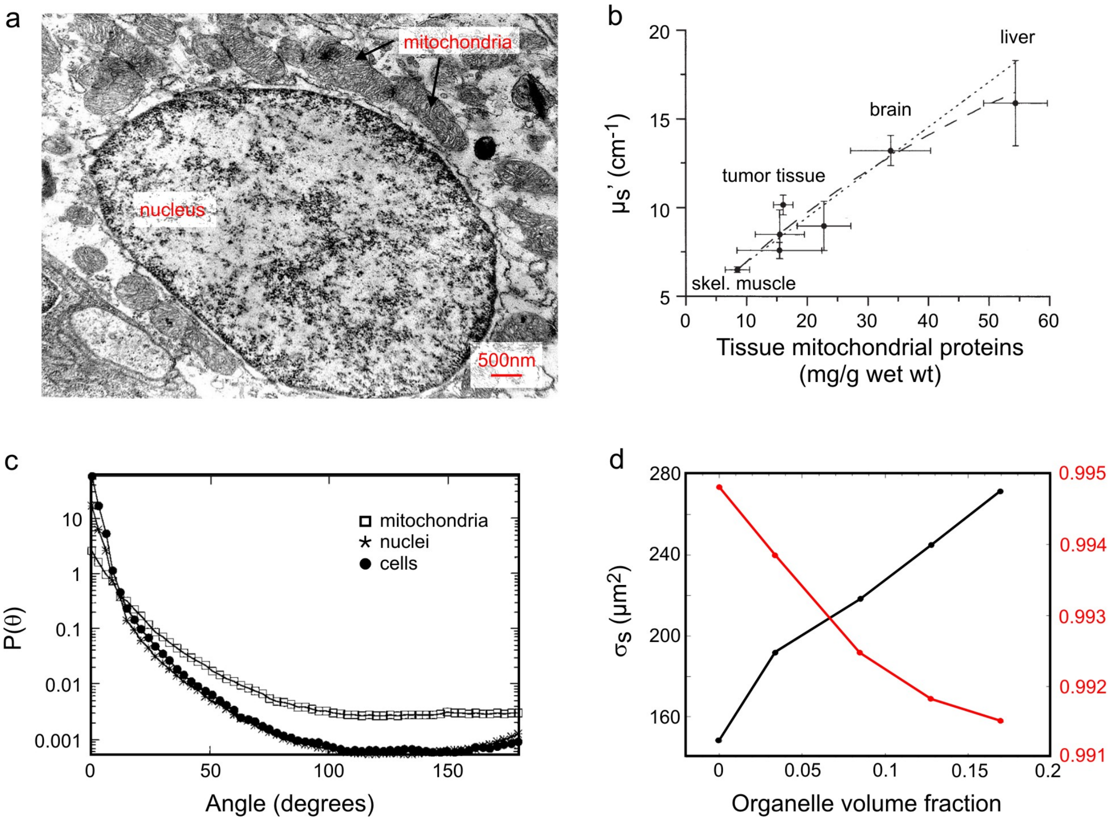

Figure 2.7: The optical properties of biological objects are characterized by intracellular structures. (a) A cell is composed of numerous scattering particles like the nucleus and smaller organelles such as mitochondria. (b) The reduced scattering coefficient μ_s' of various types of tissues depends on the mitochondrial content. (c) Phase function P(θ) measured for cell, nuclei and mitochondria suspensions. (d) FDTD-simulation of the scattering cross section σ_s and the anisotropy factor g as functions of the organelle volume fraction for organelles representing mitochondria. Transmission electron micrograph from T. Voekler, Wikimedia Commons. Diagrams adapted from Beauvoit et al. (1995), Dunn and Richards-Kortum (1996) and Mourant et al. (1998).

morphological changes during the growth phase of the cells were used to demonstrate that scattering at angles larger than 110° correlate with the DNA content of the nucleus. This inhomogeneity of the nucleus became the subject of another study from Mourant et al. (2002b), the effective radii of the nuclear structures were estimated to range from 2 µm to 10 nm and less.

Wilson et al. (2007) took advantage of fluorescent dyes allowing a specific labeling of different cell organelles. In this way, the dyes were used to induce a selective absorption or, in other words, an organelle-specific reduction of light scattering. Changes in the scattering of light between stained and unstained cells were detected for a lysosomal-specific dye whereas no difference was obtained for dyes specific to mitochondria. Later on, they found that lysosomes contribute approximately 14 % to the scattered light which was detected at scattering angles between 0 - 90° (Wilson and Foster, 2007). In contrast to the first publication, these measurements were significantly more sensitive to mitochondria (> 14 %). The latter was supported by another study on apoptotic cells whereas a correlation between changes in light scattering and intracellular areas containing fluorescently labeled mitochondria was observed (Pasternack et al., 2010).

In a more recent publication, images of specifically labeled mitochondria, lysosomes and nuclei inside fibroblasts and epithelial cells were simultaneously acquired with another set of images showing the corresponding sideward scattering of the cell body measured at a scattering angle of 90° (Marina et al., 2012). In both cell types, scattering of light could be assigned to all three organelles thereby considerable light scatter was also collected from non-fluorescent cell compartments. The nucleus was responsible for 30 - 40 % of the light scatter while the contribution of the unstained regions was about 15 - 25 %. Interestingly, the scattering efficiency for lysosomes (20 - 30 %) was higher than for mitochondria (15 - 25 %) which is in contrast to the results from Wilson and Foster (2007) and Pasternack et al. (2010).

In general, cells are phase objects which means if light interacts with cellular inhomogeneities, it experiences a certain phase shift $\Delta\phi$. Such phase shifts can be visualized by a technique called phase contrast microscopy (Zernike, 1955) and are defined by

$$\Delta\phi = \frac{2\pi d \Delta n}{\lambda} \tag{2.26}$$

where d is the sample diameter and Δn the refractive index difference of the sample in relation to its surrounding. Beuthan et al. (1996) observed a visible phase shift only for the nucleus and the cell membrane. Calculations revealed that tissue scattering is caused by the membrane fraction of the cell, i.e. by membrane-containing organelles such as mitochondria and the endoplasmic reticulum (Beuthan et al., 1996). They argued that this is due to the high refractive index difference between the lipids in the membrane bilayers ($n \approx 1.48$) and the aqueous cytoplasm ($n \approx 1.38$). The huge impact of lipids on the scattering coefficient μ_s' was demonstrated by measurements on white adipose tissue in a study from Beauvoit and Chance (1998). Phase contrast microscopy was also used to estimate the size of the scattering particles (Schmitt and Kumar, 1996). The resulting broad distribution of scatterers ranging from 0.2 - 2 µm is comparable to values determined by other methods (compare Mourant et al. (1998) and Nilsson et al. (1998)).

Accompanied by the increasing knowledge from numerous experimental data, many theoretical approaches were established simultaneously to simulate the scattering of light in biological tissues (Schmitt and Kumar, 1998; Wilson and Foster, 2005). The finite-difference time domain (FDTD) technique provides a comprehensive model to predict the cellular scattering in a realistic way as it accounts for structural inhomogeneities of the cells which are the primary source of the scattering (Dunn and Richards-Kortum, 1996; Drezek et al., 1999). Thus, optical parameters can be computed as a function of the organelle formation as shown in Figure 2.7 (d). With increasing amounts of organelles, the scattering cross section σ_s increases while the anisotropy factor g drops down which again indicates that organelles contribute to large angle scattering (compare with Figure 2.7 c).

Angular range	Cellular Structure	References
$\theta \leq 2°$	cell	Mullaney and Dean, 1969; Mourant et al., 1998; Watson et al., 2004; Grosser, 2011
$5° < \theta < 40°$	nucleus	Brunsting and Mullaney, 1974; Beuthan et al., 1996; Dunn and Richards-Kortum, 1996; Mourant et al., 1998
$40° < \theta < 170°$	mitochondria, lysosomes peroxisomes, microtubules	Beauvoit et al., 1995; Dunn and Richards-Kortum, 1996; Mourant et al., 1998; Wilson and Foster, 2007; Marina et al., 2012
$110° < \theta < 180°$	internal structures of organelles	Barer, 1957; Drezek et al., 1999; Mourant et al., 2000; Mourant et al., 2002b; Marina et al., 2012

Table 2.1: Angle-dependent interaction with light.

In conclusion, the interaction of light with biological tissues depends on a variety of different sized particles. Discrepancies regarding the contributions of some cellular structures to the total amount of scattering as for example the contradictory results for lysosomes and mitochondria between Wilson and Foster (2007) and Marina et al. (2012), indicate that this is primarily a result of the different angular ranges from which the scattered light was detected. The strong influence of the particle size on the direction and intensity of the scattered radiation supports this argument (Figure 2.6). Table 2.1 gives an overview of the celluar structures which were identified to influence the light scattering in the corresponding angular ranges.

Over a wide field, the scattering of light is sensitive to cellular organelles which explains why most studies attribute the observed changes to internal structures such as the nucleus, mitochondria, lysosomes and peroxisomes. Experiments that analyzed the scattered light at higher angles obtained a dependency on the intraorganelle architecture while measurements on suspended cells revealed that the cell shape and the refractive index account for scattering in forward direction. The latter is often described as a result of ray optics whereas the cell body is assumed to act as a simple optic lens. This assumption was supported by measurements on single isolated cells which have shown that by orders of magnitude the forward scattering intensity of the cell is higher than the intensity of the sideward scattering (Watson et al., 2004). In fact, Grosser (2011) demonstrated that optically trapped cells are able to focus a gaussian beam. However, the ray optics approach is not generally valid for cells in tissue, as there, the relative refractive index of the cell is reduced due to the surrounding extracellular matrix. Also, the data summarized in Table 2.1 primarily result from measurements on suspensions of isolated cells or cell organelles which are not embedded within their natural environment. To understand how light propagates through a vital biological tissue, the optical interaction between the cellular components has to be considered as a whole.

2.2 The Retina

2.2.1 Morphology of the Inverted Retina

In the vertebrate eye images from the environment are projected through an optical system onto the light-sensitive retina that lines the inner surface of the eyeball (Figure 2.8). It represents the sensory part of the eye very much like the film of a camera. However, if one would build a camera, nobody would design it like the vertebrate retina as the transduction of light into an electro-chemical signal takes places in the photoreceptor cells at the light-averted side of the tissue (Figure 2.9 a). In other words, the light has to pass all cellular structures of the retina before it is captured by the receptor cells.

The photoreceptors are also called first-order neurons because the retina initially gets stimulated if light is absorbed by the visual pigments in the receptor outer segments. In principal, receptor cells are categorized into rod photoreceptors that function at low light levels and cone photoreceptors which are only active under bright light conditions. Depending on the type of the activated photoreceptor cell, the signal is processed by the succeeding secondary and tertiary neurons of the retina (Rodieck, 1973; Masland, 2001). In general, rods and cones synaptically transmit the biochemical message to the bipolar cells that in turn trigger the retinal ganglion cells. Thereby, different types of horizontally oriented amacrine and horizontal cells modify the serial information flow by lateral inhibition processes. Finally, the ganglion cells generate action potentials that run along their axons at the innermost layer of the retina. The optic nerve collects the axons of all ganglions and delivers the information to the visual cortex in the brain (Figure 2.9 a).

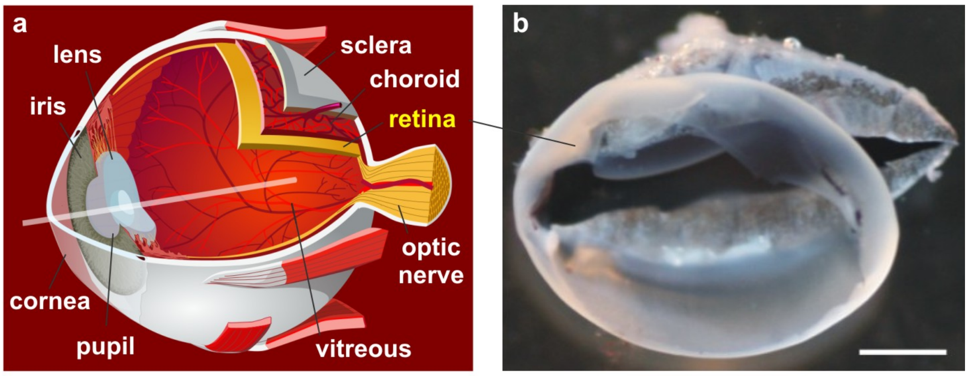

Figure 2.8: The retinal tissue in the eye. (a) The retina is a thin cell layer that converts images of the environment into a visual information which finally can be perceived by the brain. (b) Photograph of a freshly isolated retina in aqueous solution. Images adapted from Ignacio Icke, Wikimedia Commons and from Franze (2007). Scale bar 200 µm.

Under the microscope, the retina shows a distinct stratified structure where the different morphological elements of the retinal cells are well-organized in separate layers (Figure 2.9 a; Rodieck, 1973). The inner and outer segments of the photoreceptor cells form the photoreceptor segment layer (PRS) while their cell bodies are densely packed in the outer nuclear layer (ONL). Cellular processes and synaptic terminals of rod (spherules), cone (pedicles), bipolar and horizontal cells are located in the following outer plexiform layer (OPL). All layers containing substructures of the receptor cells belong to the so-called outer part of the retina which again reflects the positioning away from the incoming light. Similar to the outer part, the inner retina includes an inner nuclear (INL) and an inner plexiform layer (IPL) formed by cellular structures of the downstreamed neurons. The cell bodies of the ganglion cells are located in the ganglion cell layer (GCL) and their axons in the nerve fiber layer (NFL). In addition to the neurons, the retina contains also non-neuronal glial cells, the second cell type of the nervous tissue. The main glial cells of the retina, the Müller cells, span the entire tissue from the inner retinal surface towards the photoreceptor cells (Reichenbach and Bringmann, 2010).

From a physical point of view, the retina is built up of a variety of scattering objects (see section 2.1.4). Regarding Mie theory, the tissue can be roughly approximated to a composition of different sized spherical particles as shown in Figure 2.9 (b). It can be estimated that the Mie parameter Γ for individual spheres varies greatly between the nuclear and the plexiform layers (compare Figures 2.9, c and d). Particularly, strong sideward scattering is expected for the plexiform structures whose sizes are in the order of the visible wavelength (see Figure 2.6 and Table 2.1). Also the larger nuclei are potential scatterers that significantly contribute to the interaction with light (see Figure 2.7 and Table 2.1). The electron micrographs in Figure 2.9 visualize the tiny substructures within the nuclei and the synaptic terminals (Figures 2.9, c and d), their scattering impact was also demonstrated in section 2.1.4.

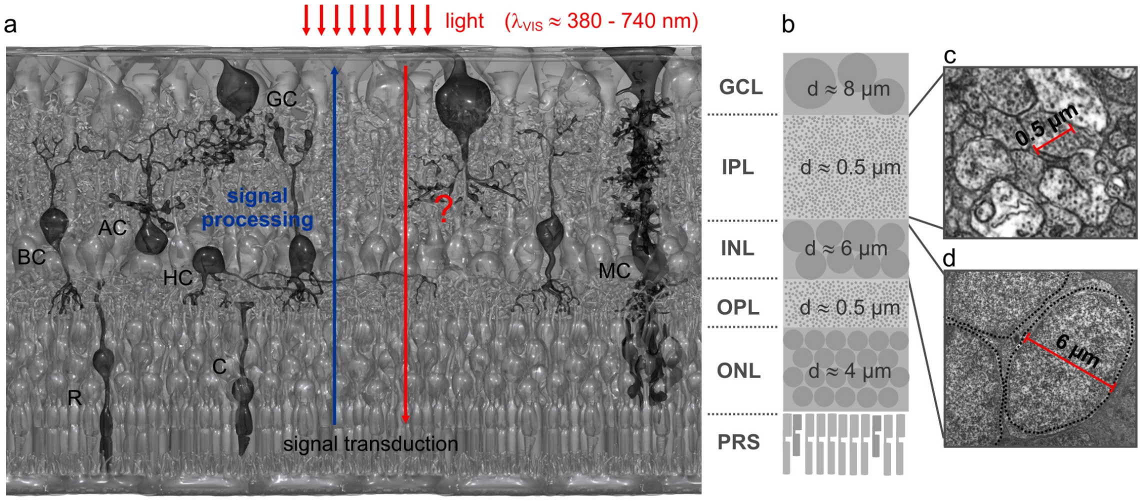

Figure 2.9: The inverted retina of vertebrates. (a) Schematic drawing of the retinal cross section. The signal processing (dark blue) between the neurons is well studied. However, the path of light through the inverted retina towards the photoreceptor cells is unknown (red question mark). Cells: GC, ganglion cell; AC, amacrine cell; BC, bipolar cell; HC, horizontal cell; R, rod photoreceptor cell; C, cone photoreceptor cell. Layers: GCL, ganglion cell layer; IPL, inner plexiform layer; INL, inner nuclear layer; OPL, outer plexiform layer; ONL, outer nuclear layer; PRS, photoreceptor segment layer. Image courtesy of J. Grosche. (b) Size distribution of scatterers for a guinea pig retina. The structures are roughly approximated to spherical particles. (c, d) Transmission electron micrographs of the IPL and INL of a guinea pig retina. Image courtesy of M. Francke.

The retina was often described to be almost totally transparent (Enoch and Glisman, 1966), however, the simple fact that the retina is visible in an aqueous solution (Figure 2.8 b) already indicates a scattering of light due to microscopic phase variations within the tissue (section 2.1.4). Therefore, Goldsmith (1990) was right when he stated that the situation of the inverted retina “is equivalent to placing a thin diffusing screen directly over the film in your camera”.

2.2.2 Vision

In general, the retina mediates two complementary visual systems: the photopic vision based on cone photoreceptor cells and the scotopic vision based on rod photoreceptor cells (Ebrey and Koutalos, 2001).

Both types of receptors are principally built in the same way (Figure 2.10 a; Kennedy and Malicki, 2009). As introduced in the previous section, the outer segments represent the sensory part of the cell as they contain tightly packed membrane discs enriched with light-sensitive photopigments which is rhodopsin for rods and opsins for cones. Morphologically, the receptor cells can be easily identified by the shape of their outer segments. While rod segments are relatively thin and cylindrical, segments of cone cells are rather wide and tapered. The multiple stacks of disc membranes are supported by a longitudinal oriented microtubules scaffold which forms a thin connecting cilium at the base of the outer segment (Eckmiller, 2004). The inner segment of the cell is filled with a myoid matrix containing the prominent golgi apparatus and an oval body, the ellipsoid, that consists of long slender mitochondria and is situated at the junction to the cilium (Kennedy and Malicki, 2009). The soma of the cell includes the bulky nucleus. At the innermost end of the cell the elongated axon forms a synaptic terminal, i.e. a rod spherule or a cone pedicle, that

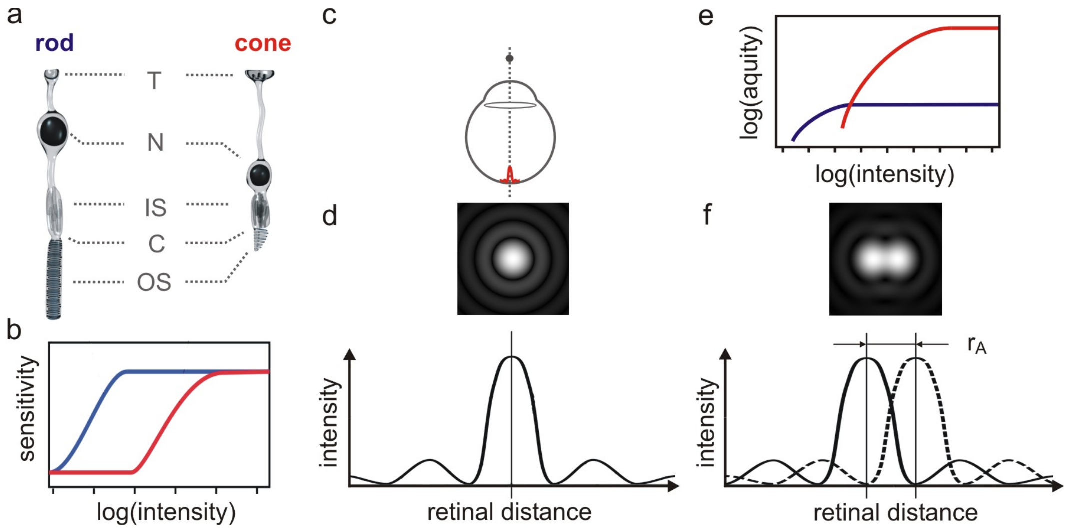

Figure 2.10: Vision of vertebrates is mediated by rods and cones. (a) Morphology of photoreceptor cells. (T, synaptic terminal; N, nucleus; IS, inner segment; C, cilium; OS, outer segment) (b) Sensitivity of rods (blue) and cones (red) as a function of the light intensity. (c, d) The projection of light is limited by diffraction. The resulting Airy pattern (d) is mathematically expressed as a point spread function. (e) The acuity of the rod (blue) and cone (red) system is dependent upon the illumination. (f) The Rayleigh criterion defines the critical distance r_A at which two points are still separately resolved. Images from Wikimedia Commons, J. Grosche and Reichenbach (2008).

enable the cell to communicate with the downstreamed bipolar cells via the release of the neurotransmitter glutamate from numerous synaptic vesicles.

The following processing steps are fundamentally different for the photopic and scotopic pathways (Kandel et al., 1999). While a single ganglion cell receives the information of only a few cone cells, many rods are convergent upon one ganglion cell. The exact ratio depends on the particular retinal area, usually the convergence gradually increases from the center towards the periphery. As an extreme, each cone in the central fovea of primates directly transmits its message to a private ganglion cell (Reichenbach, 1999). However, the convergence varies also among species, e.g., in the retina of nocturnal animals like the cat the signals of up to 1500 rods are summarized (Reichenbach, 1999; Reichenbach, 2008). One can imagine, such a summation results in a high visual sensitivity as a ganglion cell gets excited, even if only a small amount of light reaches the corresponding rod photoreceptor cells. Moreover, a single rod generally responds to lower light levels than a cone cell which further enhances the sensitivity of the scotopic system. Consequently, the threshold of the light sensitivity for rods is about two orders of magnitude lower than for cones (Figure 2.10 b) which is obviously supported by the fact that animals with a nocturnal lifestyle possess a rod-dominated retina.

Besides the highlighted advantages of the scotopic vision, it seems almost pointless to mention that a strong convergence of rod cells is accompanied by a loss of resolution. Finer details of images projected onto the retina cannot be resolved in this way. This is the task of cone photoreceptor cells which are responsible for a high spatial and temporal resolution. As demonstrated in Figure 2.10 (e), the cones mediate high contrast vision at intensities where rods are already saturated (Shlaer, 1937; Rodieck, 1973). The retina usually contains more than one cone type with different spectral sensitivities of their photoopsins, for example, humans have three kinds of cones with absorption peaks of around 420, 530 and 560 nm (Bowmaker and Dartnall, 1980). The output of all cone signals are transmitted to the visual cortex where a subsequent calculation allows the perception of color. In contrast, all rod photoreceptor cells have the same photosensitive pigment, e.g., the human rod absorption peaks at around 500 nm. Thus, scotopic vision just signals the presence of light in the visual field and the brain perceives a black-white image.

To sum up, the rod and cone vision perfectly complement each other by covering a broad range of intensity levels from small amounts of light during night to brightest sunlight at daytime (Pirenne, 1967). However, the visual perception is not only influenced by the scotopic and photopic systems but also by the eye's optical apparatus that defines the quality of the image projected onto the retina (Pask and Barrell, 1980; Westheimer, 2006). In particular, high acuity vision mediated by cone cells requires a sharp input image. For illustration, Figure 2.10 (c) sketches the imaging of a point object within the vertebrate eye. The resulting projection shows no point with sharp edges but rather a blurred image of the point, i.e. a bright central spot (Airy disc) surrounded by less intense rings (Figure 2.10 d). This so-called Airy pattern is caused by diffraction of light as it passes through the spatially limited optic system of the eye (Bergmann and Schaefer, 1998; Hecht, 2002), e.g. the pupil that acts as a circular aperture. Mathematically, the light intensity distributed across the retina can be expressed as a point spread function, shown below in Figure 2.10 (d). This three-dimensional intensity distribution represents the actual visual stimuli arriving at the retina. The diffraction-limited resolution of an optical system is characterized by the distance where two points are still recognized as two separate objects, known as the Abbe resolution limit (Hecht, 2002). Figure 2.10 (f) shows the point spread functions of two adjacent points. The Rayleigh criterion says, objects can be just resolved if the central maximum of the first point spread function coincides with the first minimum of the second one, i.e. if their distance exceeds the width of the point spread function. The critical distance r_{A} between the two maxima is given by

$$r_{\mathrm{A}} = \frac{0.61\lambda}{nsin\alpha} = \frac{0.61\lambda}{NA} \tag{2.27}$$

where λ denotes the wavelength of light, α the half angle of aperture, n the refractive index of the medium and NA the numerical aperture.

2.2.3 Retina Optics

As described in the previous section, vision is based on a sophisticated neuronal meshwork allowing high light sensitivity and/or high spatial and temporal resolution (Pirenne, 1967). The physical light stimulus is converted into an appropriate bioelectric signal that can be processed and perceived by the organism. The precondition for a successful signal transduction is that the incoming signal is not obscured by any other impulse. Therefore, not the amplitude of the signal but rather the ratio between the signal S and the background noise N gives an expression for the quality of the sensory detection. The so-called signal-to-noise ratio SNR provides the condition for a perception (Pettigrew et al., 1986)

$$SNR = \frac{S}{N}. \tag{2.28}$$

With this in mind, it seems controversial why the structure of the retina itself should minimize the yield of data by scattering of light within the retinal tissue. As highlighted in section 2.2.1 the retina is composed of structural inhomogeneities varying in size, shape and organization. This inevitably leads to phase variations, i.e. refractive index mismatches on a microscopic level (see section 2.1.4) which in turn give rise for scattering events. As a result, an immense background noise would reduce the *SNR* and finally would lead to a loss of light and image blurring. The best way to circumvent such a problem impressively shows the fovea of primates, a small pit in the central area of the retina where all tissue layers are laterally displaced and thus allows a direct passage of light towards the photoreceptor segments. However, most vertebrates have no fovea. Maybe there are other optical mechanisms involved. Research into the design of specific retinal cells revealed that certain cells possess optical functions in addition to their common role in the retina. As follows, I will give an overview of the current state of the research in retina optics.

Early studies already demonstrated that scattering of light within the eye, known as entoptic scatter, partially arises from the retinal tissue (Boehm, 1940; Vos and Bouman, 1964). Boehm, 1940 described the retina as 'turbid medium' which is composed of 'light-splintering particles'. Consistent with these results, the transmittance of light in the visible range was measured to be only between 80 - 90 % (Boucher et al., 1986; Hammer et al., 1995). Refractometric measurements on the retinal tissue revealed a mean refractive index of around 1.36 (Valentin, 1879; Nordenson, 1934; Ajo, 1947; Chen, 1993) which lies well in range determined for most biological tissues (section 2.1.4).

Photoreceptor Segments are Wave Guides within the Retinal Tissue

In the mid 20th century, some researchers stated the theory photoreceptor segments may function as dieletric wave guides transporting the light along their tubular length (Di Francia, 1949; O'Brien, 1951). This hypothesis was supported by morphological studies on photoreceptor cells performed by Sidman (1957) and Barer (1957). They used the concentration of cellular solids as a measure of the refractive power and observed a gradual increase of the refractive index from the inner ($n \approx 1.36$) towards the outer segment ($n \approx 1.40$). In historical experiments, Enoch finally found direct evidence for a wave guide behavior as he discovered that light transmission through the vital retina occurs in modal patterns along the outer segments (Figure 2.11; Enoch, 1961; Enoch, 1963). Figure 2.11 (b) shows the most commonly seen patterns, photographed at the terminations of retinal receptors. A change of the wavelength led to a well-defined change of the pattern, i.e. of the V-parameter that characterizes the mode propagation as follows

$$V = \frac{\pi d}{\lambda}\sqrt{n_1^2 - n_2^2} \tag{2.29}$$

where d represents the diameter of the wave guide, λ the wavelength of the light stimuli, and n_1 and n_2 the refractive indices of the wave guide and its surrounding respectively (Snyder and Love, 1983). For $V < 2.4$, the wave guide only supports the fundamental mode and is called a single mode fiber whereas $V \geq 2.4$ indicates the transport of multiple modes. Based upon these findings, many experimental and theoretical approaches arose (Tobey and Enoch, 1973; Tobey et al., 1975; Enoch and Tobey, 1978; Enoch et al., 1981).

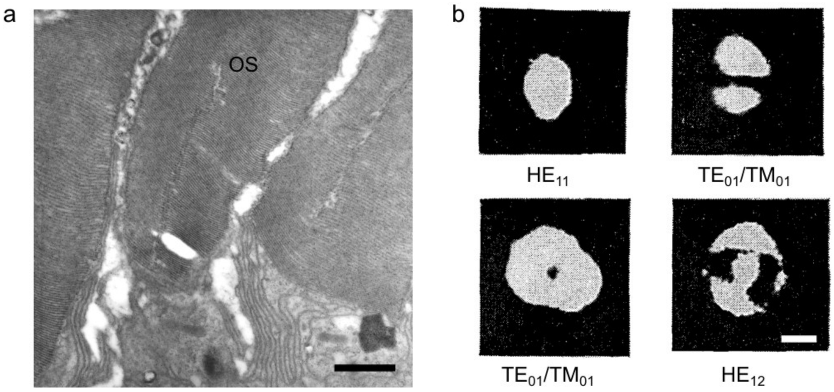

Figure 2.11: Photoreceptor segments are wave guides. (a) Transmission electron micrograph of outer segments of guinea pig photoreceptor cells. The elongated structures are entirely filled with discs of folded membranes. Scale bar 1 µm. Image courtesy of M. Francke. (b) Modal patterns of photoreceptor segments. The most often modes observed from Enoch, 1963 were HE_{11} ($V = 0$), TE_{01} ($V = 2.4$), TM_{01} ($V = 2.4$) and HE_{12} ($V = 3.8$). Scale bar 1 µm. Images adapted from Enoch (1963).

Are Müller cells Wave Guides within the Retinal Tissue?

Photoreceptors are located at the end of the transretinal light path behind the scattering tissue, thus, without upstreamed optical elements the image arriving at the receptors will be distorted. Just one glance at Figure 2.9 (a) reveals that the long Müller glial cells are the only potential candidates for a light transport through the inner part of the retina.

Besides neurons, glial cells represent the second cell type of the nervous tissue whereas their task is mainly the control of the neuronal microenvironment. Müller cells are predestinated for this job as their favorable positioning within the retina allows them to contact every type of neuron. In order to mediate the synaptic signaling between the neurons, Müller cells recycle neurotransmitters as for example the major excitatory transmitter glutamate. They are responsible for the maintenance of the extracellular water and potassium homeostasis, the release of antioxidants under oxidative stress and neurotrophic factors for neuronal development (Newman and Reichenbach, 1996; Reichenbach, 1999; Reichenbach and Bringmann, 2010). Recently, a study from Lu et al. (2006) provided new insights into the mechanical behavior of glial cells. Different than previously assumed, glial cells are softer than their neighboring neurons which protects the neurons in case of mechanical trauma and forms an appropriate substrate for neurite growth.

As described in section 2.1.4, every cell and thus also the Müller cell, consists of numerous inhomogeneities (Figure 2.12). However, some morphological formations within the Müller glial cells are of particular interest for an interaction with light (Reichenbach et al., 2012). For instance, the so-called Müller cell endfeet form a continuous border at the retinal surface, thus, light inevitably enters the tissue through the Müller glia. The following inner process of the cell mainly contains intermediate filaments formed by the protein vimentin while microtubules are the predominant structures within the outer process. It should be noted, both cytoskeletal filaments are aligned along the cell axis within the direction of light. Moreover, organelles with sizes in the order of the visible wavelength are rare. Reichenbach (1989) estimated the organelle-free volume fraction of Müller cells of avascular rabbit retinae to be at around 0.7 - 0.9. This value decreases to 0.24 in the light-averted part of the cell due to the accumulation of mitochondria. In contrast, mitochondria in vascular retinae are evenly distributed throughout the entire cell (Germer et al., 1998). However, the large nucleus is always laterally displaced from the stem process (Figure 2.12). Furthermore, Müller cells tightly ensheat the nuclei of the receptor cells and extend numerous cytoplasmic microvilli in the subretinal space around the rod and cone segments. Consequently, Müller cells form a direct connection between the inner retinal surface and the photoreceptors, the optical elements in the outer retinal part.

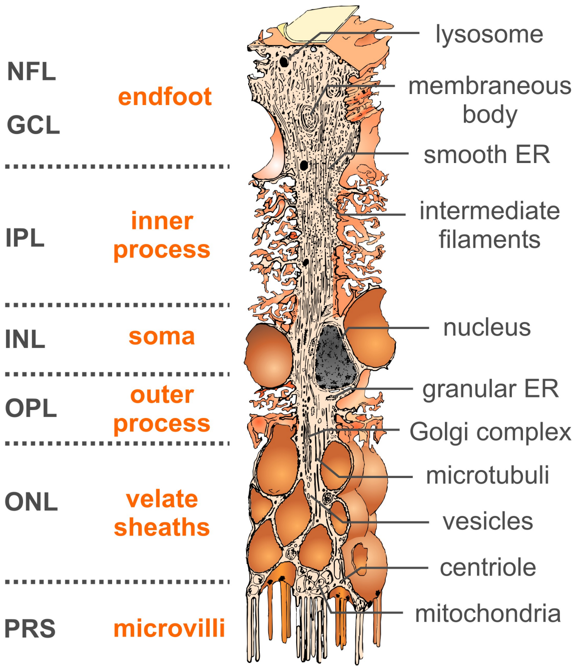

Figure 2.12: Morphology and ultrastructure of a Müller cell. Schematic drawing of an elongated Müller cell and its subcellular components. Note, shape and ultrastructure change for every retinal layer. Image of rabbit Müller cell adapted from Reichenbach (1999).

Driven by the idea of Müller cells being wave guides, my group started to investigate the optical properties of the retina in the late nineties (Reichenbach and Bringmann, 2010; Reichenbach et al., 2012). Quantitative phase microscopy on enzymatically dissociated retinal neurons revealed a refractive index of 1.35 - 1.36 which is very close to earlier estimates for the retinal tissue ($n \approx 1.36$) (Figure 2.13; Nordenson, 1934; Chen, 1993; Franze et al., 2007). It should be noted that these values were measured on the somata of the neurons, i.e. the subcellular part with the most dense architecture. Surprisingly, the refractive index of both Müller cell processes was shown to be significantly higher (1.376 - 1.380) and corresponds very well to that of light guiding photoreceptor outer segments ($n \approx 1.40$; Sidman, 1957). In addition, an observed decrease of the index of refraction towards the endfoot region ($n \approx 1.359$) was believed to reduce the reflection at the border to the low refractive vitreous ($n \approx 1.335$). As described by equation 2.29, guidance of light is not only dependent on the refractive index difference between the structure and its surrounding but also on the object's diameter and the wavelength. Figure 2.13 summarizes the results calculated by Franze et al. (2007). Despite the complex morphology of Müller cells, the V-parameter, i.e. the light guiding capability, remains nearly constant along the entire length of the cell body.

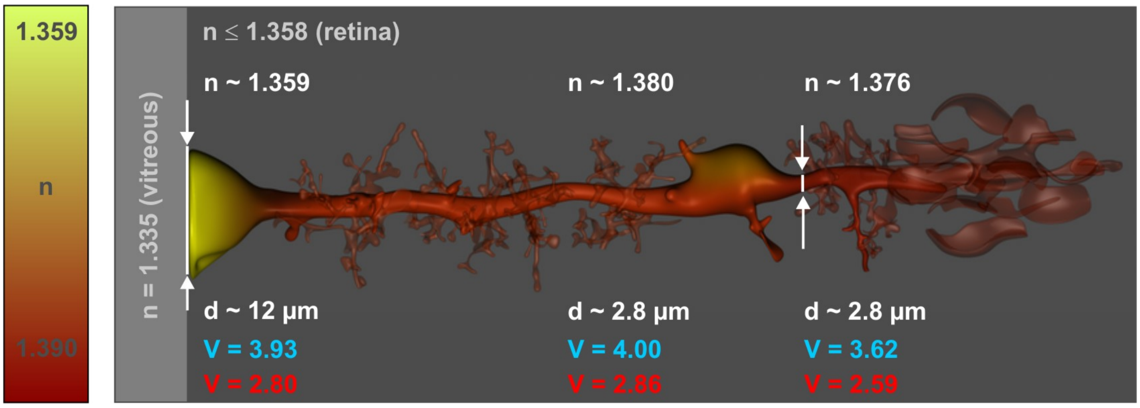

Figure 2.13: Müller cells are potential wave guides within the retina. Schematic drawing of a Müller cell, the darker the color the higher the refractive index. Despite refractive index variations and changing diameters, the V-parameter for 500 nm (blue) and 700 nm (red) stay nearly constant along the cell. All values are specific for guinea pig retinae. Image courtesy of J. Grosche, adapted from Franze et al. (2007).

To find direct evidence for the wave guide nature of Müller cells, Franze et al. (2007) developed a setup based on a dual-beam laser trap (Guck et al., 2001). In this setup, two counterpropagating infrared laser beams were used to align individual suspended Müller cells between the tips of two opposing glass fibers. The refractive index of the solution was adjusted to the well-known mean value of the retina ($n \approx 1.36$). Additionally, visible laser light was coupled into one of the two fibers and the light coupled back into the opposite fiber core was detected by a powermeter (Figure 2.14 a). In contrast to a situation without a cell in the trap where only a small fraction of the divergent light beam reached the core of the output fiber, the intensity transmitted through a Müller cell was comparable with a control experiment where both fibers were in contact with each other (Figure 2.14, b and c). The relative light guiding efficiency η_r, i.e. the ratio between the intensity with and without a Müller cell, was typically around 1.9 (Franze, 2007). In other words, the experiments successfully demonstrated that isolated Müller cells act as wave guides, even if they consist of numerous inhomogeneities.

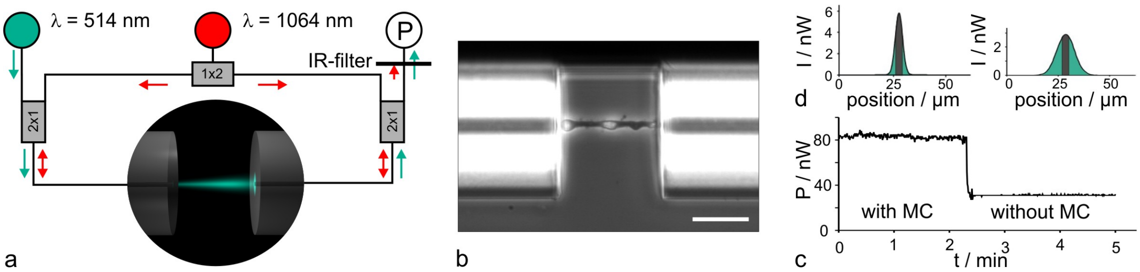

Figure 2.14: Isolated Müller cells act as wave guides. (a) Modified optical trap to measure the light transmission through single enzymatically dissociated Müller cells. (P, power meter; IR-filter, infrared filter) (b) Müller cell aligned by optical forces induced by the two counter-propagating infrared laser beams ($\lambda = 1064$ nm). Scale bar 50 µm. (c) Power of visible light ($\lambda = 514$ nm) measured during an experiment. (d) Intensity distribution at the receiving fiber tip with a cell in the trap (left) and after its removal (right). (grey: light coupled into the core of the output fiber, green: fraction of light lost for detection) Images adapted from Franze (2007) and Franze et al. (2007).

However, such an experimental design raises fundamental questions. As described in section 2.1.4, isolated cells preferentially scatter in forward direction regardless of their ultrastructure and morphology (Watson et al., 2004). In line with this, Grosser (2011) has shown that roundish cells within a dual-beam laser trap focus an incoming gaussian beam onto the core of the opposite fiber whereas the coupling efficiency increases with an increasing refractive index gradient between the cell and its surrounding. Furthermore, the smaller the cell and the more elliptical its shape, the higher was the amount of light arriving at the output core. In principle, this confirms predictions from Mie theory that single spheres whose sizes are much larger than the wavelength of light are subjected to the ray optics regime (see section 2.1.3). Consequently, the trapping of any arbitrary cell is accompanied by an increase of the light intensity at the output fiber which in turn implies that the specific experimental procedure is not well suited to demonstrate a particular optical function of Müller cells.

Another critical point is that a light guiding fiber usually consists of two concentric layers where the core in the center is enclosed by a low refractive cladding. Based on this configuration, the incoming light propagates through the internal core according to equation 2.29 (Snyder and Love, 1983; Bass, 1995). As one can imagine, the refractive index throughout the retina follows the non-uniform distribution of the retinal structures (see section 2.2.1), but this is simply unknown since refractive index measurements on isolated cells do not reliably reflect the real conditions inside the tissue. Thus, experiments on isolated cells, surrounded by homogeneous fluids, definetely do not mimic the complex optical landscape a Müller cell, i.e. the light transporting core, experiences when embedded in the retinal tissue.

In conclusion, it is the main task of the present work to show that Müller cells within the vital retina indeed function as wave guides.

3 Material and Methods

In this chapter the methods applied to study the optical properties of the vital retinal tissue will be presented. At first, the preparation of the fragile biological sample is introduced wherein the visualization of the optically relevant Müller and photoreceptor cells is described for retinal slice preparations and wholemounts. Special attention is paid to maintain the full functionality of the cells inside the tissue. Then, two techniques will be presented that combine the high resolution imaging of the retina and the local light stimulation of the sample to provide detailed information about the cellular structure and the corresponding behavior of light. Both illumination methods will be compared and discussed regarding their biological application.

3.1 Tissue and Cell Preparation

3.1.1 Animals Used - Guinea Pig Retina as Model System

For all experiments, retinae were obtained from guinea pigs. In contrast to other rodents routinely used in laboratories (e.g. rat or mouse), the guinea pig retina is avascular and thus relatively thin (Buttery et al., 1991; Dreher et al., 1992). Consequently, the Müller cells, which span the retinal thickness from the vitreous to the choroidal surface, are comparatively short. This facilitates an investigation of the intraretinal light path by reducing the probability of preparation artefacts (section 3.1.5). Another advantage for light guidance studies, that comes along with an avascularisation, is a large Müller cell diameter (Germer et al., 1998). Both processes, within the inner and outer part of the retina, have diameters of around 2 - 3 µm that ensure the coupling of light into the glial cell (section 3.2.1).

The retina of the guinea pig is sensitive to light in the visible range from 350 - 600 nm, based on the absorption spectrum of the visual pigments in the photoreceptor cells (Figure 3.1). Guinea pigs have rod receptor cells and two types of cone photoreceptors, the S- and M-cones. The rarely occurring S-cones respond to short wavelengths whereas the dominant M-cones are most sensitive to light at 530 nm which is close to the absorption peak of the rod cells at 500 nm (Parry and Bowmaker, 2002). Accordingly, optical elements in the retina have to be well suited for wavelengths in the range of 500 - 550 nm.

Adult guinea pigs were reared with free access to water and food in a species-appropriate environment under 12-hour light and 12-hour dark cycles. All experiments were performed in accordance to the ARVO Statement for the Use of Animals in Ophthalmic and Vision Research and to the German law on the protection of animals.

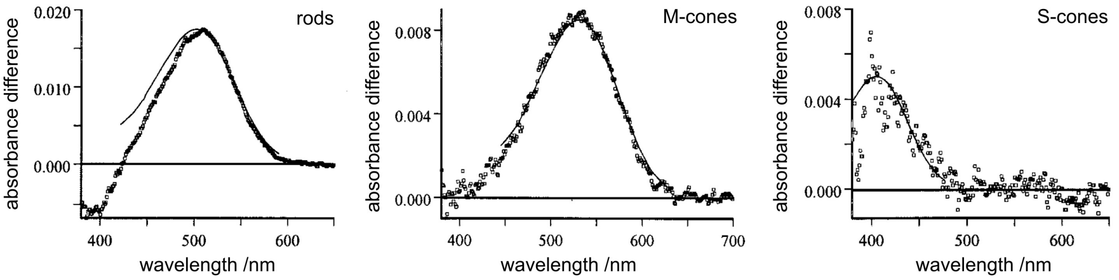

Figure 3.1: Absorbance spectra of photoreceptor cells in the guinea pig retina. Visual pigments of guinea pig photoreceptor cells absorb light in the range from 350 - 600 nm. The S-cones are sensitive to short wavelengths with an absorption peak at 400 nm, the rods and M-cones respond to medium wavelengths of around 500 nm. Shown are the mean difference spectra between the absorbance before and after a complete bleaching of the receptor cells. The data (open squares) are overlayed with best-fitted rhodopsin templates after Bowmaker et al. (1991). Diagrams taken from Parry and Bowmaker (2002).

3.1.2 Retina Preparation

Before the preparation procedure started, the animal was kept under dim light conditions for about 1 h. Light stimulates the sensitive photoreceptor cells which in turn trigger the activity of all other neurons in the vertebrate retina (Kandel et al., 1999). Also Müller cells as central components of the light-sensitive tissue are influenced in their function (Newman, 2005; Rillich et al., 2009; Wang et al., 2011). The ability of the photorecep-

substance	concentration [mMol/l]
NaCl	136
KCl	3
$CaCl_2$	2
HEPES	10
$MgCl_2$	1
D-Glucose	11

Table 3.1: Composition of extracellular solution. All substances are dissolved in bi-distilled water and the pH is adjusted to the physiological value 7.4 by using 1 M TRIS-Puffer (pH = 10.4).

tors to respond to changing light stimuli depends on an interplay between a bleaching of the visual pigments and a following regeneration process which ensures that a sufficient quantity of unbleached pigment is present for the next excitation (Cote et al., 1994). An exposure to high light levels over a long period leads to an increased bleaching and thus to a complete lack of light-sensitive chromophores which makes the retina blind for new light stimulations. Thus, while exposing the tissue to intermediate light levels for a period of about 1 h, the cones and the slower rods (Hestrin and Korenbrot, 1990; Miller and Korenbrot, 1994) have time to adapt to the light conditions, known as mesopic vision which is mediated by both receptor types. To guarantee full functional capability of the retina, all following preparation procedures were carried out under the same dim illumination. The animals were killed with carbon dioxide and their eyes had been removed. The enucleated eyes were immediately transferred into an extracellular solution consisting of sodium chloride (NaCl), potassium chloride (KCl), calcium chloride ($CaCl_2$), magnesium chloride $MgCl_2$, HEPES, and D-glucose (pH 7.4) (Table 3.1). All further preparation steps were performed in this solution to imitate the physiological environment and thus to slow down the cellular degeneration.

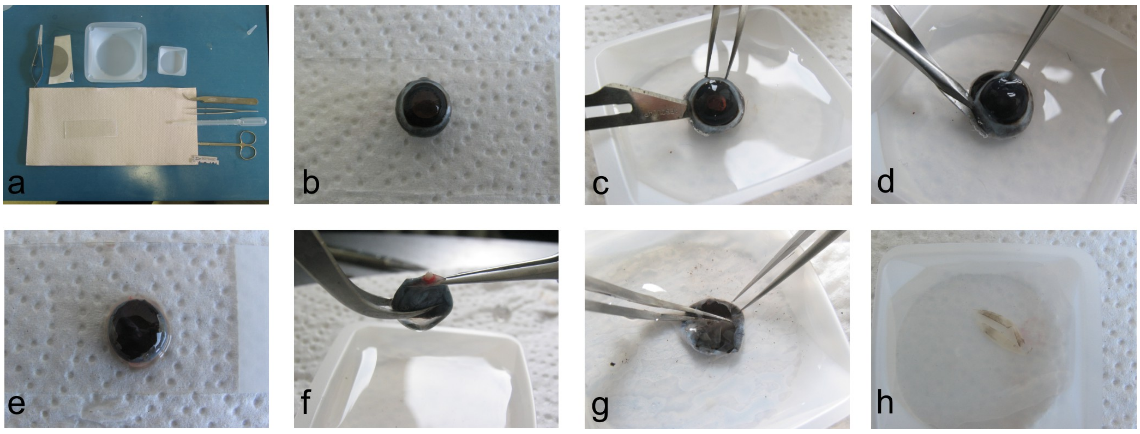

Figure 3.2: Preparation of the guinea pig retina. (a, b) The freshly dissected eye is immediately incubated into extracellular solution. (c-e) The eye is opened by a slight cut and the anterior part of the eye is removed. (f) The drop-like glass body is carefully detached from the eyecup. (g, h) The retina is gently separated from the pigment epithelium.

After removing some of the connective tissue (Figure 3.2, a and b), the eye ball was opened by a cut behind the ora serrata (Figure 3.2 c). The cornea, the iris and the lens were gently separated from the posterior part of the eye (Figure 3.2, d and e) to remove the vitreous body (Figure 3.2 f). Finally, the retina was carefully detached from the pigment epithelium (Figure 3.2 g), in particular, for light transmission experiments a complete detachment was required. This was facilitated by the existing low light condition. During dark adaptation the adherence of the retinal pigment epithelium to the photoreceptor layer is reduced in comparison to bright light where the pigment cells tightly envelope the photoreceptor outer segments to undergo a variety of physiological interactions that enforce the adhesion between both cell types (Owczarek et al., 1975; Faude et al., 2001). After dissection, further preparation procedures of the isolated retina were carried out immediately.

3.1.3 Vital Preparation of Retinal Wholemounts

Especially for light guidance experiments, it was essential to ensure the activity and function of all retinal cells during the experiment since optical properties as the refractive index are strongly correlated with the retinal function (Barer, 1957; Bolin et al., 1989; Tearney et al., 1995; Beuthan et al., 1996; Knüttel et al., 2004; Dirckx et al., 2005; Ullmann et al., 2012). Besides dim light conditions and fast retinal dissection, an immediate experimental execution was important. To slow down the retinal activity during incubation times as for example during staining procedures and washing steps, all these procedures were carried out on ice. In addition, due to the natural curvature of the eyeball, the retina

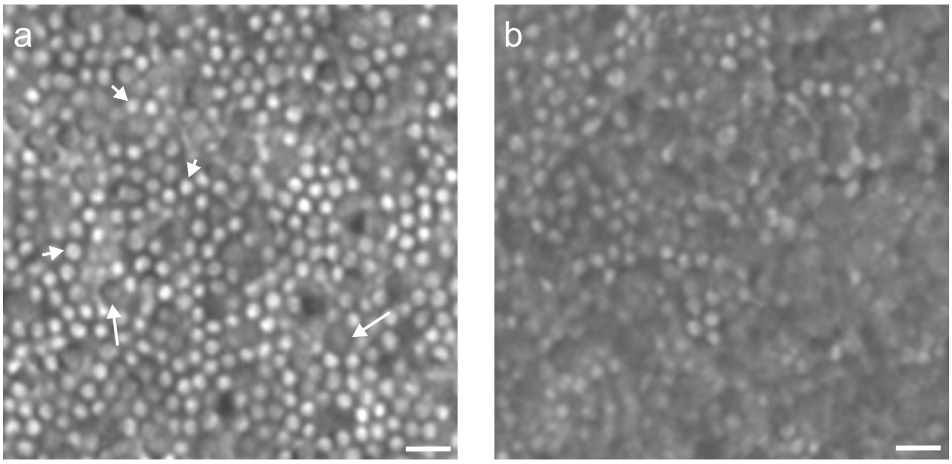

Figure 3.3: Light transmission through the retinal tissue. (a) The inner retinal surface is illuminated in brightfield to detect the transmitted light at the backside of the retina, the photoreceptor layer. The transmission image clearly shows the photoreceptor segments and even allows to assign these segments to one of the two different receptor types. The numerous rod segments (small arrows) with a diameter of about 1 - 2 µm form a homogeneous pattern, interspersed by less numerous cone segments (large arrows). In comparison to the rod cells the cones are larger in diameter (2 - 3 µm) but their segments are shorter. By positioning the focal spot of the objective (63x, *NA* 0.95W) onto the tips of the rod segments, these structures are the brightest. (b) The transmission image is well suited to indicate photoreceptor artefacts. Damaged or detached photoreceptor segments cause non-uniform light patterns. Scale bars 5 µm.

tends to form a roll which suppresses a homogeneous access of nutritions or fluorescent dyes to all parts of the sensitive tissue. This behavior was avoided by some cuts from the periphery towards the retinal center. Moreover, every step was done slowly to prevent any mechanical stress or artefacts inside the tissue. In particular, mainly the photoreceptor cells are very sensitive to mechanical stress, since only a thin fragile cilium connects the outer segment to the rest of the cell. Thus, photoreceptor segments can be damaged or even detached which disables the retina for light guidance experiments (Figure 3.3).

3.1.4 Staining of Vital Cells in the Retinal Tissue

To study the Müller cell-dependent propagation of light inside the living retinal tissue, the cells have to be visualized. The funnel-shaped endfeet of all Müller cells in the retina form a confluent layer towards the vitreous body, the so-called inner limiting membrane, which directly contacts the surrounding medium after retinal preparation. Thus, a fast access of chemical reagents into the Müller cells is already given by its morphology. A specific

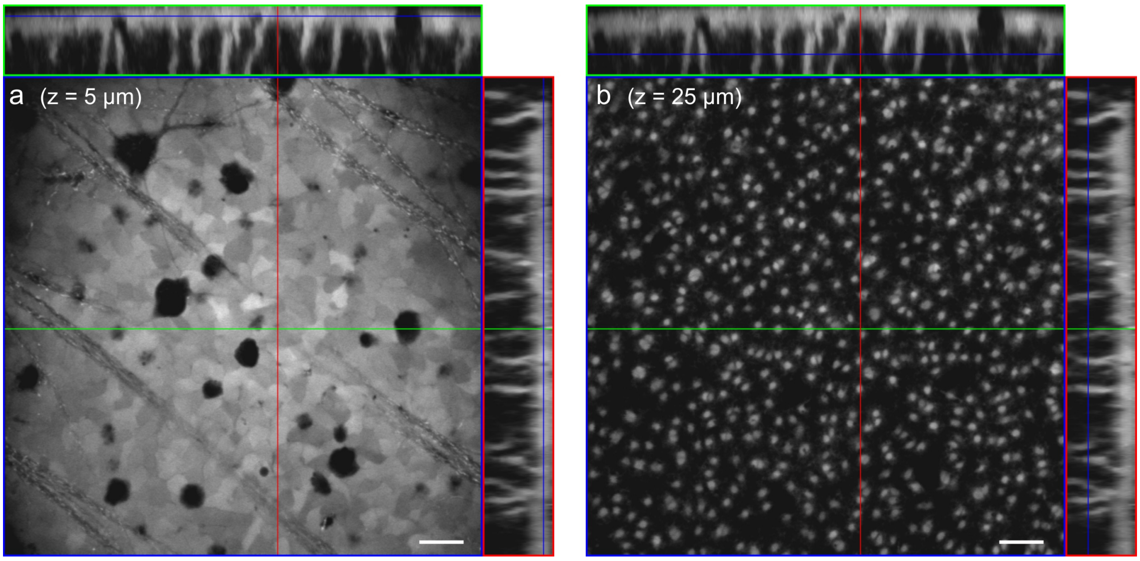

Figure 3.4: Dye-filled Müller cells in the living retina. After exposing the isolated retinal tissue into a physiological solution, containing the dissolved dye Mitotracker orange, the vital dye was accumulated into Müller cells. A confocal z-stack of the dye-loaded retina ($z = 2$ µm) was taken with a 40x water immersion objective. (a) Close to the retinal surface ($z = 5$ µm) the Müller cell endfeet are densely packed and form a homogeneous cover only interrupted by black circular holes indicating the neuronal bodies of ganglion cells. Orthogonal views (images surrounded by red and green boxes) of Müller cells oriented along the red (respectively the green) line, drawn in the confocal image, demonstrate a funneling of Müller cell endfeet into thinner processes. (b) The intensively stained stem processes are uniformly distributed in the inner plexiform layer ($z = 25\ \mu m$), thus, single Müller cells can be well recognized. Scale bars 20 µm.

identification of living Müller cells with a confocal microscope can be achieved by adding suitable fluorescent dyes to the surrounding solution (Uckermann et al., 2004b). In the experiments presented in this work, the thiol-reactive Mitotracker dyes, namely Mitotracker green, Mitotracker orange or Mitotracker deepred (M7514, M7510, M22426, Molecular Probes, Eugene, OR, USA) were chosen to stain Müller cells (Figure 3.4). The lyophilized dye was dissolved in 50 µl anhydrous dimethylsulphoxide (DMSO, D2650, Sigma-Aldrich, Taufkirchen, Germany) to produce a stock solution with a concentration of 1 mM. This solution was diluted in an extracellular solution to reach a final concentration of 2 µM. Subsequently, the freshly dissected retina was incubated for 10 - 15 min into an extracellular solution containing one of the fluorescent Mitotracker dyes. For light guidance experiments, I used retinal pieces from peripheral regions of the tissue since the cell densities slightly vary throughout the different retinal areas (Reichenbach and Robinson, 1995).

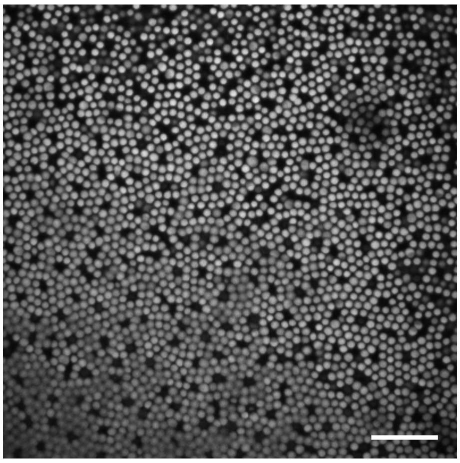

Figure 3.5: Vital staining of the photoreceptor cells. To image outer segments of photoreceptor cells by confocal microscopy, the fluorescently labeled segments (Mitotracker orange) have to face the objective. Scale bar 20 µm.

In addition to the predominantly stained Müller cells, also the photoreceptors, especially their inner and outer segments were fluorescently labeled by the staining procedure. The retina of the guinea pig is approximately 130 µm thick which is relatively thin but not thin enough for confocal detection of the outer segments at the opposing surface. For an imaging of these segments, the tissue has to be turned with the photoreceptor cells pointing towards the objective (Figure 3.5). This implies, that based on the different spatial localization of Müller cells and photoreceptor segments (see Figure 2.9 a), both cell types cannot be recorded simultaneously with a common confocal microscope.

3.1.5 Retinal Slice Preparation

To visualize the path of light along all retinal layers from the retinal surface towards the photoreceptor cells, the retina has to be sliced (Li et al., 2001; Newman, 2001). The retina is a thin fragile tissue, thus, for slicing it has to be fixed on a supporting material. Therefore, the Müller cell-stained retina was gently spread onto a nitrocellulose membrane (ME 25, Whatman, Kent, UK) with the photoreceptor cells attached to the material. A custom-built machine was used to cut the tissue-membrane assembly into thin slices ($b = 1$ mm). To obtain the retinal cross section, the retina slices were mechanically fixed in a sample chamber filled with extracellular solution. Images of the tissue, taken with a 63x water-immersion objective (Achroplan, Zeiss, Jena, Germany) of a confocal microscope (LSM 510 Meta, Zeiss, Jena, Germany), clearly identified Müller cells and photoreceptor segments (Figure 3.6). All structures seen in Figure 3.6 are located in the same focal plane of the objective. They are not a projection composed of several images taken in different depth of the sample, as it is common in confocal microscopic pictures. In Müller cell-dependent

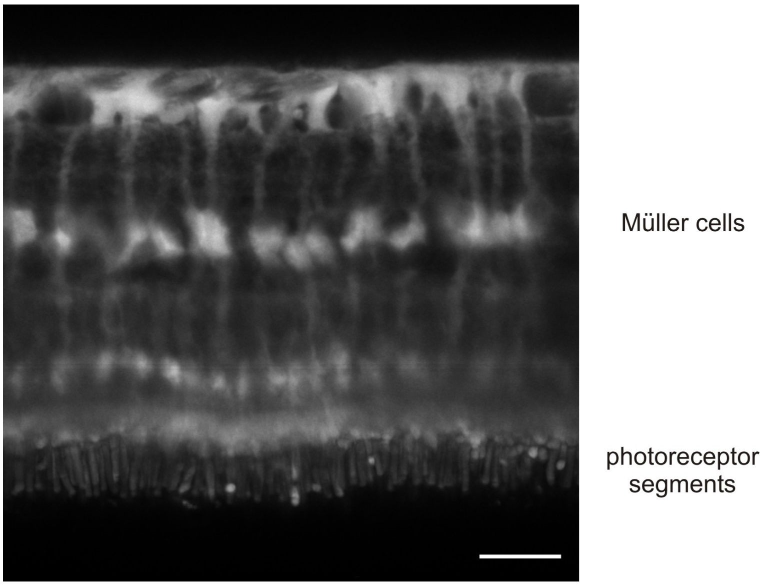

Figure 3.6: Slice preparation of the vital retina. The retina is attached to a stripe of nitrocellulose membrane (not shown) to allow the detection of the retinal cross section. The tissue was previously loaded with the dye Mitotracker deepred. A single confocal image is shown at a defined depth from a z-stack, recorded by a laser scanning microscope. All cell components along the retinal light path are in the same focal plane of the objective (63x, *NA* 0.95W), an important precondition for light propagation experiments. Not only the thick cell compartments (endfeet, nuclei), but also the thin inner and outer processes of Müller cells are visible. The photoreceptor segments, seen in the image, are morphologically located in the same retinal light path as the observed Müller cells. Scale bar 20 µm.

light guidance experiments on retinal slices (Setup shown in Figure 3.8; Agte et al., 2011), all structures have to be in the same focal plane which is located approximately 5 - 10 µm below the cutting edge (section 3.2.1).

3.1.6 Visualization of Müller Cells and Cone Photoreceptor Cells

Besides Müller glia cells, also neuronal photoreceptor cells within the retina possess optical properties (see section 2.2.3). To investigate potential coupling between the optics of both cell types, morphological studies regarding the cellular distribution and orientation had to be performed. In particular, rough quantitative estimates of cone photoreceptors and Müller cells suggested a direct correlation between them and their optical function. In the following sections, I will describe two different techniques to simultaneously visualize Müller cells and cones within the retinal tissue.

Immuno- and Lectin-Histochemistry

Pieces of freshly dissected guinea pig retina were immediately transferred into a PBS-filled petri dish (0.1 M, pH 7.4) containing 4 % paraformaldehyd. For tissue fixation, the petri dish was placed at 4 °C for approximately 1 h. After several washing steps in PBS in order to completely remove the fixative solution, the retina was incubated in a blocking buffer with normal donkey serum at room temperature for about 1 h. Subsequently, this solution was replaced by a PBS solution with primary antibodies and incubated overnight at 4 °C. The primary antibody anti-Vimentin (1:200, clone V9, Sigma Aldrich, Germany) is directed to the intermediate filaments in Müller cells (Reichenbach and Robinson, 1995; Shaw and Weber, 1984), while the biotin-conjugated lectin peanut agglutinin (1:250, PNA, FITC-coupled, Sigma Aldrich, Germany) specifically binds to cone photoreceptor cells (Krishnamoorthy et al., 2008). A complex washing procedure (again with PBS) lasting at least 4 h followed this incubation, before the tissue was embedded in a solution containing secondary antibodies (anti-mouse or anti-rabbit labeled with Cy3, Jackson immunoresearch, West Grove, USA) and streptavidin (Streptavidin labeled with Cy2, Sigma Aldrich, Germany) and placed at 4 °C overnight. After washing, for approximately 3 h, to finally remove all remaining substances the tissue was ready for investigation.

Loading the Retina with FM1-43

Fresh guinea pig eyes were opened and the anterior part was separated. Immediately after removal of the vitreous body, the eye cup was embedded in oxygenated Ames medium (pH 7.4, Sigma-Aldrich, Taufkirchen, Germany) containing the lipophilic styryl dye FM1-43 (30 µm, Molecular Probes, Eugene, USA) which unspecifically labeled the plasma membrane of the retinal cells. During an incubation period of about 45 min, the sample was kept in darkness to activate the photoreceptor cells, i.e. to induce exo- and endocytotic processes at the synaptic terminals. Consequently, the dye-loaded membrane of the photoreceptor synapse was endocytosed and fluorescent vesicles filled the synaptic endings of the receptor cells until an exposure to light again suppressed the synaptic activity (Rea et al., 2004; Choi et al., 2005a). The tissue was washed for 1 min with Advasep-7 (1 mM, Sigma-Aldrich, Taufkirchen, Germany), a cyclodextrin with a high affinity to FM1-43 that binds fluorescent molecules from the unspecific labeled membranes accordingly (Figure 3.7).

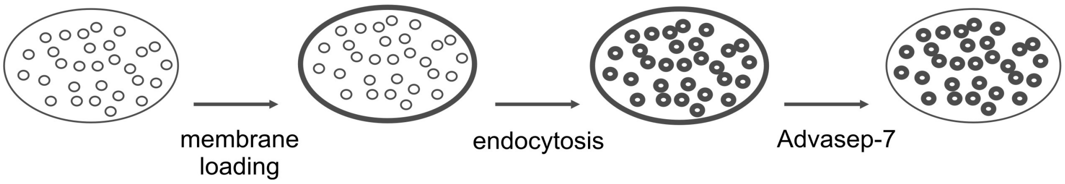

Figure 3.7: Loading the retina with FM1-43. The dye FM1-43 labels the surface membranes within the retinal tissue, including the plasma membrane of the photoreceptor synapses. In darkness endo- and exocytosis start and fluorescent synaptic vesicles are formed. Advasep-7 removes the surface labeling to selectivly stain the synaptic terminals. Image adapted from Choi et al. (2005b).

For long incubation times, the vesicle-filled synaptic terminals were the only remaining labeled structures within the tissue, in particular, the huge cone photoreceptors were visible. However, for my experiments the concentration and duration of Advasep-7 incubation was chosen to still achieve strong fluorescence in the inner plexiform layer, in which the non-labeled Müller cells appeared as dark cylindrical tubes. Also other components of the cone photoreceptors such as the inner and outer segments remained fluorescently stained. After the staining procedure was completed, the retina was gently dissected from the eye cup. Subsequently, two-photon microscopy ($\lambda = 860$ nm, Coherent, Dieburg, Germany) was used to record the fluorescence of the tissue, i.e. to simultaneously visualize the Müller cell processes within the inner plexiform layer and the cone segments.

3.2 Optical Imaging

3.2.1 Optical Fiber Setup

The light propagation through the retinal tissue was studied by using a combination of fiber optics and confocal microscopy (Figure 3.8; Agte et al., 2011). To allocate changes of light to specific cellular structures, a simultaneous detection of the incoming, the propagating and the transmitted light was necessary.

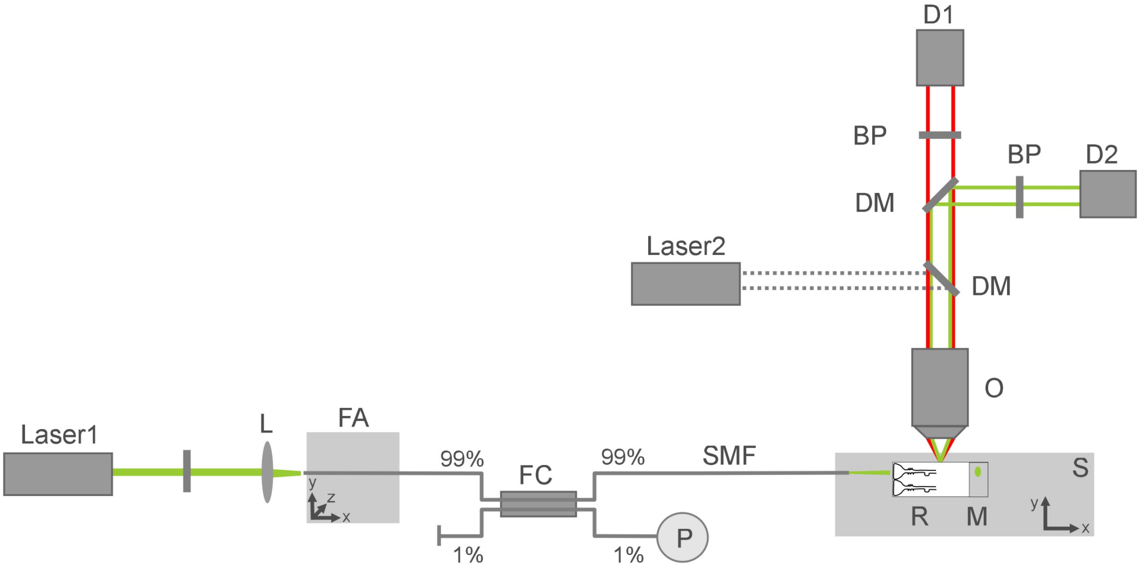

Figure 3.8: Optical Fiber Setup to visualize the beam path through the retinal cross section. The fluorescent sample, a retinal slice (R) attached to a nitrocellulose membrane (M) stained with Mitotracker orange, is placed onto the stage (S) of an upright laser scanning microscope (LSM 510). Fluorescent light (red) induced by confocal excitation (Laser2, 543 nm) is collected by a water immersion objective (O, 63x, *NA* 0.95W) to pass a dichroic mirror (DM) and a bandpass filter (BP) before it is recorded by detector D1 of a first confocal channel. Light from a laser diode (Laser1, 532 nm, green) is sent through an aspheric lens (L) to focus the light onto the tip of a single mode fiber (SMF). Efficient coupling of light into the glass fiber is achieved by a fiber launcher (FA) allowing precise mechanical adjustments of the glass fiber in xyz-direction. A fiber coupler (FC) is used to control the power of light (P, power meter) coupled into the single mode fiber. One leg of the coupler is again connected to the single mode fiber whose core is placed in the focal plane of the objective, in front of the vitread surface to illuminate single Müller cell endfeet. The scattering of the laser light inside the sample (green) is detected by a second channel of the confocal imaging unit (DM, dichroic mirrors; BP, bandpass filter; D2, detector). The micropositioning stage moves the sample perpendicular to the light propagation.

The light source used in the experiments was a laser diode (LAS-GTEC, Laser 2000, Wessling, Germany) operating at 532 nm with a maximum output power of 20 mW. Broadband mirrors (BB1-E02, Thorlabs, Newton, NJ, USA) were used to control the alignment of light, before it was focused by an aspheric lens (C110TME-A, Thorlabs, Newton, NJ, USA) which was mounted in front of a fiber holder on top of a fiber launch system (MBT610/M, Thorlabs, Newton, NJ, USA). The xyz-drive of the fiber launcher precisely positioned the focal spot onto the tip of a single mode fiber, optimized for wavelengths between 450 - 600 nm (460HP, Thorlabs, Newton, NJ, USA). In this way, the light was efficiently coupled into the glass fiber. Then, the fiber was spliced to the input of a fiber coupler (FC632-99B, Single Mode Standard Coupler, Thorlabs, Newton, NJ, USA). To monitor the laser intensity, the first output was attached to a power meter (OP-2VIS, FieldMate, Coherent, Santa Clara, CA, USA) while the second output was again spliced to a single mode fiber and was used as light source for the experiment. The ends of the fiber were cut by a fiber cleaver (XL410, Precision Fiber Cleaver, Thorlabs, Newton, NJ, USA). Neutral density filters in the beam path were used to adjust the light intensity

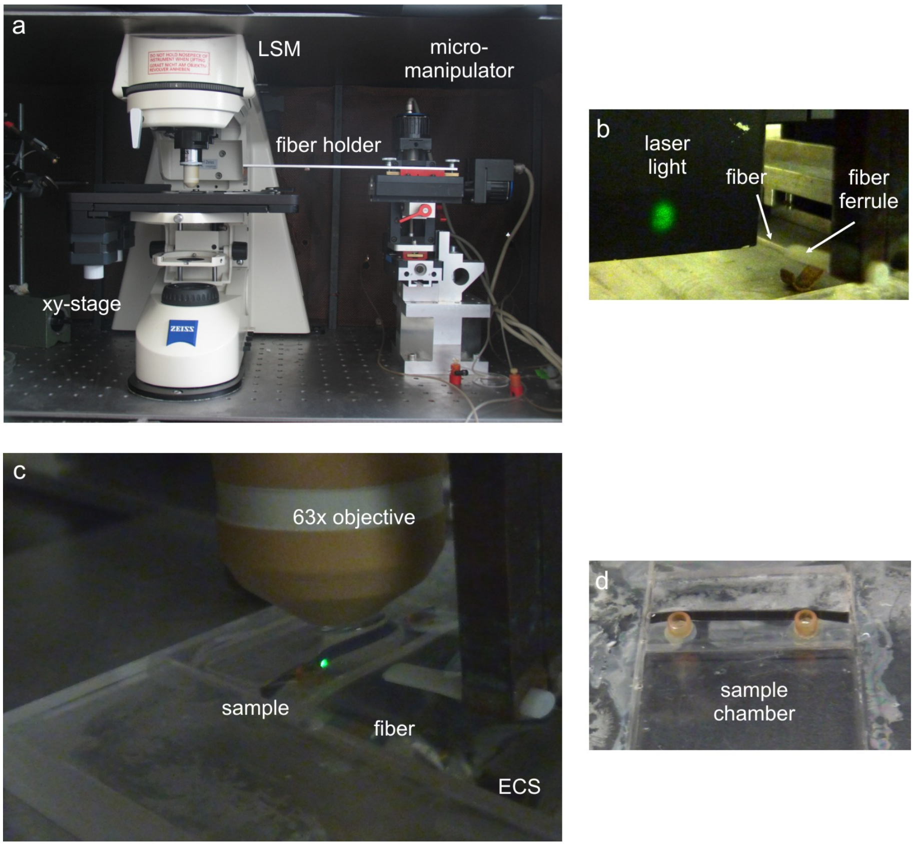

Figure 3.9: Positioning of the fiber. (a) The micromanipulator places the fiber under the objective. A motorized stage controls the xy-movement of the sample. (b) For stable adjustments the glass fiber is inserted into a ceramic ferrule. To demonstrate the beam divergence, the green laser light is projected to a screen in some distance to the fiber tip. (c, d) The retinal slice, attached to an artificial membrane, is mounted inside the chamber which is filled with extracellular solution (ECS). The fiber is gently placed in front of the slice under a water immersion objective. The fluorescence and the scattering of laser light inside the sample are detected simultaneously for each fiber position. For photography the light intensity was increased.

to 100 nW (OP-2VIS, FieldMate, Coherent, Santa Clara, CA, USA) which corresponds to the maximum light intensity that enters the area of a single endfoot under daylight conditions (Kopp and Lean, 2011).

Subsequently, a micromanipulator (Luigs & Neumann, Ratingen, Germany) gently placed the light source in front of a retinal slice within the recording chamber that was filled with extracellular solution (Figure 3.9). A single mode fiber with a small mode field diameter was used as small radiation source to illuminate individual Müller cell endfeet. I used guinea pigs because their Müller cells are the thickest among rodents. A single endfoot with an average diameter of 10 µm was clearly visible in slice preparations and was illuminated separately by the fiber when the distance between fiber and endfoot surface was 80 µm or less. The divergence of light limits this distance (see section 3.2.2). A laser diode with a wavelength of 532 nm was chosen because this wavelength fits to the absorption of photopigments in the guinea pig retina (section 3.1.1). Any optic function of the retina at least has to work for this spectral range. For the detection, the sample chamber was placed on a micropositioning stage (C7018-9012K, Märzhäuser, Wetzlar, Germany) under a water immersion objective (63x Achroplan, *NA* 0.95W, Zeiss, Oberkochen, Germany) of an upright microscope (AxioScope FS2MOT, Zeiss, Oberkochen, Germany) which was equipped with a laser scanning unit (LSM 510 Meta, Zeiss, Oberkochen, Germany). This experimental arrangement fulfilled all necessary requirements.

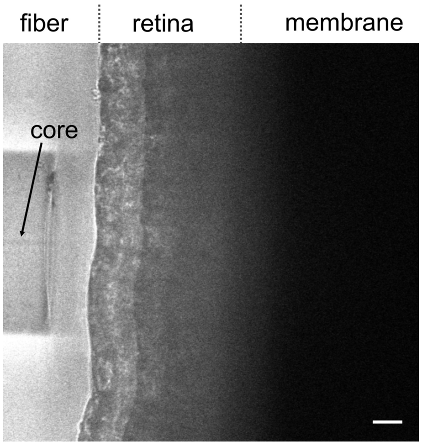

Figure 3.10: Positioning of the light source. Brightfield illumination is used to image the single mode fiber in front of the retina that is attached to a membrane. Even the tiny fiber core, through which the light propagates, is visualized and can be precisely positioned with respect to the cells. Scale bar 20 µm.

The transmission mode of the microscope allowed a precise location of the single mode fiber in front of the retinal slice (Figure 3.10) while the laser scanning mode was used to collect detailed information from the inside of the sample (see Figures 4.1 and 4.3). In a first channel, the stained structures (Mitotracker orange) were confocally excited and the resulting fluorescence was recorded by a first detector (Figure 4.1). A second channel of the laser scanning microscope recorded the scattered laser light within the retinal sample (Figure 4.3) and was finally overlayed with the first channel to identify scattering elements along the retinal light path (Figure 4.4). A micropositioning stage, on which the sample was mounted, was moved in steps of 2 µm along the optical fiber perpendicular to the light propagation. The stage was controlled by a self-written software based on LabView (National Instruments, Austin, TX, USA). Data were analyzed using the software IgorPro (Wavemetrics, Portland, OR, USA) and Mac Biophotonics ImageJ (ImageJ, Bethesda, MD, USA).

3.2.2 Local Light Illumination with Glass Fiber

In the optical fiber setup, a single mode fiber was used to transport light onto the retinal sample. The light in the glass fiber travels through a small core surrounded by a cladding material with a lower index of refraction. This layered composition of materials with different optical properties causes the trapping of light inside the core. The propagating light in a single mode fiber shows a Gaussian intensity distribution. After leaving the fiber, the light is no longer confined to a small area and the intensity decays radially with increasing distance from the fiber end (Figure 3.11).

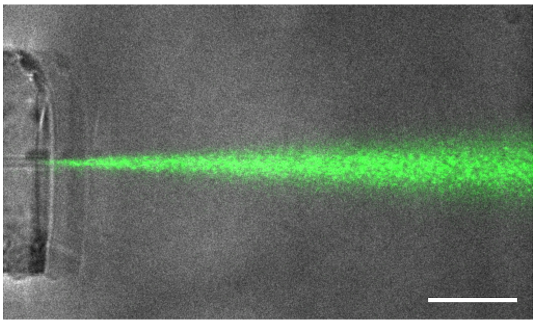

Figure 3.11: Light emanating from a single mode fiber. A single mode fiber is inserted into agarose gel to visualize the emanating light by scattering the light into an objective of a confocal microscope. The light coming from a small fiber core (approximately 3 µm) which is embedded in the cladding (125 µm) diverges through the medium. The image shows an overlay of an image taken in bright field illumination (grey) and a confocal image of the detected scattering of light (green). Scale bar 50 µm.

The Gaussian profile of the intensity distribution can be described by

$$I(r,z) = \frac{2P}{\pi w(z)^2} \exp\left(-\frac{2r^2}{w(z)^2}\right), \tag{3.1}$$

where P is the power of the beam, $w(z)$ the beam waist, r the transversal distance to the beam axis and z the longitudinal distance to the fiber core (Saleh and Teich, 1991). The beam waist $w(z)$ is defined as the radius where the power is decreased to $1/e^2 = 13\,\%$, thus, 86 % of the power is transported within a circle of the radius $r\ = w(z)$. For each transverse plane the beam width, given by

$$w(z) = w_0 \sqrt{1 + \left(\frac{z}{z_0}\right)^2}, \tag{3.2}$$

depends on the distance z (Figure 3.12). Here, w_0 describes the minimum value of the beam width at its narrowest point $z = 0$, namely the beam waist at the fiber tip (Bass, 1995).

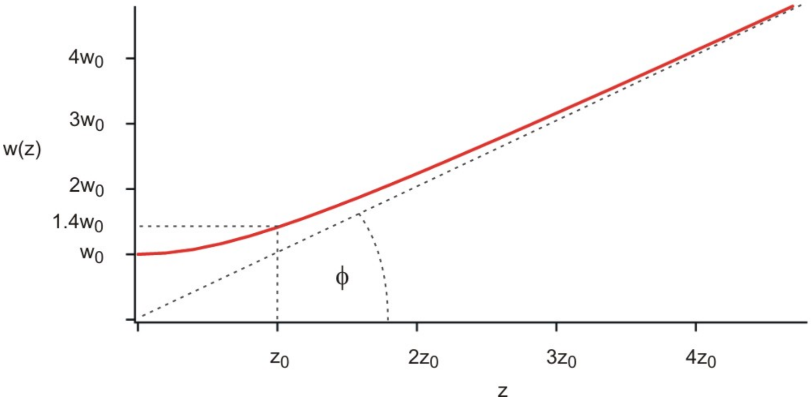

Figure 3.12: Beam width for a Gaussian beam emanating from a single mode fiber. The beam width $w(z)$ moderately increases from its mimimum value w_0 at $z = 0$ to $\sqrt{2}w_0$ at $z = z_0$, the Rayleigh range. For $z \gg z_0$ the beam width linearly increases with z.

For a slightly increased distance from $z = 0$ in a range of $0 < z < z_0$ the beam width $w(z)$ remains almost constant, at $z = z_0$ the width corresponds to 1.4 times the value of the beam waist

$$w(z_0) = \sqrt{2}w_0. \tag{3.3}$$

The length z_0 is called the depth of focus or Rayleigh range

$$z_0 = \frac{n\pi w_0^2}{\lambda}, \tag{3.4}$$

where n is the refractive index of the surrounding medium and λ the wavelength of the laser light. Finally, this results in

$$w(z) = w_0 \sqrt{1 + \left(\frac{z\lambda}{n\pi w_0^2}\right)^2}. \tag{3.5}$$

For transverse planes which are more distant from the Rayleigh range (i.e. $z \gg z_0$) equation 3.5 can be approximated to

$$w(z) \approx \frac{\lambda}{n\pi w_0} z, \tag{3.6}$$

where the beam width is linearly related to z. This behavior can be also described by the half-angle ϕ enclosed by $w(z)$ (for $z \gg z_0$) and the beam axis

$$w(z) = \phi z, \tag{3.7}$$

$$\phi = \frac{w_0}{z_0} = \frac{\lambda}{n\pi w_0}. \tag{3.8}$$

The full angle usually serves as a measure of the beam divergence and is given by

$$\Phi = 2\phi = \frac{2\lambda}{n\pi w_0}. \tag{3.9}$$

Consequently, the divergence of a light beam is a function of the beam waist, the wavelength and the refractive index of the medium where the light beam propagates through (Saleh and Teich, 1991).

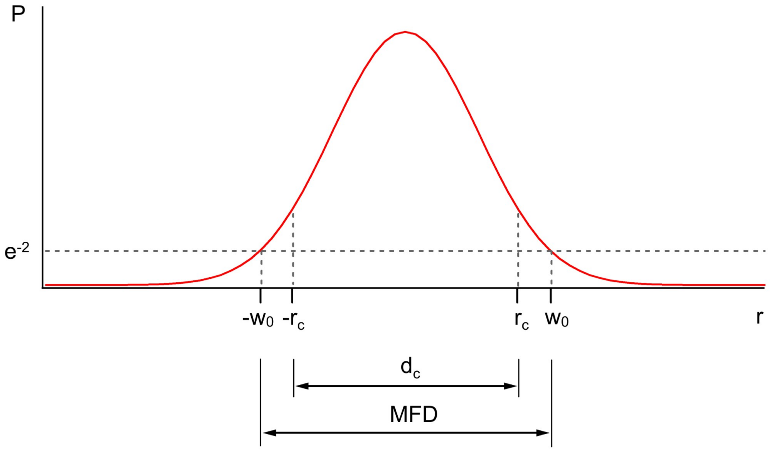

Figure 3.13: Mode field diameter. Most of the optical power P propagates within the fiber core (d_c, diameter of the core; r_c, core radius) whereas a small portion of light is distributed in the cladding material close to the core ($r > |r_\mathrm{c}|$). The mode field diameter *MFD* is a measure of the effective beam width, i.e. the beam waist w_0 of a Gaussian beam across the endface of an optical fiber.

The fiber used in the experiments was a single mode fiber. Its relatively small core diameter d_c of around 3 µm only allows the propagation of the fundamental zero mode LP_{01}. However, the propagation of light in single mode fibers is influenced by an additional phenomenon occurring at the core-cladding boundary where most of the light is reflected back into the core by total internal reflection. Considering this process by using the wave theory, the light intensity behind the boundary is not dropped to zero, however an evanescent wave is formed whose intensity exponentially decays with an increasing distance from the surface of the core. Therefore, light slightly penetrates into the less dense cladding material which in turn increases the effective area of the light source. The beam width at which the optical power is decreased to $1/e^2$ of its peak power along the fiber axis is called mode field diameter MFD, it is related to the beam waist by

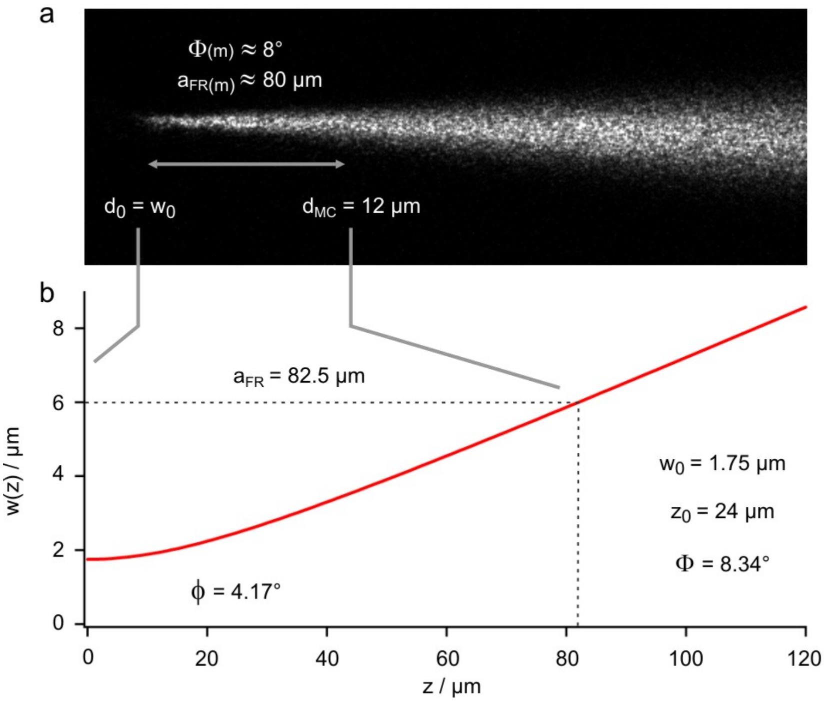

Figure 3.14: Beam shape of the used single mode fiber. (a) The beam is visualized to estimate the fiber-retina distance $a_{\mathrm{FR(m)}}$ at which one Müller cell endfoot ($d_{\mathrm{MC}} \approx 12$ µm) is still illuminated. At a beam diameter of 12 µm, a distance $a_{\mathrm{FR(m)}} \approx 80$ µm and an angle of $\Phi_{\mathrm{m}} \approx 8°$ was measured (m, measured). (b) The light cone of the single mode fiber (460HP, Thorlabs, Newton, NJ, USA) for a wavelength of 532 nm and a surrounding medium with a refractive index of $n = 1.33$ is illustrated by using equation 3.5. The computed parameters $\Phi = 8.34°$ and $a_{\mathrm{FR}} = 82.5$ µm match the measured values. In the experiments a_{FR} was usually between 10 and 30 µm.

$$w_0 = \frac{MFD}{2}. \tag{3.10}$$

The mode field diameter is slightly larger than the core diameter d_c as shown in Figure 3.13. The mode field diameter of the used fiber (460HP, Thorlabs, Newton, NJ, USA) was given by 3.5 ± 0.5 µm, thus the beam waist w_0 was approximately 1.75 µm (equation 3.10). By using equation 3.4 the Rayleigh range $z_0 = 24.05$ µm was calculated for a physiological solution with a refractive index of $n = 1.33$ and a laser diode with a wavelength of 532 nm. Consequently, the calculated value for the divergence angle Φ was $8.34°$ (equation 3.9).

By inserting the fiber into a fluid agarose gel ($n \approx 1.33$), the laser light emanating the fiber was visualized by scattering into the objective. The angle of divergence was measured and corresponded to the calculated value as shown in Figure 3.14. Since the glass fiber acts as small light source to illuminate individual Müller cells, the divergence of light limits the distance between fiber and sample. The area of a Müller cell endoot varies in dependence on the retinal region, however, the maximum diameter is around 12 µm. A circular area with this diameter is illuminated if the fiber-retina distance a_{FR} is around 80 µm (Figure 3.14). To ensure that only single Müller cells are in the light spot, the distance in my experiments was usually chosen between 10 and 30 µm.

3.2.3 Both Way Imaging Setup Combined with Local Light Illumination

The inner and outer segments of photoreceptors act as wave guides. Light is kept inside the segments and is efficiently transported along their entire length which increases the probability of being absorbed by the light-sensitive pigments (section 2.2.3). Due to this mechanism, no or less light is scattered in sideward direction out of the structures. Consequently, for studying the distribution of light over an area of rod and cone photoreceptor cells, the transmitted light should be detected behind the retina to obtain a two-dimensional illumination pattern that can be assigned to the corresponding cells. In a slice preparation, the retina is attached to a membrane, thus no imaging unit can be placed behind the photoreceptors. Effort was spent to replace the membrane by a transparent material, e.g. by thin slices of cover slip, however, an immobilization of the tissue onto the glass surface remained inconclusive. The only appropriate way to image the receptor light pattern was to spread the retina horizontally onto the bottom of a transparent chamber pointing the photoreceptor cells towards a microscope objective. In this arrangement, an opposing objective directed to the inner retinal surface could be used for simultaneous localization of Müller cells. However, this assembly implies another technical problem as the outer shell of the optical fiber is around 125 µm in diameter and by placing the fiber between objective and retinal surface, the Müller cells are obscured by the light source. Thus, a setup was needed which simultaneously detects Müller cells and photoreceptors inside the vital tissue combined with additional local light stimulation.

For this purpose, an upright imaging unit was mounted on top of an inverted microscope (Axiovert 100M, Zeiss, Jena, Germany) equipped with a conventional laser scanning device (LSM510, Zeiss, Jena, Germany) (Figure 3.15; Agte et al., 2011). The stained retina was placed in a perfusion chamber, with the inner (vitread) surface down, to observe confocal images from below (Figure 3.16 a). High resolution images from different depths were obtained with a high-numerical objective (40x C-Apochromat, *NA* 1.2W, Zeiss, Jena, Germany) and recombined to provide detailed information about the shape, distribution and orientation of the Müller glial cells (Figure 3.16 c). In this experimental arrange-

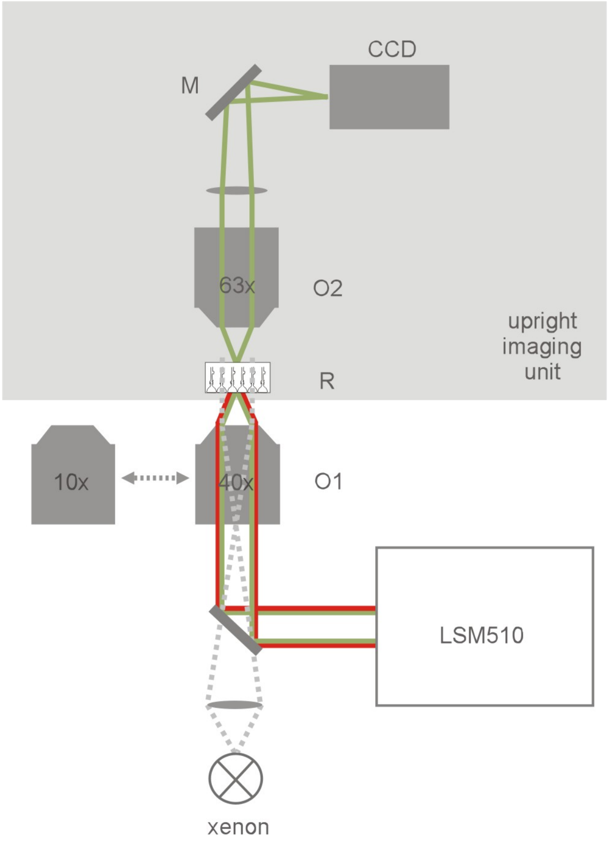

Figure 3.15: Both way imaging of the retinal tissue combined with local light illumination. The retinal wholemount (R) is spread, with the Müller cell endfeet down, onto the bottom of a sample chamber. To obtain images from both sides of the retina, the chamber is placed between two opposing objectives. The objective (O1) below the chamber belongs to a microscope equipped with a laser scanning unit. Optically sectioned confocal images of the dye-loaded Müller cells within the retinal tissue are taken by a 40x objective. The 40x objective is replaced by a 10x objective to apply light in physiological direction onto the inner retinal surface, either using the xenon lamp for widefield illumination or the stationary focused laser beam of the scanning unit for localized illumination. The opposing objective (O2) above the sample chamber collects the transmitted light and after passing a convex lens (L), a mirror (M) projects the light onto the chip of a CCD-camera (CCD). Two-dimensional light patterns are recorded and can be assigned to the photoreceptor cells.

ment, it was possible to image the sample from above in transmission mode using the widefield illumination of the xenon lamp from the Axiovert and the upright objective (63x Achroplan, *NA* 0.95W, Zeiss, Jena, Germany) to collect the light transmitting through the sample (Figure 3.16 b). All components of the custom-built imaging unit were mounted on an optomechanical construction (Linos, Göttingen, Germany) which consisted of an objective, a convex lens ($f = 100$ mm, Linos, Göttingen, Germany), a plane mirror (Linos, Göttingen, Germany) and a CCD camera (CF 8/5 MX Kappa, Gleichen, Germany). The camera was read out by using a frame grabber (GA-VD207, Georgia Technology, Wis Technologies Inc., Taipei Hisen, Taiwan) and the WinDVD Creator software (InterVideo, MountainView, California).

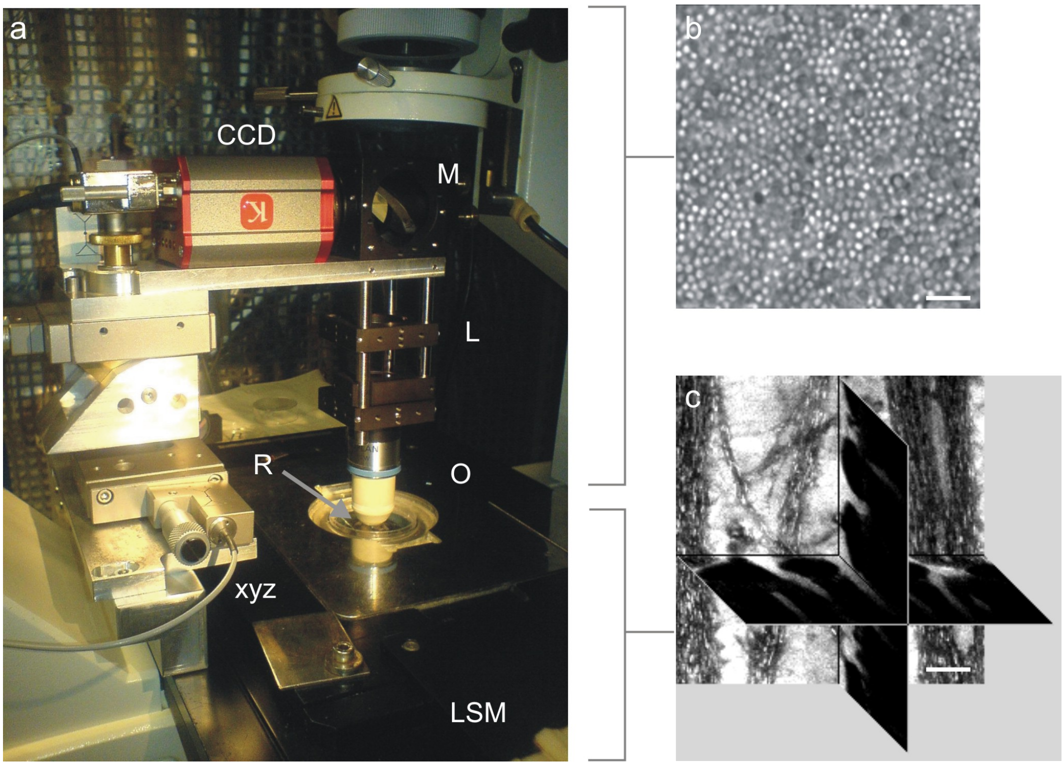

Figure 3.16: Imaging the retina from both surfaces. (a) Upright imaging setup mounted on top of a laser scanning microscope (LSM). The retinal tisssue (R) is placed at the bottom of a transparent chamber with the Müller cells facing the objective (not shown) of the confocal microsope. Confocal images of the dye-filled cells in the desired resolution are taken from below. The upright unit from above images the light transmission through the retina. The upright unit consists of a water immersion objective (O), a convex lens (L), a mirror (M) and a CCD-camera (CCD). All optical components are mechanically combined with a xyz-drive (xyz) to adjust the upright setup with respect to the optical path of the laser scanning microscope. (b) Transmission image of the photoreceptor segments taken with the upright imaging unit. (c) Volume view of a confocal stack consisting of high-resolution images of the dye-filled retina (Mitotracker green). Single fluorescent Müller cells can be localized inside the retinal tissue. Precise information about their shape and orientation are given. Scale bars 10 µm.

To overcome the described problem of combining this setup with an additional illumination of single Müller cells, the internal laser light ($\lambda = 543$ nm) from the confocal microscope was used for local light stimulation. A low numerical objective (10x, *NA* 0.3, Zeiss, Jena, Germany) was stationary focused at a semi-angle of maximal 13°. The full acceptance angle of the endfoot, estimated from the refractive index difference between the glial cell and the vitreous body, is at least 22° and is described as physiological acceptance angle (see section 3.2.5). Thus, the full projection angle of the objective matches the value under physiological conditions. Subsequently, confocal images showing the three-dimensional localization of Müller cells, taken with the 10x objective, were used to accurately apply the laser focus at the preferred position of the retinal surface (Figure 3.17). Finally, the imaging unit on top of the inverted microscope captured the light emerging from the photoreceptor segments. This illumination pattern can be compared with the corresponding photoreceptors and the position of the stationary laser beam with respect to the Müller cells at the opposite surface of the retina. Image scales for both the inverted and the upright imaging units were determined by acquiring images of a standard scale bar (Zeiss, Jena, Germany). The software IgorPro (Wavemetrics, Portland, OR, USA) and Mac Biophotonics ImageJ (ImageJ, Bethesda, MD, USA) were used for data analysis.

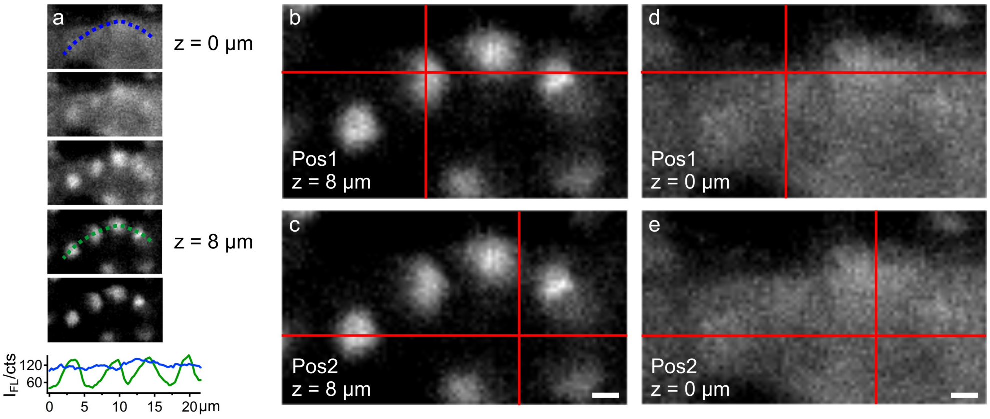

Figure 3.17: Positioning of the laser light illumination onto the retinal tissue. (a) Confocal stack ($z = 2$ µm) of a group of labeled Müller cells (Mitotracker green) taken with a 10x objective. The endfeet of Müller cells are densely packed at the retinal surface ($z = 0$ µm), thus, the border between two adjacent endfeet cannot be resolved by the 10x objective. The fluorescence intensity I_{FL} along the blue dotted line, shown in the diagram below the confocal stack, is nearly homogeneous without distinct fluctuations. With increasing retinal depth, single bright spots appear indicating Müller cell processes in the inner plexiform layer. Individual Müller cells are detected at a depth of around 8 µm, the fluorescence along the green dotted line fluctuates between low and high intensities. (b, c) The software of the confocal microscope is used to define the xy-position of the stationary focused laser light (red cross indicates Pos1, respectively Pos2) at a retinal depth of around 8 µm. (d, e) Finally, the z-drive of the microscope is used to set the focal spot at $z = 0$ µm to simulate an illumination of light under physiological conditions. The numerical aperture (0.3 *NA*) of the objective corresponds to the acceptance angle of the endfoot. Scale bar 3 µm.

3.2.4 Local Light Illumination with Objective

To illuminate individual Müller cells in the both way imaging setup, an objective with a 10x magnification and a numerical aperture of 0.3 was used to focus the confocal laser light onto the sample. The numerical aperture NA is related to the spreading of light in the far field of the focal spot by

$$NA = n \sin \phi, \tag{3.11}$$

where ϕ describes the half-angle of the light cone and n the refractive index of the medium between the front lens of the objective and the coverglass. With $NA = 0.3$ and $n = 1$ for air, the angle ϕ of the objective is around 17° (ϕ_1 in Figure 3.18). After travelling through the cover glass and the aqueous solution in which the sample was placed, the light reaches the sample under an angle of approximately 13° (ϕ_2 in Figure 3.18). The angular acceptance

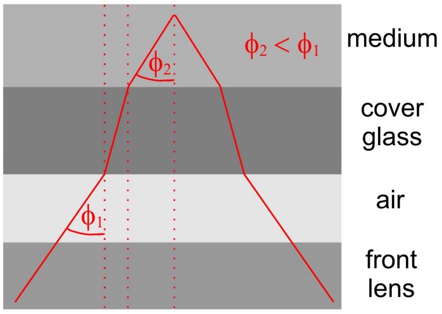

Figure 3.18: Angle of light illumination. The illumination angle ϕ_2 of the sample can be calculated by using Snell's Law for light travelling from the front lens through three different media (air, glass, extracellular solution). The angle ϕ_1 describes the incoming angle of the objective in air.

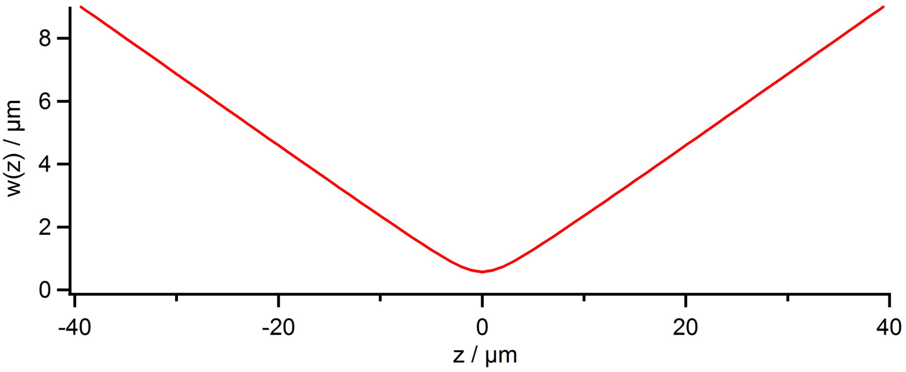

Figure 3.19: Beam width for a Gaussian beam emanating from a 10x objective. The light converges to a focal spot with a beam waist of about $w_0 = 0.57$ µm over a length of $2z_0 = 5.05$ µm before the beam width again increases with an angle of 13°.

of the retinal sample will be discussed in more detail in the next section (section 3.2.5). The confocal laser light with a wavelength of 532 nm follows a Gaussian distribution as described in section 3.2.2. Figure 3.19 illustrates the beam width for the objective after equation 3.5 where the calculated values for the beam waist and the depth of focus are $w_0 = 0.57$ µm and $z_0 = 2.52$ µm respectively.

3.2.5 Discussion of the Applied Methods

In this section, the used illumination methods will be discussed regarding their application as physiological light sources. In the eye the light rays passing the vitreous body are projected at the sensitive retinal tissue. Franze et al. (2007) found that isolated Müller cells possess wave guide properties to transport the incoming light through the retina (see section 2.2.3). Assuming that Müller cells in the vital tissue also act as wave guides, each light ray impinging the tissue with an incident angle below the acceptance angle of the Müller cell will be guided by these glial cells. The angle of acceptance describes the angular range over which a light ray can enter a fiber to propagate through its core. If the light inside the cell is guided by total internal reflection, the angle can be estimated by the refractive index difference between the core, i.e. the Müller cell, and the surrounding tissue. The acceptance angle ϕ_a depends on the critical reflection angle at the Müller cell-tissue boundary and is given by

$$\sin\phi_\mathrm{a} = \frac{1}{n_\mathrm{VB}}\sqrt{n_\mathrm{MC}^2 - n_\mathrm{ET}^2} = \frac{1}{n_\mathrm{VB}} NA, \qquad (3.12)$$

with the refractive indices of the Müller cell $n_\mathrm{MC} = 1.380$, the vitreous body $n_\mathrm{VB} = 1.335$ and the extracellular tissue n_ET wherein the fiber is embedded. To estimate the minimum possible angle, the largest refractive index among the neuronal tissue, i.e. refractive index of the neuronal soma $n_\mathrm{ET} = 1.358$, was taken for the calculation (Franze et al., 2007). Consequently, the calculated minimum angle is $\phi_\mathrm{a} = 10.59°$. The numerical aperture NA characterizes the acceptance cone, i.e. the angular range of the Müller cell, to emit or accept light (Saleh and Teich, 1991).

To efficiently couple laser light into a Müller cell, not only the size of the light source but also the angular spread has to be considered. The focal dimension of a Gaussian laser beam is inversely related to its divergence as described by equation 3.8. The smaller the beam waist the larger the divergence angle, i.e. the increase of the beam diameter by an increasing distance to its source. The beam width for both light sources after equation 3.2 is demonstrated in Figure 3.20. Obviously, the divergence angle of the light from the fiber ($\phi = 4.17°$) is lower than of the 10x objective ($\phi = 13.03°$), however, both light sources should fulfill the condition to stay in or close to the angular acceptance range of the Müller

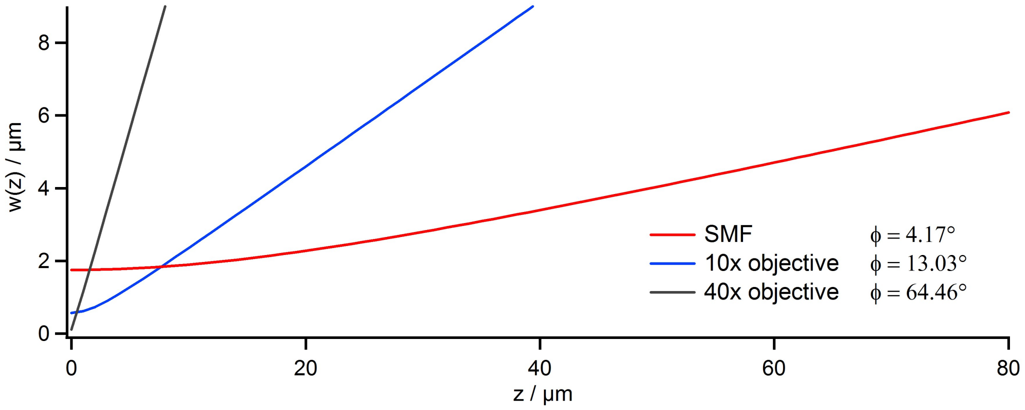

Figure 3.20: Comparison of three Gaussian beam curves. The beam waist of a single mode fiber (SMF), a 10x and a 40x objective are small enough to act as light sources for single Müller cells. However, the divergence angle limits the application only to the SMF ($\phi = 4.17°$) and the 10x objective ($\phi = 13.03°$) because the 40x objective with its smallest beam width possesses a divergence angle of $\phi = 64.46°$ that exceeds the acceptance range of the Müller cell.

cell which is at least $\phi = 10.59°$. In line with this, the diagram also illustrates why the 40x objective, used to image Müller cells in high resolution in the both way imaging setup, was replaced by an objective with a 10x magnification for sample illumination. The angle of divergence $\phi = 64.46°$ far exceeds the acceptance angle, thus, most of the light would not be trapped within the cell but would pass the tissue by scattering through the adjacent neuronal tissue.

	λ /nm	ϕ /°	$2w_0$ /µm	z_0 /µm	$2z_0$ /µm
SMF	532	4.17	3.50	24.05	-
10x objective	543	13.03	1.14	2.52	5.05

Table 3.2: Beam parameters. A single mode fiber (SMF) and a 10x objective are used as light sources to simulate the physiological illumination of individual Müller cells.

However, also for the used light sources it is sufficient to minimize the angular effect which can be achieved by placing the sample close to the Rayleigh range z_0, the distance where the light beam shows no considerable divergence. All previously described parameters, including the Rayleigh range, of both light sources are summarized in Table 3.2. In contrast to the fiber, the distance, over which the beam width stays nearly constant, is twice the Rayleigh range for an objective. Even if this distance of the 10x objective is approximately 5 times lower than for the fiber, the objective can be used since its enormous working distance (approximately 5 mm) guarantees a contact-free and convenient setting of the focal spot onto the sample. To sum up, the fiber as well as the 10x objective were considered to be appropriate light sources to apply light onto the retina (Agte et al., 2011).

4 Experimental Results

The main focus of the present work is to verify the light guiding mechanism of Müller cells in the vital retinal tissue. Furthermore, this thesis provides insight into the interaction of light with living cells and cellular structures embedded within their natural environment. Because of its significance in vision, the retina plays a key role in understanding how light behaves in a tissue composed of elements which fundamentally differ in their anatomical structure (see section 2.2.1). The morphology of the retina is well known, its layered design allows a clear separation of the cellular components which facilitates the assignment to the Müller cell-dependent behavior of light in the particular layer. Altogether, the present work investigates the complex optical landscape of the retina with respect to Müller cells.

In this chapter, the visualization of the transretinal light propagation with a newly established method will be presented in detail. Furthermore, the data analysis of the resulting beam structure is introduced which finally identified Müller cells to play a decisive role in light propagation. In order to prove this finding, a statistical test procedure was performed. Finally, the biological relevance of the Müller cell-provided light propagation with respect to the light-sensitive receptor cells was analyzed by a second imaging setup and by a morphological study of both cell types.

4.1 A New Method to Visualize the Transretinal Lightpath

To visualize the light along its natural path within the intact retinal tissue, experiments were carried out on a newly established setup whose technical design was already introduced in section 3.2.1 (Agte et al., 2011). The setup consists of an illumination unit based on glass fiber optics and a detection unit provided by conventional confocal microscopy. In the course of this section, I will demonstrate all steps required for an implementation of the system up to the final measurement.

During the whole experiment, special attention was paid to the vitality of the retinal sample. To maintain all vital functions, the tissue preparation was performed under elaborate conditions avoiding any artefacts induced by chemical or physical stress (see sections 3.1.2 and 3.1.3). In the end of this gentle preparation process, vital retinal slices, attached to an artificial membrane, were fixed in a chamber filled with physiological solution and placed onto a stage of an upright confocal microscope (see section 3.1.5). Confocal microscopy is a powerful tool widely-used in life science to obtain high-resolution optical images of biological tissues (Sheppard and Shotton, 1997; Pawley, 2006). Advantages of confocal detection for the imaging of tissues include an increased signal-to-noise ratio and a z-sectioning of the sample which is achieved by a highly limited depth of focus. Thus, the confocal method represents an appropriate tool to allocate changes of the light propagation to specific cellular structures within the intact retina.

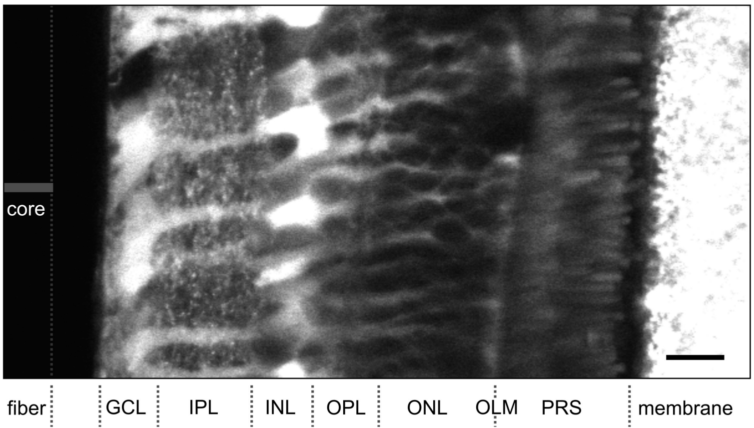

Figure 4.1: Confocal image of the vital retinal sample, recorded by a first confocal channel. Müller cells, photoreceptor segments and the nitrocellulose membrane, to which the retina is attached, are loaded by the fluorescent dye Mitotracker orange. All three nuclear layers (GCL, ganglion cell layer; INL, inner nuclear layer; ONL, outer nuclear layer) and both plexiform layers (IPL, inner plexiform layer; OPL, outer plexiform layer) are clearly assigned by the Müller cell morphology. A fiber is gently placed in front of the retina to apply laser light onto the vitread surface of the slice preparation. (OLM, outer limiting membrane) Scale bar 20 µm.

The confocal image in Figure 4.1 demonstrates the fluorescence signal along the retinal cross section, evoked by a vital dye, which became predominantly incorporated into Müller cells, photoreceptor segments and the supporting membrane. Obviously, the predominantly stained Müller glial cells elongate through the entire retinal tissue (Reichenbach and Birkenmeyer, 1984). Their densely packed endfeet at the inner retinal surface funnel into individual processes spanning the inner plexiform layer (IPL) which mainly consists of synaptic connections between neuronal cells. In the following inner nuclear layer (INL), the intensively stained somata of Müller cells are located slightly lateral from their stem processes which again bridge a second synaptic layer (outer plexiform layer, OPL) before they get splitted into many thin branches in the following outer nuclear layer (ONL). Altogether, the morphological structure of Müller cells is different for virtually every retinal compartment. Müller cells form a soft matrix surrounding all neuronal structures (Lu et al., 2006; Lu et al., 2011), in particular, they tightly envelope the rigid neuronal soma in the nuclear layers while the shape of their processes seems to be less affected by the synaptic endings in both plexiform layers. Figure 4.1 additionally demonstrates that the photoreceptor segments, labeled by the same fluorescent dye, arise at the outer limiting membrane (OLM). Thus, each part within the retina could be clearly identified only by the fluorescence of Müller cells and photoreceptor segments recorded by a first confocal channel providing high resolution images of the retinal cross section. Furthermore, considerable fluorescence of the membrane behind the retina was observed.

To avoid loss of information caused by sample drifting during the experiment, a small confocal z-stack consisting of about five images was recorded. But as explained before, a precise slicing allowed that only one confocal plane was chosen for analysis (see section 3.1.5). This ensured that changes of light were not obscured by interactions with the overlaying tissue. If all structures of interest were in the same focal plane, i.e. had the same amount of overlying tissue, all changes of light along the light path were comparable. This alignment of the retinal slice perpendicular to the objective could be controlled by the fluorescence of Müller cells. Only samples showing single Müller cells visible from the retinal surface to the outer limiting membrane, i.e. all parts of the cell are located at the same z-level, were used for data acquisition.

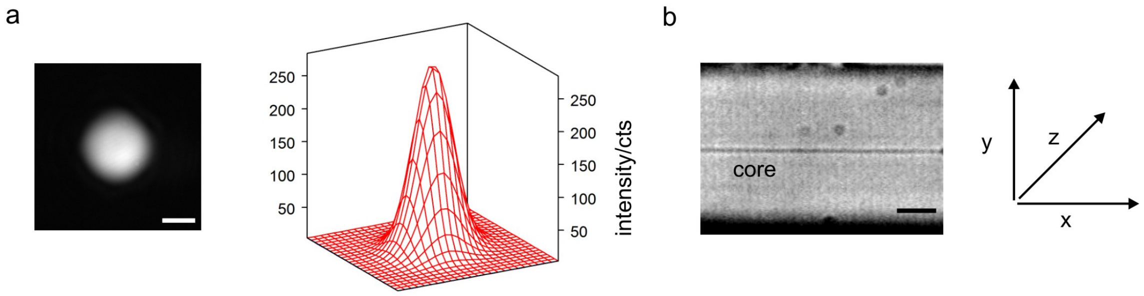

Figure 4.2: Calibration of the fiber illumination. (a) The laser light recorded from the tip of the fiber shows a round intensity profile (left). Only fibers with a beam profile close to a Gaussian distribution were taken for the experiments (right). Scale bar 250 µm. (b) The fiber core, visualized in the transmission mode of the microscope, is used to align the fiber in x, y, and z-direction. In the end of this alignment procedure, the core appears as an almost homogeneous line in the z-focus of the objective (63x, *NA* 0.95W). Scale bar 20 µm.

Besides high resolution imaging, another advantage of confocal microscopy in comparison to common fluorescence techniques is the relatively low excitation intensity leading to reduced bleaching artefacts. Accompanied by that, the functionality of the light-sensitive retina is less affected by light coming from the small focal volume which rapidly scans the sample as shown for example on ganglion cells (Otori et al., 1998), glial cells (Pannicke et al., 2006; Karl et al., 2011; Srienc et al., 2012) or by the use of confocal imaging in medical ophthalmology (Seeliger et al., 2005). Thus, the behavior of light within the retinal tissue could be analyzed without any disturbing influences of other light sources.

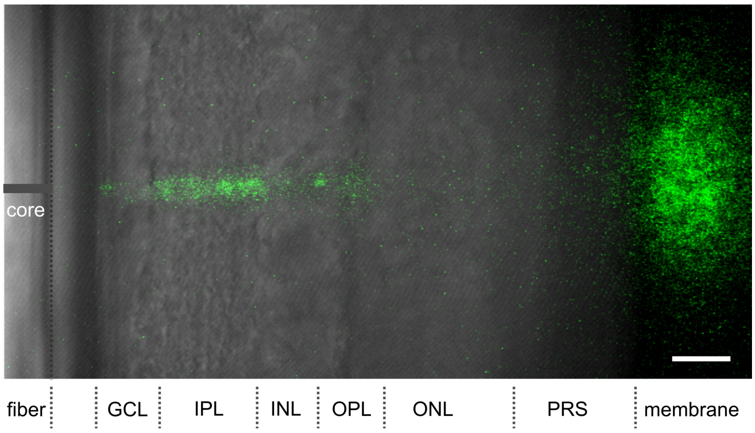

Figure 4.3: Scattering of light inside the sample, recorded by a second confocal channel. Laser light emanating from the core of the fiber interacts with celluar structures along its way through the retinal cross section towards the artificial membrane. The scattering of light evoked by the sample was collected through an objective of a confocal microscope. Scale bar 20 µm.

In order to mimic the natural light path, I used a single mode fiber which was placed in front of the slices perpendicular to the optical axis of the microscope (Figure 4.3). Before each experiment, the illumination of the optic fiber was calibrated to ensure the same illumination cone as obtained in the control experiment with agarose gel (Figure 3.14). Inserting the fiber into a scattering solution would contaminate the fiber core and disable it for further experiments. Consequently, the beam profile was controlled by imaging the light that exits the tip of the fiber (Figure 4.2 a). To check if the fiber showed the typical Gaussian intensity distribution, an intensity profile of the roundish spot was fitted by a Gaussian function. Then the fiber was turned around 90° (see Figures 3.9 and 3.10). In this position the fiber core became visible and was used to align the fiber in x, y and z-direction (Figure 4.2 b). The intensity of the laser light and the distance between fiber and retina were adjusted with respect to single Müller cells (sections 3.2.1 and 3.2.2). Thereby, the small mode-field diameter and low divergence of the light emanating from the fiber core were advantageous for an illumination of individual Müller cell endfeet (Figure 3.14). After the positioning of the fiber core in front of the vitread surface (see section 3.2.1), the behavior of fiber-provided laser light within the retinal tissue was observed by a second confocal channel running in detection mode which recorded the green laser light that was scattered into the objective (Figure 4.3). In addition to intraretinal scattering, the second channel also revealed scattering from the membrane to which the retina was attached since the membrane served as an artificial screen indicating the transmitted light behind the retina. Finally, an overlay of the information from both confocal channels was used to identify scattering elements along the retinal light path and to detect the spatial distribution of light transmitted by the vital tissue (Figure 4.4). Consequently, the described method provides an imaging of all retinal layers together with a visualization of the incoming, the propagating and the transmitted light with respect to Müller cells.

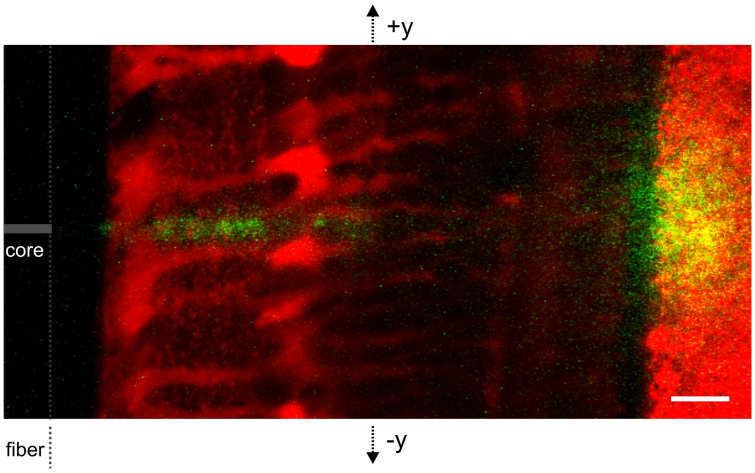

Figure 4.4: Pathway of light through the vital retina. An overlay of the sample fluorescence (first confocal channel, see Figure 4.1) and the light scattering (second confocal channel, see Figure 4.3) provides detailed information about the interaction of light in dependence on the cellular structures within the tissue. To observe changes in the light behavior with respect to the beam position, the sample was stepwise moved perpendicular to the fiber axis in y-direction. Scale bar 20 µm.

4.2 Behavior of Light in Dependence on the Beam Position

Interactions of light within the sample were assessed by changes in light scattering during a stepwise movement of the retina perpendicular to the fiber axis. The stage to which the sample was attached was moved in equal steps of 2 µm. After each step, the information inside of the sample was recorded by confocal detection as decribed in the previous section. Starting from an arbitrary position of the fiber core in front of the vitread surface, one portion of light was scattered within the retina while another amount of light was projected to the membrane where it appeared as bright spot representing the transmitted light (Figure 4.5 a). The scattering inside the retina predominantly arose from interactions of the incoming light with cellular elements in the plexiform layers, the nuclear layers virtually showed no evident signal (Agte et al., 2011). In contrast to the modest expansion of intraretinal light scatter, the membrane caused a scattering of light distributed over a wide area. An overlay of scattered light from the sample (green) with intensively stained fluorescent structures (red) often displayed a yellow color. In some samples, strong labeling particularly occurred at the artificial membrane as shown in Figure 4.5.

Finally, a stepwise motion of the sample out of its initial position is demonstrated (Figure 4.5, b-h). By comparing all resulting images in each fiber position, the propagation of light

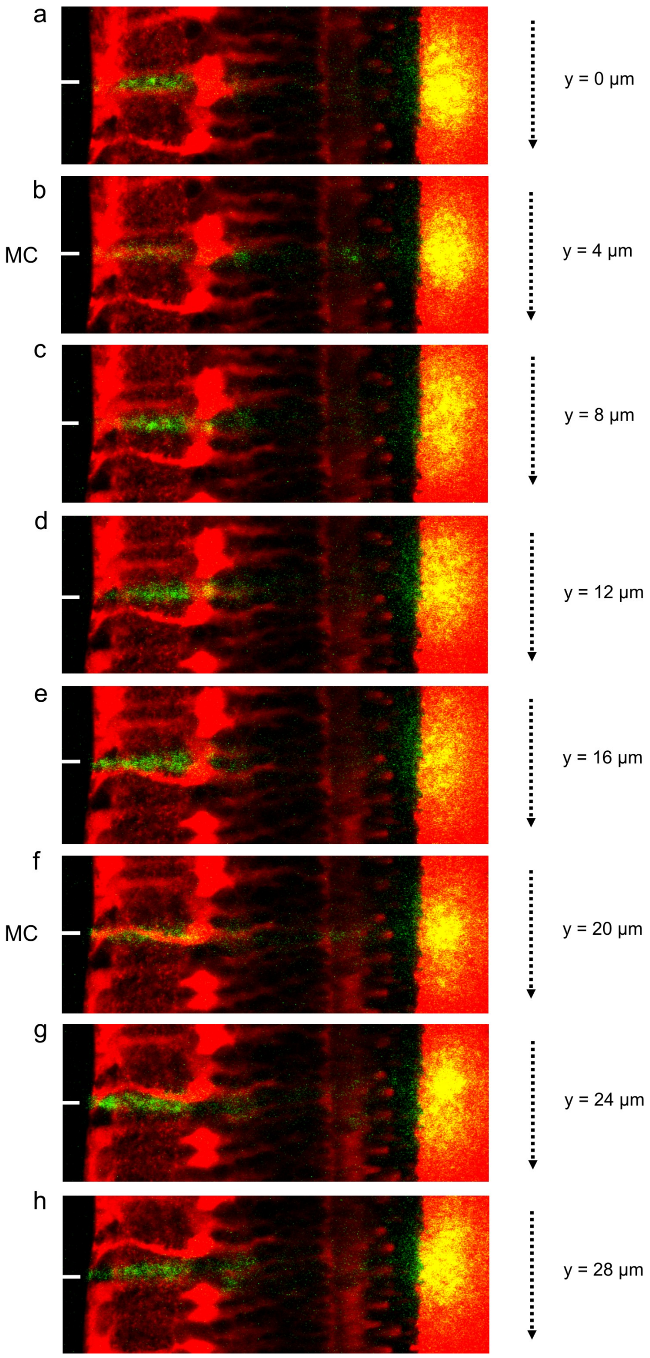

Figure 4.5: Positioning of the incoming light influences the retinal light propagation. The scattered light within the sample (green) and the transmitted light projected to the membrane (yellow) varies during a stepwise movement of the retina (2 µm steps, every second position shown) along the light-emitting fiber core (position indicated by a white line). Changes in the light structure occur in dependence on Müller cells. When a Müller cell is directly placed in the lightpath of the fiber (indicated by 'MC' in front of the retinal surface), the light scattered by the retinal tissue becomes less and light transmitted to the membrane appears as a small intensive spot with sharp boundaries.

changed in dependence on the beam position with respect to Müller radial glial cells. If the fiber was moved into a position where the fiber core and the axis of a Müller cell were oriented along a line (Figure 4.5 b), the prominent scattering in the inner plexiform layer decreased. Furthermore, the transmitted light was now confined to a small area with high local light density. Some further steps in y-direction again caused a misalingment between the light emitting core and the Müller cell which again led to a wide spatial distribution of light at the artificial membrane and an immediate return of scattering within the plexiform layers (Figure 4.5, c-e). The described observation became clearer for a second Müller cell that was even more co-aligned with the fiber core (Figure 4.5 f). This can be derived by the strong fluorescence caused by an orientation along the focal plane of the objective, the same z-level the fiber core was previously positioned. Especially the light spot at the membrane became very small before some additional steps in y-direction again abolished this effect (Figure 4.5, g and h). Consequently, Müller cells influence the interaction of light within the retinal tissue.

4.3 Transretinal Light Propagation

In order to analyze the influence of Müller glial cells in transretinal light propagation, two images were chosen that clearly represent the described phenomenon (Figure 4.6). In the first image (Figure 4.6 a), the fiber core, indicated by a line, was placed between two Müller cell processes while the second image (Figure 4.6 b) shows a situation where Müller cell and fiber core were perfectly co-aligned similar to Figures 4.5 (b) and (f). The resulting light pattern for both positions was analyzed regarding its distribution within the retinal sample (Figure 4.6, c and d). The scattered light was estimated by profile plots reflecting the averaged light intensity across 25 pixels (corresponding to approximately 7 µm) around the red and blue lines drawn along the different cellular layers. A clear discrimination of the layered composition inside the retina was achieved by the Müller cell morphology (Figure 4.5, a and b), as described in section 4.2.

The light intensity for all retinal parts and the membrane is shown in Figures 4.7, 4.8, 4.9 and 4.10. Intensity profiles of the scattered light for position 1 and position 2 along the lines in Figure 4.6 are indicated by blue and red color respectively. At the inner limiting membrane, the border between the vitreous body and the retina, light scattering was observed for both positions (Figures 4.7) where the maximum light intensity for position 2, with a Müller cell in the light path, decreased by approximately 50 % compared to position 1. Due to a refractive index mismatch which the light experiences during the transition from the lower refractive vitreous liquid ($n = 1.335$; Valentin, 1879) to the higher refractive retina ($n \approx 1.36$; Valentin, 1879; Nordenson, 1934; Chen, 1993;

Franze et al., 2007), the light gets partially reflected backwards (see section 2.2.3). The light that enters the ganglion cell layer is scattered to a lower extent, however, the difference between the two positions is still recognizable (Figure 4.8 a). This difference between the red and blue curve was strongly increased within the following inner plexiform layer, since the maximum of light scattering in position 1 was twice as large as in position 2 (Figure 4.8 b). In the inner nuclear layer the curve progressions of the resulting line profiles were the same (Figure 4.8 c). Both positions revealed lower intensity values with amplitudes comparable to Figure 4.8 (a).

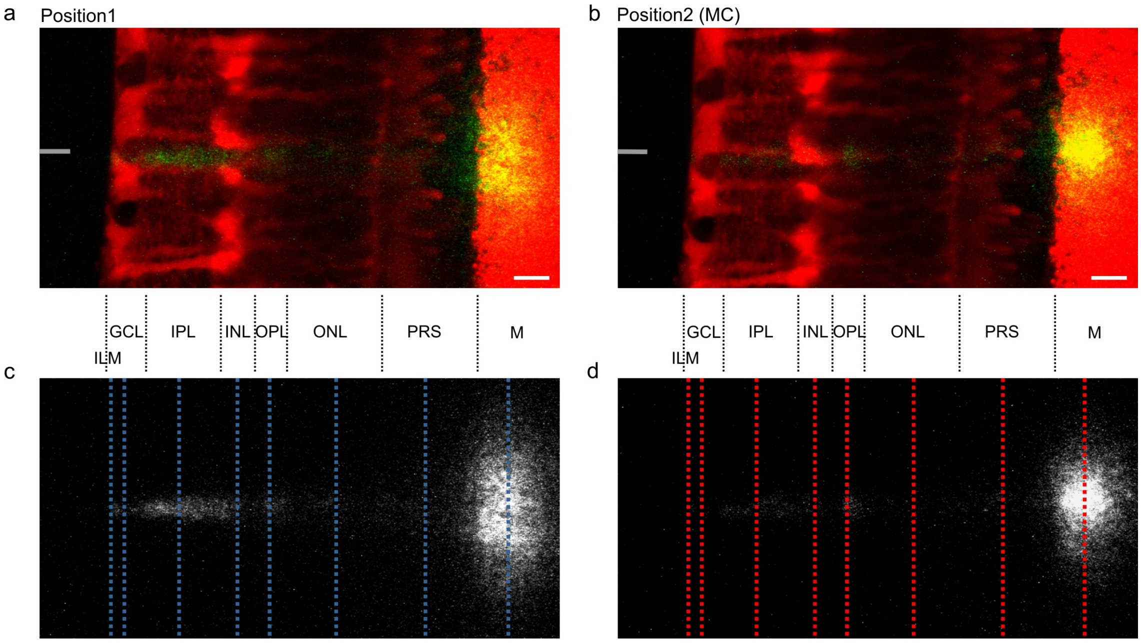

Figure 4.6: Analysis of the Müller cell-dependent light propagation. (a, b) The fluorescence (red) is used to identify different parts of the sample, for a situation with (b) and without (a) a Müller cell in the light path. (c, d) The resulting light scattering in each part can be studied by intensity profiles along lines drawn perpendicular to the light propagation (blue, without Müller cell; red, with Müller cell). (ILM, inner limiting membrane; GCL, ganglion cell layer; IPL, inner plexiform layer; INL, inner nuclear layer; OPL, outer plexiform layer; PRS, photoreceptor segment layer; M, membrane) Scale bars 10 µm.

Further scattering profiles caused by light propagation through the outer part of the retina are shown in Figure 4.9. As in the inner part, the plexiform layer (outer plexiform layer) showed a marked increase of the scattered light intensity. However, in this second synaptic layer only slightly more light was scattered in position 1 without a Müller cell than in position 2 with a Müller cell in the light path (Figure 4.9 a). Finally, the following relatively thick outer nuclear layer, formed by somata of photoreceptor neurons, once again confirmed the observed effect that nuclear layers evoke less light scattering than plexiform layers (Figure 4.9 b). Again no obvious difference of the scattered light intensity between both positions was recorded. Also, nearly no sideward scattering was observed for the light-sensitive segments of the photoreceptor cells at the end of the retinal light path (Figure 4.9 c) as expected for a light guiding structure (see section 2.2.3). The blue and red curves are superimposed and in both cases no considerable peak in the scattering intensity became visible.

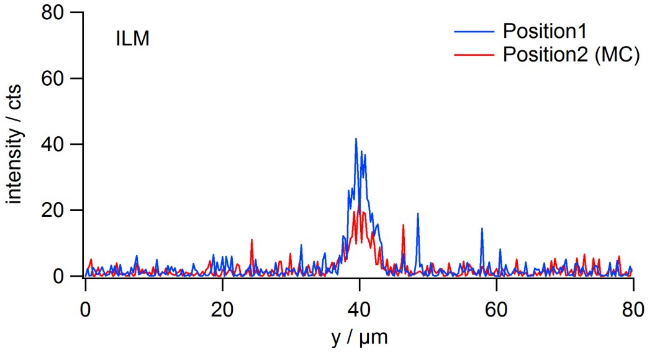

Figure 4.7: Light scattering at the vitread surface. The scattering of light at the vitread surface is illustrated by an intensity profile across 25 pixels (corresponding to approximately 7 µm) around a line along the retinal surface (ILM, inner limiting membrane), shown in Figure 4.6. In a position where the fiber core is placed in front of the endfoot center of the Müller cell (red curve) the light reflection is reduced to a position without a Müller cell in the light path (blue curve).

In contrast to the relatively low scattering within the retina, a huge amount of light interacted with the membrane behind the retina (Figure 4.10). Moreover, the intensity profiles at the membrane was also dependent on the presence of Müller cells within the tissue. If a Müller cell was located in a line with the core of the light emitting fiber, the density of the scattered light at the membrane was increased in comparison to a position without a Müller cell. Obviously, also the curve progression changed from a profile with a single peak in its center to a curve with several maxima distributed over a wider range.

Altogether, the diagrams allow several conclusions about the behavior of light within a vital tissue. At first, the described observations confirm the correlation between the size of the particles and the scattering of light for a vital retinal tissue (see sections 2.1.3 and 2.1.4). In particular, small sized particles and structures with dimensions close to the wavelength of the visible light such as synapses and dendrites are in an appropriate range to evoke extensive light scattering. In accordance with this phenomenon, larger structures as the somata of the retinal neurons in the nuclear layers (between 4 - 10 µm) cause less scattering of light. By comparing the profiles for the inner and outer retinal parts, it can be seen that with an increasing distance to the fiber core the light tends to be distributed over a wider area (Figures 4.8 and 4.9). For interpreting this observation, it is important to

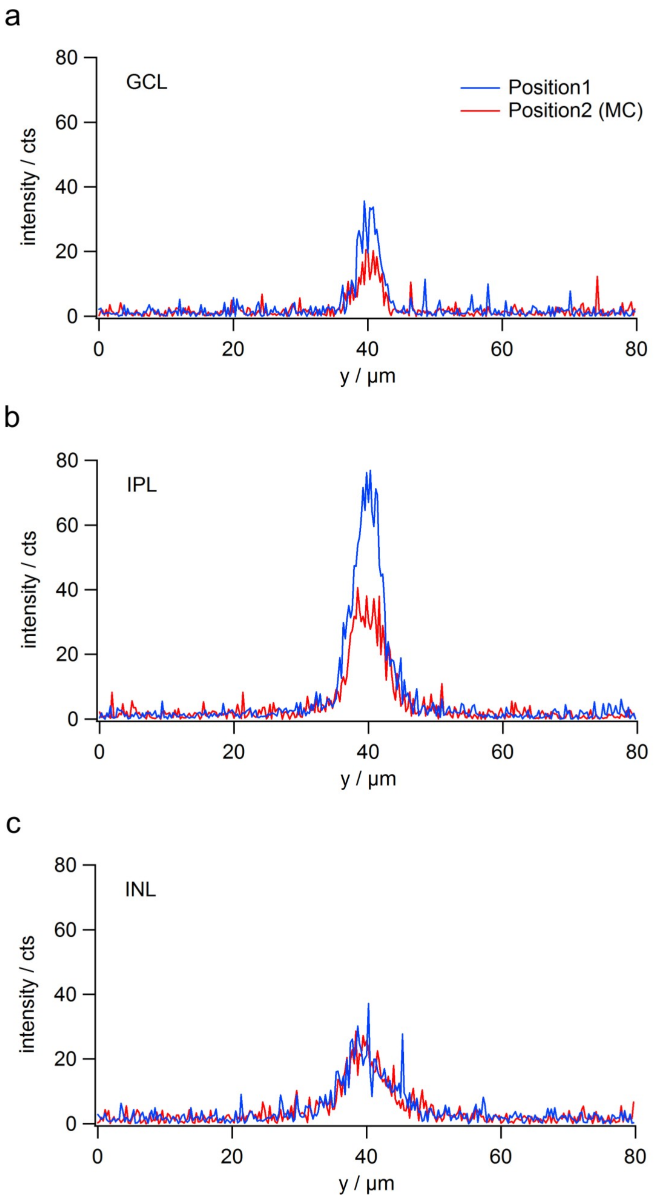

Figure 4.8: Light scattering within the inner part of the retina. (a-c) The scattered light intensity for all parts of the inner retina is studied by intensity profiles across 25 pixels (corresponding to approximately 7 µm) around the lines shown in Figure 4.6. In each part the intensity caused by a fiber position without a Müller cell (blue curves) is compared to a situation where the fiber is placed in front of the Müller cell axis (red curves). (b) In particular, strong scattering occurs in the inner plexiform layer (IPL) which is tremendously reduced if a Müller cell is placed in the path of light. (a, c) In the two nuclear cell layers (GCL, ganglion cell layer; INL, inner nuclear layer) light is less scattered, also the difference between the two positions is lower or even disappears.

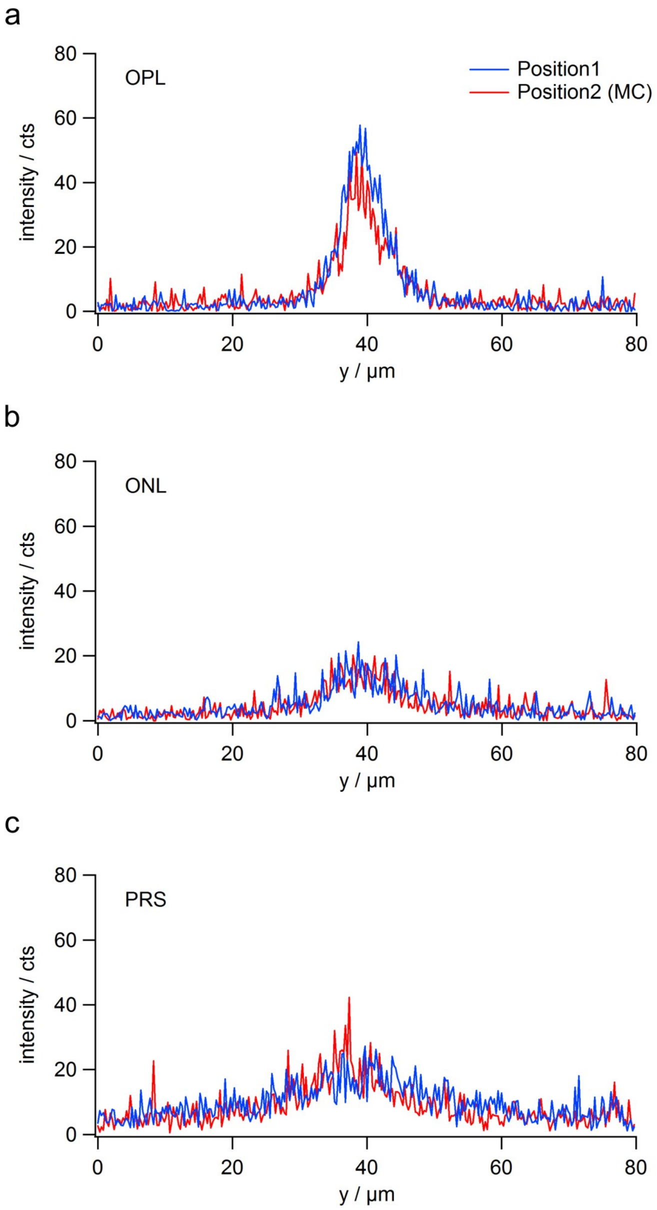

Figure 4.9: Light scattering within the outer part of the retina. (a-c) The scattered light intensity for all parts of the outer retina is studied by intensity profiles across 25 pixels (corresponding to approximately 7 µm) around the lines, shown in Figure 4.6. In each part the intensity caused by a fiber position without a Müller cell (blue curves) is compared to a situation where the fiber is placed in front of the Müller cell axis (red curves). (b) As observed in Figure 4.8, the plexiform layer (OPL, outer plexiform layer) again causes strong laser scattering which is slightly reduced by the Müller cell. (a, c) In the outer nuclear layer (ONL) and the layer of photoreceptor segments (PRS) a low amount of light is scattered into the objective for position 1 and 2.

keep in mind that only light which was hindered in its original propagation was detected by the experimental setup. Consequently, the widening of the profiles were caused by collisions of the divergent laser beam with numerous cellular structures in the light path, so that the beam cone became visible (compare Figure 3.11). In line with this, the amount of light passing the retina without any disturbances will not be collected by the microscope. For example, photoreceptor segments act as wave guides (see section 2.2.3). Thus, images taken perpendicular to their length show low scattering signals (Figure 4.9 c). Müller cells are oriented in the same way as photoreceptor segments and show a similar optic behavior since they reduce the scattering of light which predominantly occurs in the inner plexiform layer. This leads to the assumption that Müller cells, whose light guiding properties were already shown on isolated cells (Franze et al., 2007), also act as light fibers within the vital retinal tissue.

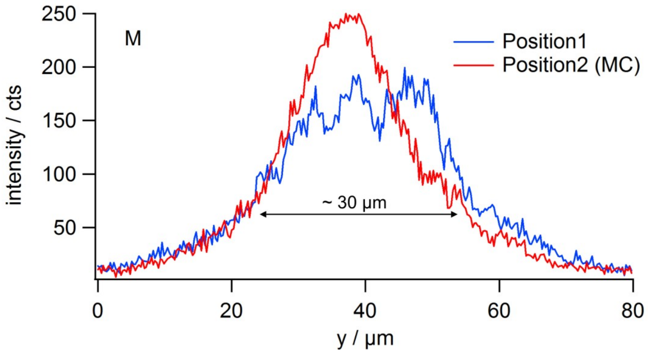

Figure 4.10: Light transmission at the membrane. The scattering of light at the membrane represents the light transmission through the retina which is studied by an intensity profile across 25 pixels (corresponding to approximately 7 µm) around a line along the membrane, shown in Figure 4.6. In a position where Müller cell and fiber core are misaligned (blue curve), the intensity is almost uniformly spread over a range of about 30 µm. This dimension corresponds to the beam diameter estimated by a fiber-membrane distance of about 200 µm and a divergence angle of around 4 - 5°. A Müller cell between fiber and membrane enhances the local light transmission through the retina, whereas all intensity values are distributed around a maximum peak in the center of the profile (red curve).

The Müller cell-dependent projection of light at the membrane supports this theory (Figure 4.10). Consistent with the previous explanation, the dimension of a light projection at the membrane depends on the initial divergence of the light beam and its distance to the fiber tip. The larger the distance the more light is spread, i.e. the more light is uniformly distributed over a wide area (Figure 4.11 a). A light guiding structure in the light path confines the beam to the diameter of the wave guide and a narrow intensity profile appears at the screen behind the retina (Figure 4.11 b, grey). However, a perfect single-peaked curve progression will only be achieved for optimal conditions. Technically, coupling light from one fiber to another, i.e. from the single mode fiber to the Müller cell, is a very sensitive process and strongly depends on lateral and angular misalignments between both elements (Thiel and Hawk, 1976; Murakami et al., 1979; Taylor and Anderson, 1995). Also mismatches of the core diameter influence the guidance of light (Thiel and Hawk, 1976). Considering all these possible artefacts, the projected light spot at the membrane represents an overlay of two portions of light. One portion reached the membrane through the light guiding glial cell (Figure 4.11 b, grey) while the other non-guided part was scattered through the retinal tissue (Figure 4.11 b, blue) and caused a smearing of the transmitted light spot (Figure 4.11 b, red). Indeed, the observed intensity profiles of Figure 4.10 correspond to the described hypothesis illustrated in Figure 4.11 (b). The range over which the intensity was uniformly distributed, without a Müller cell in the light path, was around 30 µm (Figure 4.10, position 1). This was consistent with the beam diameter resulting from a fiber-membrane distance of approximately 200 µm and a light divergence of about 4 - 5°. In particular, it should be noted that the intensity profile for a position with a Müller cell in front of the fiber still shows a wide distribution of light, but with a single peak in its center (Figure 4.10, position 2). This shape corresponds to the assumed profile for a light guiding Müller cell embedded in its natural environment (Figure 4.11 b, red curve). In order to prove this hypothesis, further analysis of the light interactions within the inner plexiform layer and at the membrane, are required as there the largest light modifications occur.

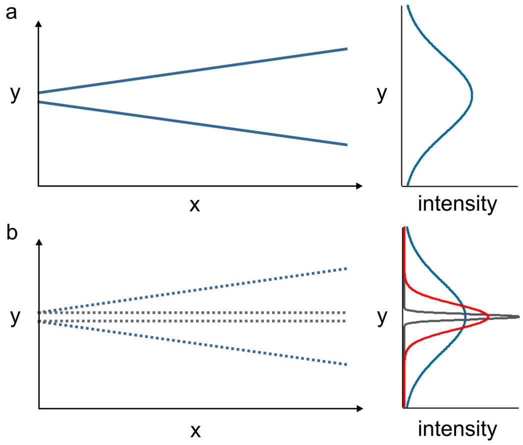

Figure 4.11: Intensity distribution in dependence on the beam path. (a) A divergent beam propagating through a scattering medium (left, blue) leads to a broad intensity distribution behind the medium (right, blue). Changes in divergence depend on interactions within the material. (b) A light guiding structure (parallel dashed lines) prevents the light from diverging and causes a narrow beam profile (grey). Light which is not coupled into the fiber follows its initial spreading and is overlayed with the guided light. The resulting profile (red) shows a wide distribution with a distinct maximum.

4.4 Analysis of the Beam Structure with Respect to Müller Cells

To verify the observed results, the beam structure was examined in detail. As described, the beam pattern was mainly influenced by Müller cells which are supposed to function as wave guides within the retinal tissue. In general, a wave guide is characterized by its low loss light transfer that can be assessed by the scattering in sideward direction along its length and the transmission of light at the output of the fiber. Such kind of mechanism in the retina is primarily required for the plexiform layers to circumvent the intensive sideward scattering arising from interactions of light with numerous synaptic structures (Figures 4.1 and 4.4). Indeed, the propagation of light through the inner plexiform layer strongly depends on the presence of Müller cell processes which can be easily visualized by their intense red fluorescence (Figures 4.6 and 4.8). This clear localization of Müller cells and the distinct thickness of the inner plexiform layer facilitated the detection of any occurring light interaction along the thick tubular processes. In comparison, the short Müller cell processes in the outer plexiform layer get tapered towards the following nuclear layer (Uckermann et al., 2004a) and show a rather low fluorescence. An additional advantage of the inner part of the retina was its short distance to the fiber tip since an increasing distance raises the probability of misalignments. Finally, the inner plexiform layer provided an appropriate basis to investigate the Müller cell-dependent light propagation within the retina.

For this purpose, the laser scattering in the inner plexiform layer was examined by an intensity profile along a line perpendicular to the propagation of light as demonstrated in section 4.3 (Figure 4.12, b and c, red curves; Agte et al., 2011). The resulting curves could be approximated by a Gaussian fit function (Figure 4.12, b and c, black curves)

$$I(y) = I_0 + A \exp\left[-\frac{1}{2}\left(\frac{y - y_0}{width}\right)^2\right] \tag{4.1}$$

where the coefficient A represents the amplitude, I_0 the background intensity and the *width* the spread of the Gaussian curve which center is localized at y_0, the y-position of the fiber core. In my analysis, the intensity distributed in y-direction $I(y)$ was analyzed by these fit parameters to characterize the light propagation within the inner plexifom layer. A first comparison clearly demonstrated that the coefficient values for a position with and without a Müller cell in the light path predominantly differ in their amplitudes A (Figure 4.12, b and c) which was used as parameter for the intraretinal light scatter.

Another insight in the retinal light propagation was provided by the scattered spot at the membrane that imaged the amount of light which was not detected in the inner plexiform layer but penetrated the tissue and reached the membrane as transmitted light (Agte

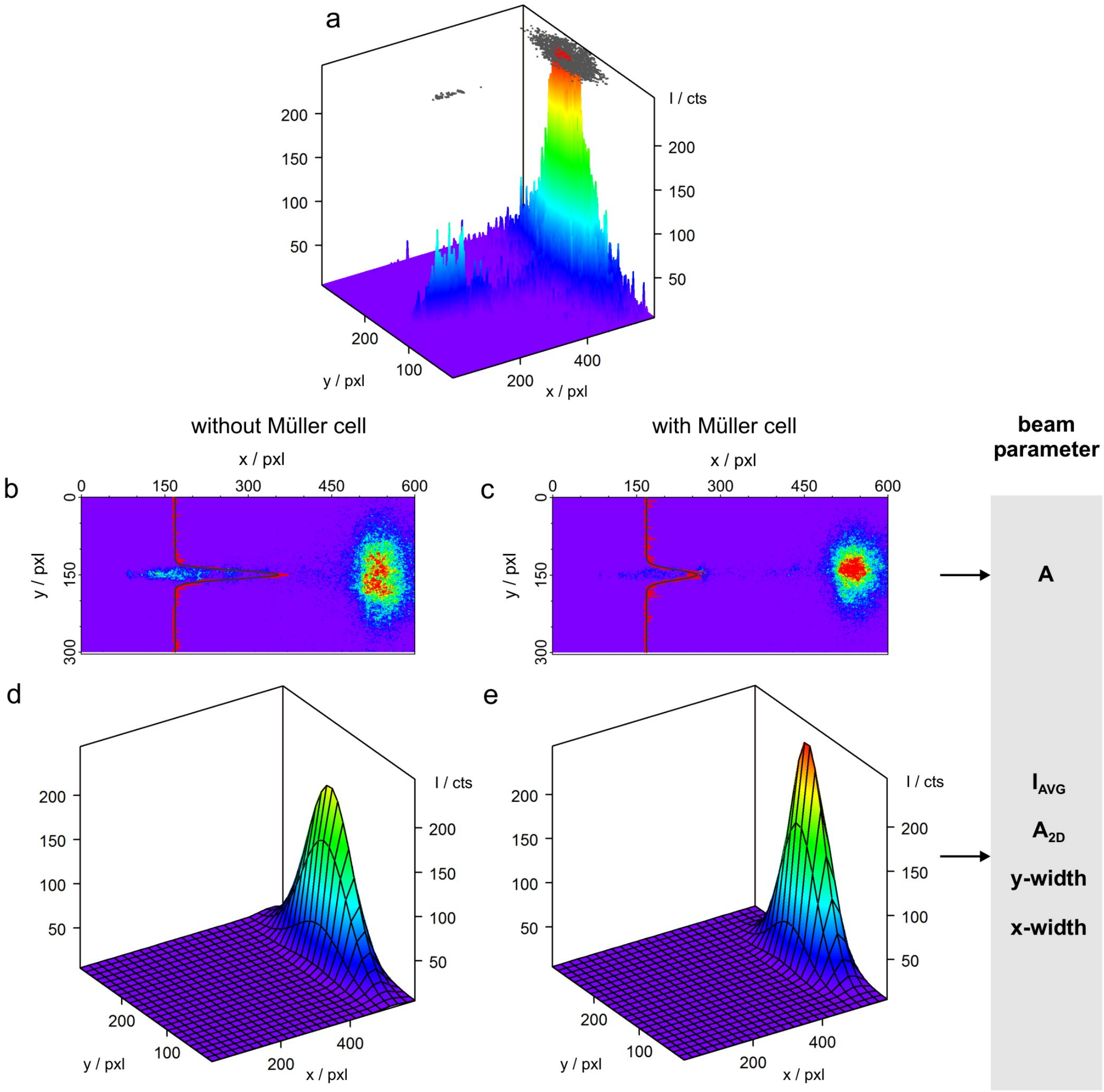

Figure 4.12: Description of the beam structure. (a) Intensity distribution of the scattered light within the sample plotted in three dimensions. A contour plot (grey) displays the two-dimensional projection of the light pattern. (b, c) Interactions of light inside the retina are analyzed by an intensity profile (red) along the inner plexiform layer. A Gaussian function (black) is fitted to the curve to characterize the light structure. In particular, the amplitude A which is used as parameter for the intraretinal light scattering changes in dependence on the presence of Müller cells. (d, e) The light transmission through the retina is estimated by averaging all intensity values across the membrane (I_{AVG}). The shape and distribution of the spot is approximated by a two-dimensional Gaussian (rainbow colored) where the resulting amplitude A_{2D}, the *x-width* and the *y-width* serve as parameters for the distribution of the transmitted light.

et al., 2011). Thus, the intensity was averaged (I_{AVG}) across all pixels at the membrane. However, the transmitted light pattern also changed its shape and density in dependence on the fiber position with respect to Müller cells (Figures 4.5 and 4.10). To characterize the distribution of light behind the retina, the spot was analyzed by a two-dimensional Gaussian fit function

$$I(y) = I_0 + A_{\mathrm{2D}} \exp\left[-\frac{1}{2}\left(\frac{(x-x_0)^2}{x\text{-}width^2} + \frac{(y-y_0)^2}{y\text{-}width^2}\right)\right] \tag{4.2}$$

with A_{2D} as amplitude, I_0 as background intensity and *x-width* and *y-width* as Gaussian widths in x and y-direction, respectively. The position of the peak is given by x_0 and y_0, equivalent to the one-dimensional case. The two-dimensional Gaussians with and without a Müller cell in front of the fiber light are shown in Figure 4.12 (d) and (e).

During a stepwise motion of the retina perpendicular to the fiber axis, the beam parameters were analyzed for each image of the light structure caused by different positions between light source and sample (compare Figure 4.5). In the following, the beam parameters of an image sequence resulting from a micrometer movement over a range of approximately 110 µm will be presented.

In order to investigate changes of the beam parameters with respect to Müller cells, the inner stem processes of the cells were also visualized by an intensity profile of the cellular fluorescence along a line through the inner plexiform layer (plotted in red in Figure 4.13 b; Agte et al., 2011). In Figure 4.13 (a), six fluorescence peaks (1, 2, 4, 6, 7, 8) are visible indicating the stem processes of six Müller cells. Two Müller cell processes were located slightly out of the focal plane but still caused sufficient fluorescence for a clear identification (Figure 4.13 a, 3 and 5). In addition, six regions of low fluorescence represent the interjacent retinal tissue devoid of Müller cell processes (Figure 4.13 a, 1' - 6').

The amplitude A for each retina position along the fiber (110 µm, stepsize 2 µm) is plotted into the same diagram (Figure 4.13 a, black curve). It shows a strong fluctuation of 30.95 % around the amplitude's mean value (A = 80.75 ± 24.99 cts, mean ± SD, N = 55) in dependence on the localization of Müller cells. In particular, the lowest values of A coincide with the largest Müller cell peaks (1, 4, 7, 8) while the two small fluorescent peaks rather show a weak reduction of A or even an increase (peak 5 and 3 respectively). Large amplitudes can be found in the areas between the Müller cells. Therefore, the diagram roughly confirms an inverse correlation between A and the corresponding fluorescence values; a quantitative evaluation resulted in a correlation coefficient r = -0.35. This rather imperfect correlation was substantially improved to r = -0.79 by investigating only the fluorescence values with a clear classification, either as Müller cell or as surrounding tissue between two Müller cells (Figure 4.13 c). Most likely, this effect is caused by the three-dimensional structure of the retinal tissue. The coupling of light from one fiber to another - in this case, from the fiber core to the inner Müller cell stem process - strongly depends on the alignment between both elements (Taylor and Anderson, 1995). Here, the level of the fluorescence intensity can be used to estimate the alignment between Müller cell and fiber core and thus the coupling efficiency. High cell fluorescence indicates that Müller cell processes are positioned in the z-focus of the objective and are thus in the same focal plane as the fiber core. Accordingly, the higher the fluorescence intensity the higher the chance of an efficient coupling of light into the cell body. If more light is trapped within the Müller cell process, less light leaves the cell in sideward direction which reduces the intraretinal light scatter, i.e. the parameter A, caused by the surrounding neuronal tissue.

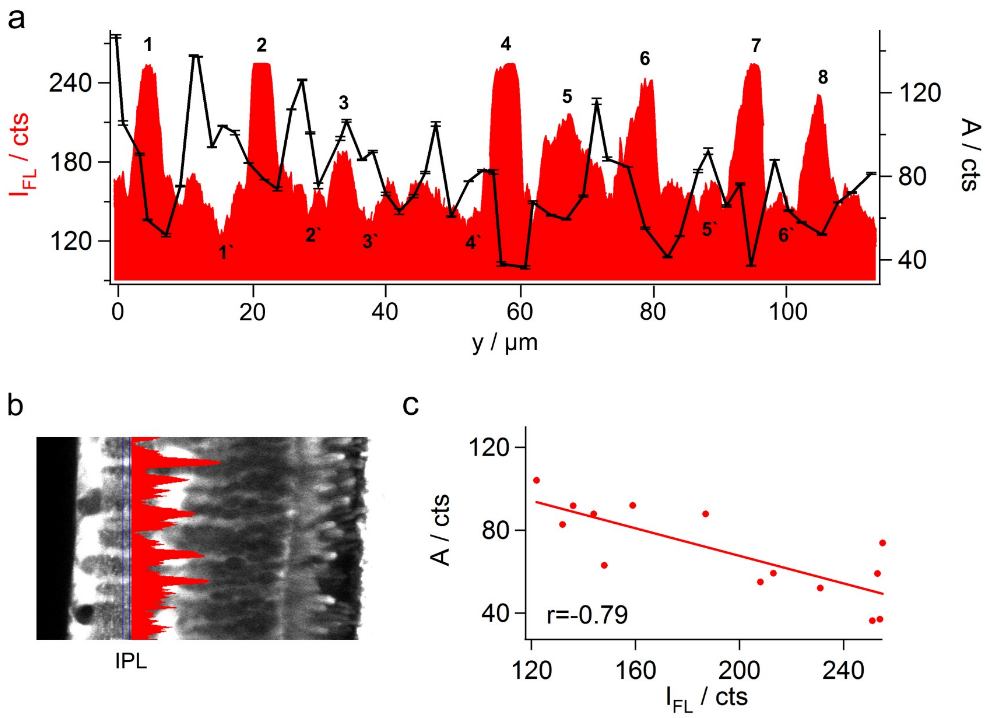

Figure 4.13: Correlation between intraretinal scattering and Müller cells. (a, b) An intensity profile of the fluorescence I_{FL} along the inner plexiform layer (IPL) is used to localize the y-position and, indirectly, the z-position of the Müller cell processes in the retina (red). The intensity maxima 1 - 8 (red) each identify a single Müller cell in the focal plane of the objective in which the fiber core is placed. Spots of low fluorescence (1' - 6') represent the tissue surrounding the thick cell processes. All other data points in the fluorescence profile cannot clearly assigned to one of the two cases. The intraretinal light scatter, described by the amplitude A (black curve in panel a) of a gauss fit of the scattered light in the IPL, behaves contrary to I_{FL}. The parameter A drops down at the fluorescence peaks (1 - 8) and increases towards at the fluorescence minima (1' - 6'). (c) The amplitude A of the well-defined maxima and minima is plotted against the corresponding fluorescence values. The resulting curve shows an inverse correlation with a correlation coefficient of r = -0.79.

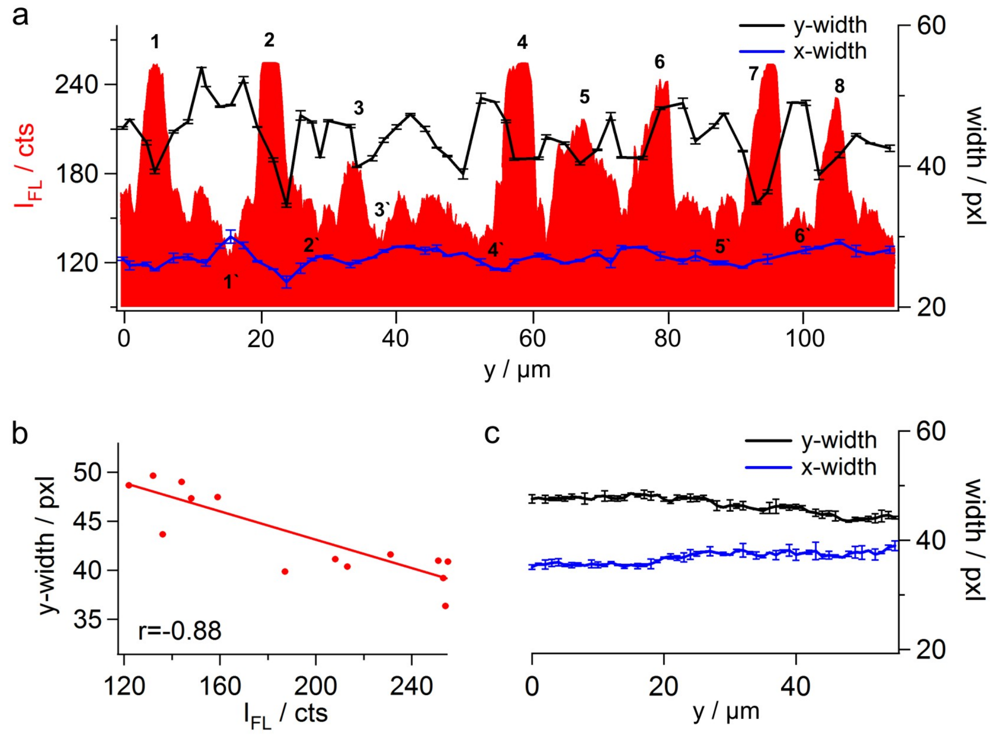

Figure 4.14: Correlation between beam divergence and Müller cells. (a) Intensity profile of the fluorescence I_{FL} along the inner plexiform layer (compare Figure 4.13 a) together with the *x-width* (blue curve) and *y-width* (black curve) of the scattered spot on the membrane for a stepwise change of the fiber position (110 µm, stepsize 2 µm). Both widths, determined by a two-dimensional gauss fit, are used to estimate the light distribution behind the retina. In contrast to the *x-width* the *y-width* fluctuates. These fluctuations depend on I_{FL}, if a high fluorescent Müller cell is present, the *y-width*, i.e. the beam divergence, decreases. (b) The *y-width* of the well-defined maxima and minima is plotted against the corresponding fluorescence values. The correlation results in a correlation coefficient of r = -0.88. (c) Control experiment without the retina attached to the membrane. The *x-width* and *y-width* show a similar behavior as the *x-width* in panel (a).

To prove this light guidance theory in a second manner, I additionally analyzed the distribution of light behind the retina and its behavior with respect to Müller glial cells (Agte et al., 2011). Figure 4.14 (a) shows the same fluorescence profile as Figure 4.13 together with the *x-width* and *y-width* of the transmitted spot for each retina position along the fiber (*x-width*, blue curve; *y-width*, black curve). For each data point the *x-width* is lower than the *y-width*, a result of the used light source. The laser beam emanating from the core of the fiber was divergent, consequently, the y-dimension of the beam increased with the distance between membrane and fiber core. Thus, the transmitted spot on the membrane was used to estimate the divergence of light within the retina by taking its *y-width* as measure of the beam waist. As demonstrated in the diagram, the *y-width* underlies distinct fluctuations of 9.32 % around its mean value (*y-width* = 44.30 ± 4.13 cts, mean ± SD, $N = 55$) while the *x-width* stays nearly constant (*x-width* = 27.40 ± 1.18 cts, mean ± SD, $N = 55$). Comparing these changes of the y-values with the fluorescence intensity, the *y-width* behaves in the same way as the amplitude A, it drops down for the prominent Müller cell peaks and returns to higher values in areas of lower fluorescences. The correlation of all *y-width* values and their corresponding fluorescence intensities resulted in a correlation coefficient of $r = -0.47$, using only the well-defined data points (Müller cells: 1 - 8, regions between Müller cells: 1' - 6') this coefficient could be optimized to $r = -0.88$ (Figure 4.14 b). As shown in Figure 4.14 (c), a control experiment of the membrane spot without the retina in the light path demonstrates an almost constant behavior of the *y-width* with a fluctuation of only 3.24 % around its mean value (*y-width* = 46.48 ± 1.51 cts, mean ± SD, $N = 56$) which is comparable with the *x-width* fluctuation of 2.90 % (*x-width* = 36.87 ± 1.08 cts, mean ± SD, $N = 56$). It was not possible to compare the absolute values of the parameters between control and retina measurement because the experimental settings slightly changed from one experiment to another. Taken together, changes of the beam divergence were only observed with Müller cells in the pathway of light.

Furthermore, the light transmission was investigated regarding its intensity I_{T} (Figure 4.15). Thereby, the averaged intensity I_{AVG} of the transmitted spot and the intensity maximum A_{2D}, determined by the two-dimensional gauss fit, are plotted in the same diagram as in Figure 4.13 and 4.14. The averaged intensity I_{AVG} (blue curve) representing the total retinal light transmission remains unaffected by the different fiber positions in front of the retina ($I_{\mathrm{AVG}} = 84.50 \pm 3.80$ cts, mean ± SD, $N = 55$). In contrast, the maximum intensity A_{2D} (black curve), i.e. the local light transmission in the center of the spot, shows distinct oscillations of 11.79 % around its mean value ($A_{\mathrm{2D}} = 222.11 \pm 26.18$ cts, mean ± SD, $N = 55$). These changes of A_{2D} occur in dependence on the fluorescence intensity, A_{2D} particularly increases for the large Müller cell peaks (2, 4, 5, 7, 8) and drops down for certain points of low fluorescences (1', 4', 5', 6'). The correlation coefficient between all values of A_{2D} and the corresponding cellular fluorescences I_{FL} revealed a value of $r = 0.35$. This value was improved to $r = 0.77$ by only considering the fluorescence values with a clear classification (Figure 4.15 b). In a control experiment without the retina, A_{2D} shows less fluctuations of only 1.57 % ($A_{\mathrm{2D}} = 248.73 \pm 3.91$ cts, mean ± SD, $N = 56$) which is comparable to I_{AVG} with 1.73 % ($I_{\mathrm{AVG}} = 195.76 \pm 3.38$ cts, mean ± SD, $N = 56$). Again, it was not possible to compare the absolute values of the parameters in panel (a) and (c). This observation confirms that changes in the intensity of the transmitted light only occur in the center of the spot in dependence on an intraretinal mechanism allowing a loss-free passage of light through the tissue.

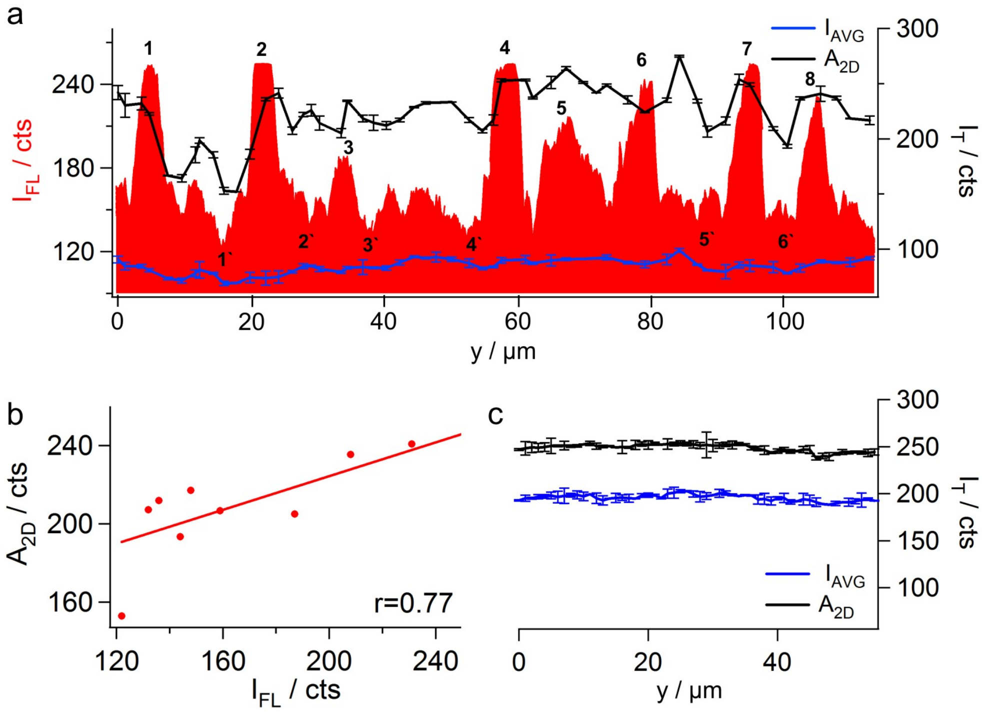

Figure 4.15: Correlation between the transmitted light intensity and Müller cells. (a) Intensity profile of the fluorescence I_{FL} along the inner plexiform layer (compare Figure 4.13 a) together with the averaged intensity of the transmitted spot I_{AVG} (blue curve) and the amplitude of the two-dimensional gauss fit A_{2D} (black curve). During a stepwise change of the fiber position (110 µm, stepsize 2 µm), the total retinal light transmission, described by I_{AVG}, is nearly constant in each data point. The local light transmission through the retina, represented by A_{2D}, fluctuates in dependence on I_{FL}. At the fluorescence peaks (1 - 8), A_{2D} is increased in contrast to the fluorescence minima (1' - 6') at which A_{2D} is low. (b) The amplitude A_{2D} of the maxima and minima is plotted against the corresponding fluorescence values, the correlation coefficient is $r = 0.77$. (c) In a control experiment without the retina, A_{2D} and I_{AVG} show low fluctuations similar to I_{AVG} in panel (a).

To verify this retinal light transport, A_{2D} was compared with the amount of light that was scattered within the retinal tissue, i.e. parameter A. In Figure 4.16 (a), all data points of A_{2D} which were previously assigned to either a Müller cell (1 - 8) or the tissue between (1' - 6') are plotted against A. The resulting correlation coefficient was r = -0.85. In other words, the more light is scattered inside the retina, the lower the maximum intensity of the spot. Conversely, a Müller cell reduces the intraretinal scattering and increases the maximum intensity of the spot center. This result is consistent with the assumption of a light guiding mechanism of Müller cells, as claimed in Figure 4.11. Accordingly, the cell body traps the light and prevents it from diverging. Figure 4.16 (b) shows the beam divergence of the transmitted light (*y-width*) plotted against the intraretinal light scatter A. A data correlation resulted in a positive correlation coefficient of $r = 0.68$ which additionally supports the hypothesis.

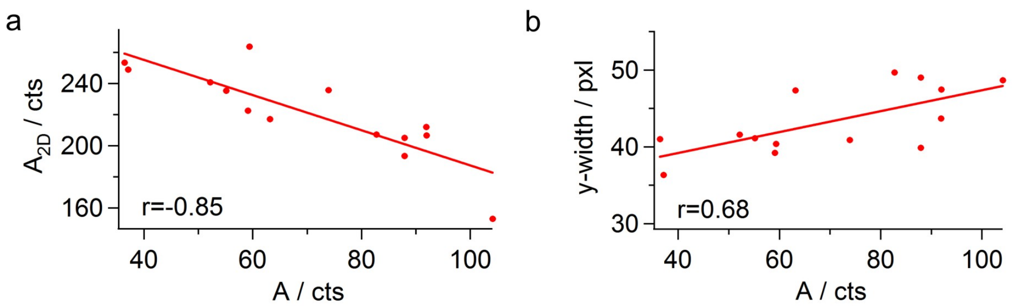

Figure 4.16: Correlation between the intraretinal light scatter and the retinal light transmission. (a, b) The maximum intensity A_{2D} and the beam diameter *y-width* of the transmitted light are plotted against the amplitude A of the light scattering within the retina. The resulting correlation coefficients are r = -0.85 for A_{2D} and r = 0.68 for *y-width*.

4.5 Statistical Relevance of the Data

The analysis of the beam structure within the vital retina described in the previous section was applied to 18 image sequences. During each sequence, the retina was moved about 100 µm whereas around 6 - 10 Müller cells were located one by one in front of the fiber depending on their distribution within the retinal tissue.

However, it was not possible to compare the absolute values of the beam parameters and the Müller cell fluorescence since the experimental settings slightly changed under different conditions. On the one hand, these variations were caused by the preparation of the sample from one experiment to another. For example, a difference in the cutting angle of the retinal slice affected the orientation of the cells and the membrane with respect to the optical fiber. To ensure the vitality of the tissue, I used a freshly dissected guinea pig retina for each individual experiment resulting in a different uptake of the dye for the same staining procedures. In particular, the tissue surrounding the Müller cells varied in its cellular fluorescence which influenced the detection of Müller cells. On the other hand, also mechanical artefacts during the aquisition of a single sequence had to be considered. The y-motion of the stage slightly displaced the sample in x and/or z-direction which in turn changed the x and/or z-distance between retina and fiber core. This, for example, might affect the coupling of light into the cell body. Consequently, the beam structure in the end of an image sequence, especially in long ones, could vary to a small extent with respect to the initial position. For these reasons, only data with less artefacts were taken for my analysis as for example the image sequence shown in section 4.4. Indeed, this allowed the detection of possible differences but the results were not quantifiable. The more strict approach is a mathematically testing of the population mean and its standard error with regard to a confidence level. As precondition, I had to find a method to make all parameters comparable to finally estimate their mean and standard error. Even if only sequences with less artefacts were considered, their effect had to be diminished.

For this purpose, the beam parameters for the well-defined maxima of the fluorescence peaks, as shown in Figure 4.13 (a), were compared with beam parameters of the neighboring fluorescence minima since artefacts between two adjacent situations were negligible.

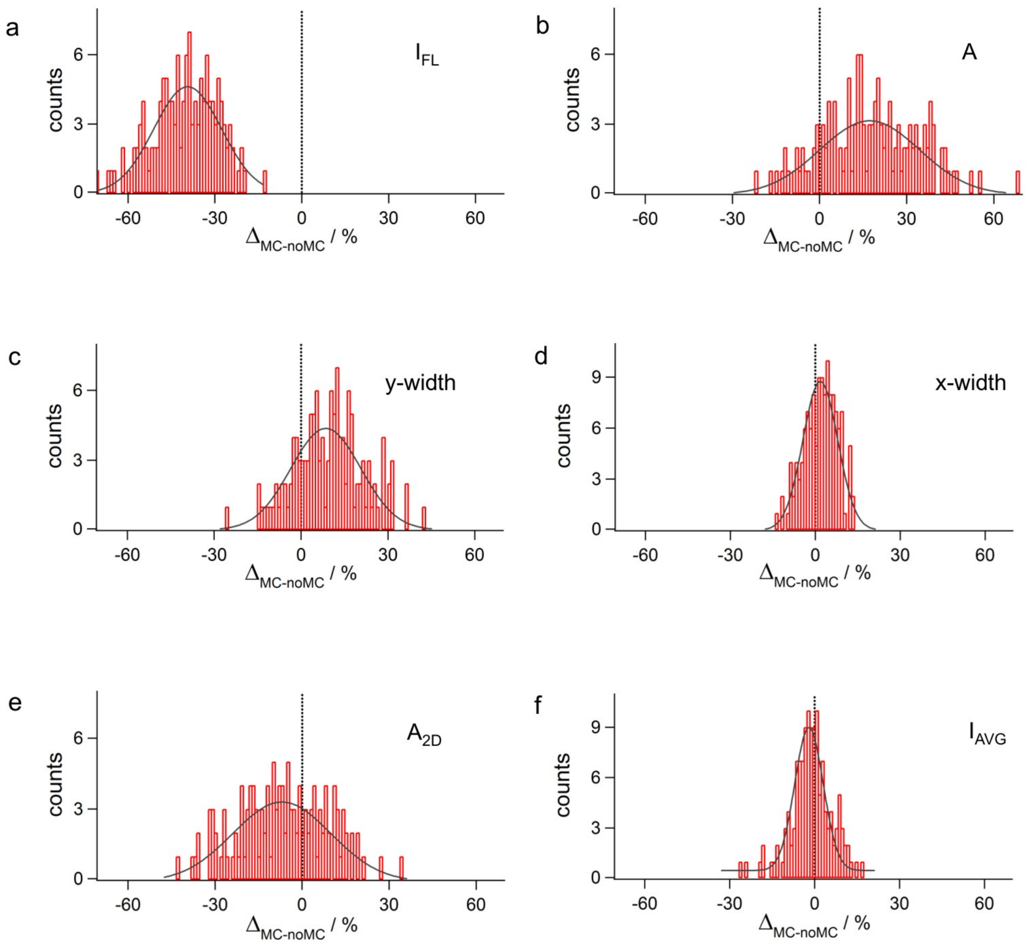

Figure 4.17: Müller cell-dependent changes of the beam parameters. Histograms of the percental changes ($\Delta_{\text{MC-noMC}}$) of the beam parameters from the fluorescence maxima to the adjacent fluorescence minima. The results for $N = 133$ Müller cells are shown. (a) Control measurement to test the software routine. The retinal fluorescence I_{FL} decreases from an area with to an area without a Müller cell. As expected, the percental difference between both situations ($\Delta_{\text{MC-noMC}}$) is shifted to the negative range. (b-f) Also the histograms of the beam parameters are shifted with respect to the zero point (dashed line). All datasets show a normal distribution (Gaussian fit curve, grey).

As explained in the previous section, the fluorescence maxima and minima distinguish regions with a Müller cell from regions without a Müller cell in the light path. In my software routine each beam parameter for a fluorescence maxima was set to 100 % and the percental change $\Delta_{\text{MC-noMC}}$ to the following minima was calculated. The resulting histograms for 133 Müller cells taken from 18 image sequences are shown in Figure 4.17. Gaussian curves fitted to each dataset clearly demonstrate that all data follow a bell-shaped normal distribution which is more or less shifted with respect to the zero line and thus leads to the assumption of a Müller cell-dependent change of the parameters. In order to test the routine, the intensity values for the fluorescence I_{FL} were analyzed in the same way as the beam parameters (Figure 4.17 a). As expected, all values for I_{FL} were found in the negative range since the difference $\Delta_{\text{MC-noMC}}$ between the high Müller cell fluorescence and the low fluorescence of the adjacent area decreased. This confirms that all curves in Figure 4.17 indeed represent changes with respect to Müller cells.

Nevertheless, the data need to be tested statistically as histograms provide no clear evidence of significant differences. Therefore, a one sample t-test was used which calculates the t-value as follows

$$t = \frac{\overline{x} - \mu_0}{SD/\sqrt{N}} \tag{4.3}$$

where $\overline{x}$ is the sample mean, SD the standard deviation and N the sample size (Glaser, 2001). To check the hypothesis that the means of $\Delta_{\text{MC-noMC}}$ did not change with respect to Müller cells, the value μ_0 was set to zero (null hypothesis). The test requires a normal distribution of the datasets. As shown in Figure 4.17, the data were already approximated to a Gaussian by fitting a Gauss curve to all histograms. However, according to the central limit theorem, the test can be also applied to data without a normal distribution if the sample size is sufficiently high (Glaser, 2001). A cell number of $N = 133$ meets this condition and additionally supports the statements of the test that will be described in the following (Figure 4.18).

The intraretinal light scattering represented by the amplitude A and the beam divergence behind the retina represented by *y-width* significantly increased to 17.58 ± 2.01 % (mean ± SEM, $N = 133$) and 6.75 ± 1.68 % (mean ± SEM, $N = 133$), respectively. In contrast, a statistically significant decrease of -6.87 ± 1.95 % (mean ± SEM, $N = 133$) was observed for the amplitude A_{2D} describing the local light transmission through the retina. However, no significant difference between regions with and without a Müller cell was identified for the *x-width* of the membrane spot (1.51 ± 1.08 %, mean ± SEM, $N = 133$) and the total intensity of the transmitted light, represented by the averaged intensity at the membrane I_{AVG} (1.80 ± 0.77 %, mean ± SEM, $N = 133$). These results were consistent with the effects observed in section 4.4 as only A, *y-width* and A_{2D} varied in dependence on the Müller cell fluorescence (compare Figures 4.13, 4.14 and 4.15), no fluctuations occurred for *x-width* and I_{AVG} (compare Figures 4.14 and 4.15).

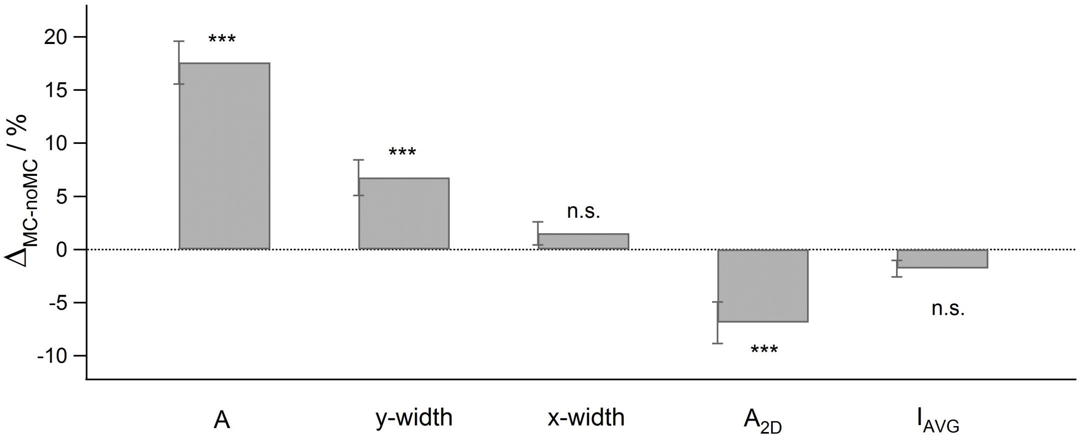

Figure 4.18: Statistic testing of the beam parameters. The percental variations $\Delta_{\text{MC-noMC}}$ of the parameters describing the beam structure are calculated from an area with a Müller cell to an area without a Müller cell in the lightpath. The parameters A (17.58 ± 2.01 %), *y-width* (6.75 ± 1.68 %) and A_{2D} (-6.87 ± 1.95 %) significantly change with a confidence $\geq 99\%$. The *x-width* (1.51 ± 1.08 %) and I_{AVG} (1.80 ± 0.77 % show no significant difference between both situations. Values are means ± SEM. ($N = 133$, *** highly significant $\alpha = 0.01$, n.s.: not significant, a single sample t-test was performed with the software Igor Pro)

The resulting difference $\Delta_{\text{MC-noMC}}$ for A, observed from the inner plexiform layer, exceeds the differences for *y-width* and A_{2D} which were determined at the membrane. For each experiment the inner stem processes of Müller cells in the plexiform layer were aligned with respect to the fiber core. Thus, changes of the scattered light became very clear. However, most of the Müller cells slightly changed their orientation with an increasing distance to the fiber (see Figure 3.4), thus, the transmitted light might be projected slightly out of the focal plane of the objective. This could explain why changes of the light spot became less obvious than differences of the light structure within the inner plexiform layer. Thus, the relative light guiding efficiency

$$\eta_{\mathrm{r}} = \frac{100\ \%}{100\ \% - |\Delta_{\text{MC-noMC}}|}, \tag{4.4}$$

defined as the ratio between the transported light with and without the Müller cell, revealed $\eta_{\mathrm{r}} = 1.21 \pm 0.03$ for the intensity of the intraretinal light scattering in the inner plexiform layer (A) and $\eta_{\mathrm{r}} = 1.07 \pm 0.02$ for the intensity of the local light transmission at the membrane (A_{2D}).

4.6 Coupling Efficiency and Signal-to-Noise Ratio

The described results have shown that the regularly arranged Müller cells within the retina achieve a redistribution of light, presumably to improve the signal-to noise ratio at the level of the photoreceptor cells. This light pattern depends on the distribution and orientation of the tubular Müller cells inside the tissue. In my experiments only straight Müller cells that were aligned along the laser axis were able to project the beam to the same y-position from where it arose (compare Figure 4.19 (a) with Figures 4.13, 4.14 and 4.15: cells numbered 4 and 7). However, in some cases I observed a slight y-displacement between the axis of the fiber core and the maxima and minima of the beam parameters, i.e. the minima of A and *y-width* and the maxima of A_{2D} (see Figures 4.13, 4.14 and 4.15: cells numbered 2 and 6).

If Müller cells act as light fibers, there are two possible explanations for a shift in y-direction (Agte et al., 2011): First, it can be expected that Müller cells without a straight orientation will redirect the light along their curved shape, accordingly, the spot is displaced with respect to the beam axis (Figure 4.19 b). A second explanation can be given by the divergence of the used light source. If the axis of the light cone is not centered in front of the Müller cell, only divergent light rays with an angle to the laser beam axis are guided and cause a spot displacement in y-direction (Figure 4.19 c).

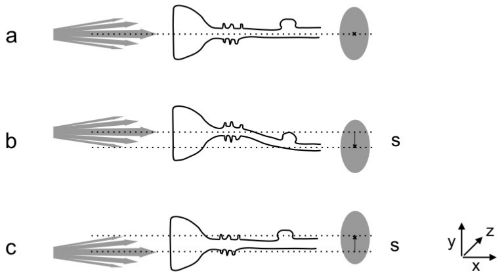

Figure 4.19: Schemata of the light passage through Müller cells. (a) The fiber axis is centered in front of a straight Müller cell. The fiber core, the axis of the Müller cell and the center of the transmitted spot are at the same y-position. (b) A Müller cell with a bended shape guides the light to a y-position which is displaced by a distance s with respect to the fiber core. (c) A displacement s is also generated if the center of the beam cone does not hit the axis of the Müller cell. Only light rays with an angle to the beam axis pass the cell.

This second case was examined in detail to study the coupling of light into a Müller glial cell (Agte et al., 2011). In order to exclude a change of the cell orientation along the entire retinal thickness, an individual Müller cell was chosen whose orientation varied neither in y nor in z-direction as shown in Figure 4.20. The considered Müller cell was moved in micrometer steps perpendicular to the divergent light beam to analyze the expected effects for different coupling conditions which slightly change for each y-position. In Figure 4.20,

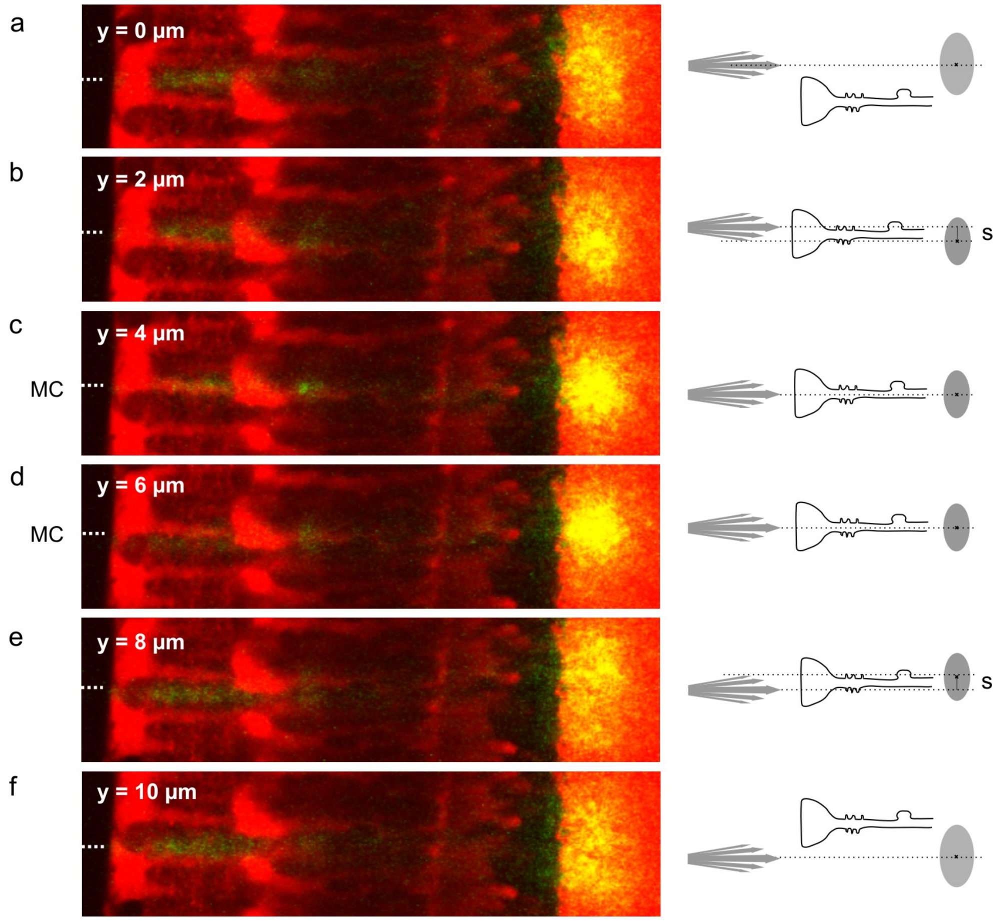

Figure 4.20: Coupling efficiency of a light guiding Müller cell. (a-f) A straight Müller cell whose orientation varies neither in y nor in z-direction is moved perpendicular to the beam cone of the divergent laser light (stepsize 2 µm) in order to study the different coupling conditions into a Müller cell (illustrated in the right schemata). The position of the fiber core is indicated by a white line. (a and f) If the light of the fiber illuminates the neuronal tissue between two Müller cells, prominent light scattering within the retina is caused and a less intense transmitted spot at the membrane appears. (b and e) When the fiber illuminates an endfoot region closer to the cell axis, only light rays with an angle to the beam axis enter the Müller cell. The transmitted spot intensity increases and the spot is displaced in y-direction (b, displacement s below the beam axis; e, displacement s above the beam axis). (c and d) For ideal coupling conditions, indicated by the word MC, the axis of the beam cone and the cell body are aligned. The intensity of the transmitted spot increases and no displacement is observed.

the fiber core is indicated by a white line in front of the retinal surface. The schemata on the right hand side in Figure 4.20 illustrate the different coupling conditions. In a position where the axis of the beam cone and the inner stem process of the Müller cell were not aligned, the light was scattered by the neuronal tissue between the Müller cells and the transmitted spot showed a wide distribution with a low maximum intensity (compare Figure 4.20 (a) with Figure 4.6 (a)). Then, the retina was moved and the laser light emanating the fiber core illuminated an endfoot region which was closer to the center of the cell. Here, one portion of light was still scattered in the retinal tissue while the spot at the membrane became brighter and was slighty shifted against the beam axis (Figure 4.20 b). This observation corresponds to a coupling condition where the laser beam does not hit the central part of the wave guide. Only oblique light rays of the beam cone were coupled into the cell body. In a position where the beam cone was directly positioned in front of the cell, the light scattering in the retinal tissue disappeared and the transmitted light spot became brightest without a displacement in y-direction. Thus, the laser light was efficiently coupled into the cell as expected for ideal coupling conditions between light source and wave guide (Figure 4.20, c and d). A further step in y-direction abolished this perfect alignment, thus the prominent light scattering within the retina rapidly increased and the transmitted spot became less intense. Again, only light rays with an angle to the beam axis passed the cell and caused the expected opposite displacement (Figure 4.20 e). In a position where the beam did not hit the center of the endfoot most of the laser beam bypassed the Müller cell and caused a wide and diffuse light transmission without displacement (Figure 4.20 f).

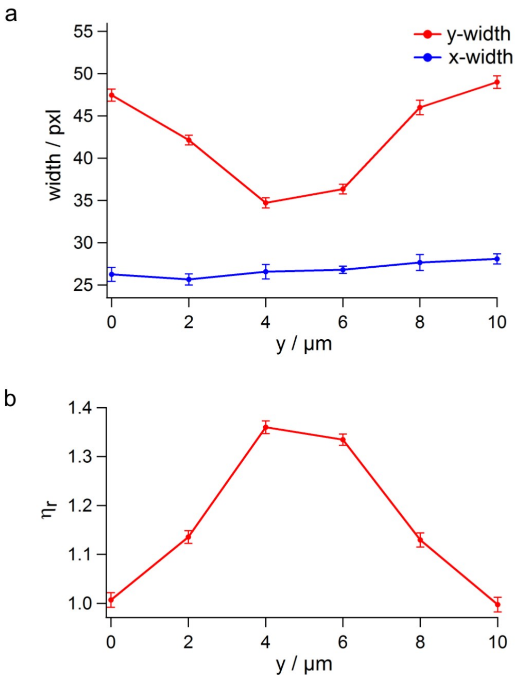

Figure 4.21: Light guiding efficiency for different coupling conditions. Analysis of the transmitted spot shown in Figure 4.20. For ideal coupling conditions the *y-width*, i.e. the beam divergence, is at the lowest value of about 35 pxl (a) and the relative light guiding efficiency η_r reveals a maximum of 1.36 ± 0.01 (b). When only light rays with an angle to the beam axis are guided, η_r drops down to 1.13 ± 0.01. The x-dimension of the transmitted spot (*x-width*) remains unaffected by the retina movement.

Finally, the image sequence was analyzed with the same procedure as introduced in section 4.4. The resulting relative light guiding efficiency η_r, determined by the parameter A, shows a nearly constant maximum of around 1.36 for the two ideal coupling conditions (Figure 4.20, c and d) since the beam was trapped inside the cell and was hindered in its original divergence (Figure 4.21). In other words, 1.36 times more light was guided than without a Müller cell in the beam path (Figure 4.20, a and f). In contrast, if the cell and fiber axis were slightly misaligned, the relative light guiding efficiency revealed a value of only 1.13. This value is in line with a small amount of light coupled into the cell body. These observations additionally demonstrate that Müller cells have light guiding features and act as living light fibers within their natural environment.

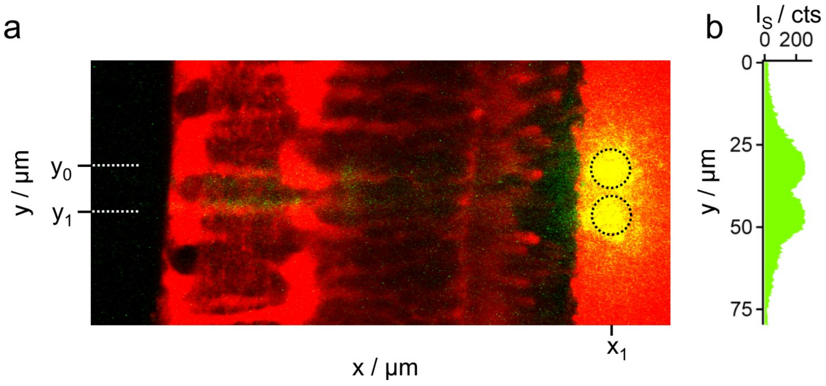

Figure 4.22: Müller cells suppress the beam widening. (a) The fluorescence (red) of two neighboring Müller cells is overlayed with the laser scattering (green) resulting from two fiber positions, y_0 and y_1 (dotted lines). At both positions the fiber core and the axis of the respective Müller cell are co-aligned to achieve similar coupling conditions. At the membrane two transmitted spots (black circles) with minimal overlap appear. (b) The intensity profile of the scattering intensity I_S along a line at x_1 shows two distinct peaks of similar width and maximum intensity.

To further study the light pattern behind the retina, the transmitted intensity of at least two adjacent Müller cells have to be compared. Figure 4.22 (a) shows the same Müller cell as in Figure 4.20 together with its closest neighbor which has a similar fluorescence intensity. Thus, both cell processes were located in the focal plane of the objective, the same z-level where the fiber core was placed before. For this reason, it can be assumed that the coupling conditions and the efficiency of the light guidance were comparable. Finally, the projection areas of the transmitted light resulting from the fiber positions in front of the two adjacent Müller cells were overlayed. At the membrane two transmitted spots with small overlap became visible which were analyzed by an intensity profile along a line at x_1 (Figure 4.22 b). The profile shows two distinct peaks of similar width and maximum intensity (Agte et al., 2011). The distance between the maxima corresponds to the distance between the axes of the Müller cells.

In conclusion, all results obtained from fiber experiments on retinal slice preparations (sections 4.1 - 4.6) have shown that Müller cells efficiently couple the light at the vitread surface, transport it without losses through the entire retinal thickness and finally increase the signal-to-noise ratio behind the retina by their appropriate spatial distribution within the retina. With this in mind, the next section will study if such an improvement of the signal-to-noise ratio really allows a separation of the visual information at the level of the photoreceptor cells.

4.7 Müller Cell-dependent Illumination of Photoreceptor Cells

The obtained results of the optical fiber setup clearly show that vital Müller cells embedded in their natural environment act as wave guides transporting the light through the retinal tissue. Thus, the light pattern behind the retina is interspersed with intensity peaks whose distribution corresponds to the array of Müller cells. Next, this improvement of the signal-to-noise ratio will be studied with respect to photoreceptor cells located at the backside of the retina.

In 1963, Enoch (1963) found that photoreceptor segments are wave guides by themselves, the light is trapped within the elongated structures and is finally absorbed by the sensitive visual pigments at the outermost part of the receptors. As observed for light guiding Müller cells, in wave guides no or less light is scattered sidewards perpendicular to the light propagation which in turn has the effect that no light reaches the objective placed perpendicular to the segments as in the fiber setup. For this purpose, the illumination pattern of photoreceptor cells has to be detected behind the retina. In this way, the light coming from single Müller cells can be assigned to the corresponding rod and cone cells.

To simultaneously image Müller cells and photoreceptors from both surfaces of the vital tissue, I used a setup with two opposing microscope objectives (see section 3.2.3; Agte et al., 2011). The retina was spread onto the bottom of a transparent sample chamber on top of a an inverted confocal microscope which condensor was replaced by a custom-built microscope. The inner retinal surface of the fluorescently stained sample was pointed towards the confocal objective while the outer part was imaged from above by the upright imaging unit. In this experimental arrangement the laser scanning microscope was used to record high resolution images in different depths of the inner retina to provide detailed information about the Müller cell shape, distribution and spatial orientation. Figure 4.23 (a) shows a reconstruction of the confocal z-stack illustrating Müller cell endfeet funneling into their thick inner processes. The dashed white lines demonstrate the z-positions of two intersecting images, shown in Figures 4.23 (b) and (c). The endfeet of Müller cells close to the retinal surface form an almost homogeneous fluorescence (green) only interrupted

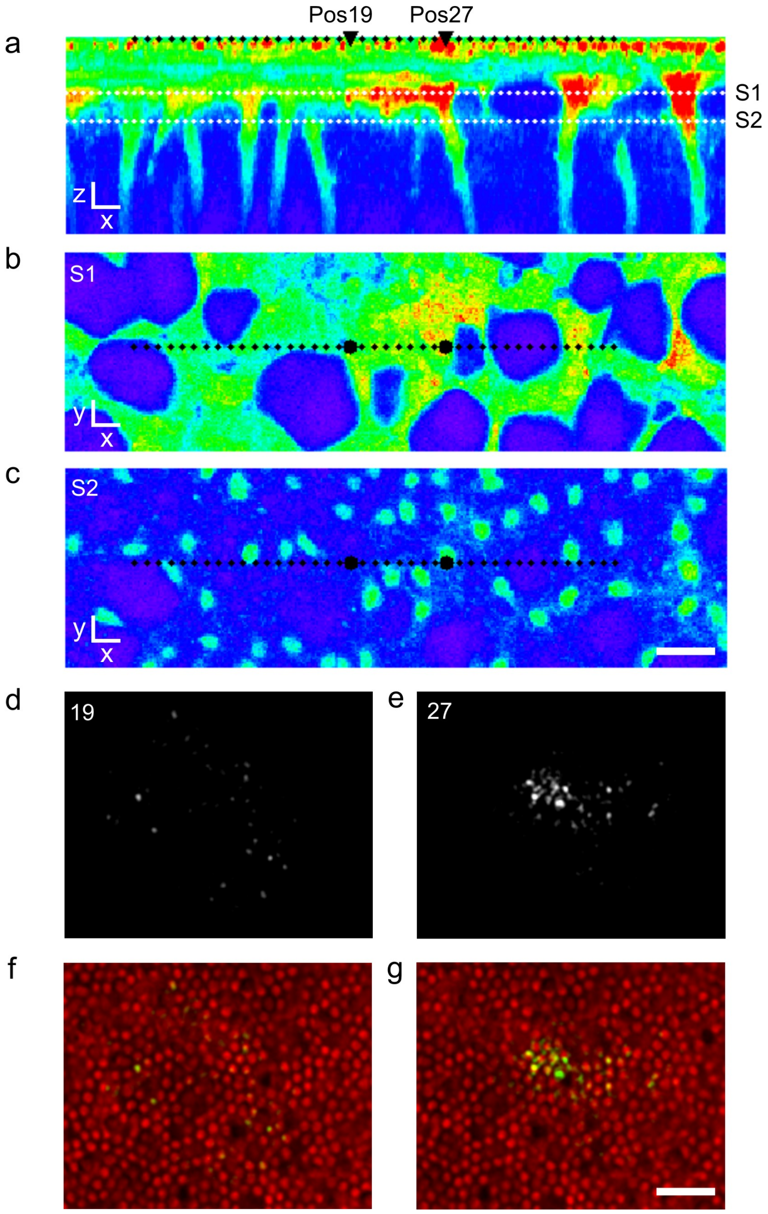

Figure 4.23: Both way imaging of the retina combined with local light-transmission. The fluorescent retina is imaged from both surfaces by two opposing microscopes. (a) A z-reconstruction of an image stack, acquired with a laser scanning microscope from below, shows the endfeet and inner stem processes of the fluorescently stained Müller cells. The image was created by using a maximum intensity projection across seven pixels (corresponding to 2.4 µm) in y-direction around a line indicated in (b) and (c). The black dots represent the positions of the stationary focused laser beam that illuminated the sample. (b, c) Confocal slices (S1, S2) at specific retinal depths (dashed white lines in (a)) are used to position the laser beam with respect to Müller glial cells. (d, e) Transmission images corresponding to a laser focus either positioned in the center of the Müller cell (e, position 27) or in its periphery (d, position 19). (f, g) Overlay of the transmitted light and the photoreceptor cells (red). Scale bars 10 µm.

by non-fluorescent ganglion cell bodies (Figure 4.23 b). With increasing retinal depth the inner stem processes allow a clear separation of individual Müller cells (Figure 4.23 c).

In addition to the imaging of Müller cells within the living tissue, the confocal microscope was also used to illuminate the retina whereas the light arriving at the photoreceptor cells was detected by the opposing objective. For local Müller cell illumination a low-numerical objective was used to focus a laser beam at an angle close to the physiological conditions (see section 3.2.4). Here, the prior acquisition of the cellular fluorescence allowed to precisely position the stationary focused light onto the surface of the retina after localizing Müller cells in the deeper inner plexiform layer (Figure 3.17). The laser light was moved in equal steps of 1 µm, indicated by black dots, each representing a single position of the light source onto the Müller cell endfeet (Figure 4.23 a-c, stepsize 1 µm). Two positions were chosen to demonstrate the Müller cell-dependent behavior of light at the level of the photoreceptor cells (bold black dots). In position 27 the light source was placed in the center of the endfoot so that the light can enter the tubular stem process of the glia cell.

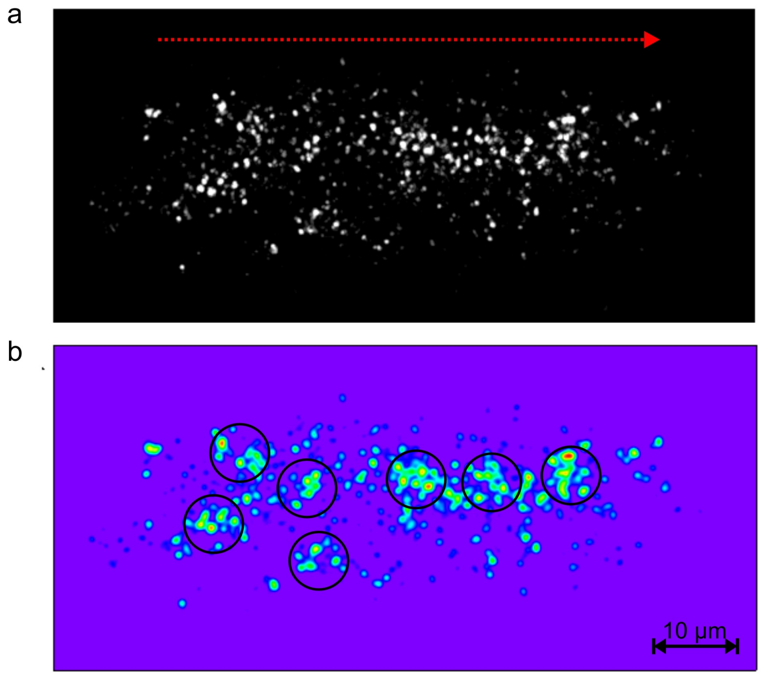

Figure 4.24: Illumination pattern of the photoreceptor cells. (a) Maximum intensity projection of all transmitted light spots originating from a stepwise positioning of the light source at the vitread surface (see Figure 4.23). Unlike the straight movement of the light beam (red arrow) the illuminated photoreceptor cells show a rather non-uniform transmission pattern. (b) After an image filtering, the irregular intensity distribution in (a) become more obvious. The nearest distance between neighboring intensity peaks (black circles) is around 10 µm. Scale bar 10 µm.

As a result, an intense illumination of a small group of photoreceptor cells was observed (Figure 4.23, e and g). For comparison, the light source was placed in the periphery of the endfoot in position 19. The low intense transmitted light was received only by some receptor cells which were randomly spread over a wide area (Figure 4.23, d and f). These observations clearly confirm an influence of the Müller cells on the transretinal propagation of light on its way to the sensitive photoreceptor cells.

Figure 4.24 (a) illustrates a maximum intensity projection of all transmission images resulting from the consecutive laser positions as shown in Figure 4.23. In general, the composed projection follows the direction of the incoming light source. However, the light emerging from the tips of the densely packed photoreceptor segments shows a rather non-uniform distribution. To emphasize the pattern of the intensity map, the raw projection image was smoothed by a median filter (Figure 4.24 b). After this filtering process, distinct intensity peaks (surrounded by black circles) became visible though the peaks were not perfectly positioned along a line. This reflects the distribution of Müller cells within the retina since not all endfeet were directly illuminated in their central part. An additional explanation for such sideward deviations is the intraretinal orientation of Müller cells, with increasing tissue depth most of the cells are slightly shifted with respect to their endfoot center (see Figure 4.23 a).

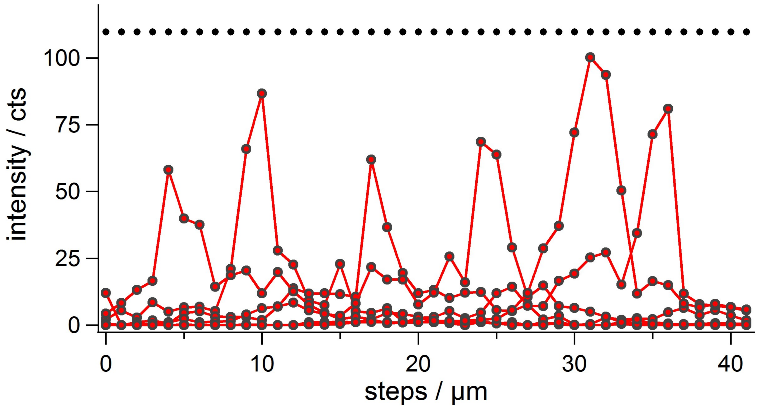

Figure 4.25: Transmitted light intensity received by the photoreceptor cells. Six photoreceptor cells (objective focus on rods) are chosen to represent the transmitted light intensity during a stepwise motion of the light source (single steps are indicated by black dots). All cells are positioned close to an area located under the illumination line. Each curve shows a single peak which does not last longer than 3 steps (stepsize 1 µm).

Subsequently, the light intensity received by the receptor cells was investigated for all positions of the laser beam. Six photoreceptor cells from areas situated in arbitrary distances under the illumination line were chosen for the analysis, the intensity curves are shown in Figure 4.25. Each curve shows a single peak with an intensity that rapidly increases for a certain step and finally returns to the background value after a maximum of 3 steps each of 1 µm (minimum: 1 step). This distance of 1 - 3 µm is in accordance with the averaged diameter of the Müller cell stem process in the inner plexiform layer (Reichenbach and Birkenmeyer, 1984, section 4.8). Finally, this finding supports that the high intensity in the center of the transmitted light spot as obtained in the fiber experiments (sections 4.4 and 4.5), was evoked by light guiding Müller cells.

4.8 Spatial Relation between Müller Cells and Cone Photoreceptors

In order to find a relation between cellular elements participating in retina optics, Müller cells and photoreceptor cells were morphologically analyzed using protocols for fluorescent labeling in combination with confocal microscopy (see sections 3.1.4 and 3.1.6).

For a first estimate, I focused my research on the density and distribution of both cell types within the retinal tissue. The Müller cell distribution and quantitity could be assessed in the inner plexiform layer while individual photoreceptors were identified at the level of their inner segments. To additionally measure the geometrical dimensions of these cellular structures, I used vital staining procedures to maintain their original shape unaffected by preparation artefacts (see section 3.1.3). The photoreceptor dimensions were measured at a focal depth where the cone segments were not tapered. Here, the diameter of the cone cells ($d_{\mathrm{cone}} = 3.05 \pm 0.57$ µm, mean ± SEM, $N = 125$) is slightly larger than the diameter for the rod photoreceptor cells ($d_{\mathrm{rod}} = 2.15 \pm 0.21$ µm, mean ± SEM, $N = 929$) which corresponds to earlier estimates (Reichenbach and Bringmann, 2010;

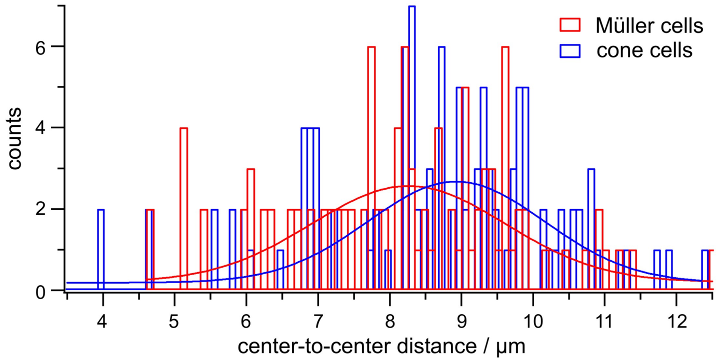

Figure 4.26: Structural comparison of Müller cells and cone cells in the vital retina. The center-to-center distances of neighboring Müller cells (Gaussian fit: $x_{\mathrm{MC}} = 8.26 \pm 0.13$ µm, mean ± SEM, $N = 107$) and neighboring cone photoreceptor cells (Gaussian fit, $x_{\mathrm{cone}} = 8.93 \pm 0.11$ µm, mean ± SEM, $N = 125$) are roughly equal.

Reichenbach et al., 2012). Both segments are definitely larger than the wavelength of the visible light. The diameter of Müller cell processes ($d_{\mathrm{MC}} = 3.32 \pm 0.49$ µm, mean ± SEM, $N = 107$) is close to the diameter of cone segments. However, not only the size but also the distribution of Müller cells appears to be similar to those of cones. The center-to-center distances between both cell types were analyzed and plotted in a diagram shown in Figure 4.26. A Gaussian function fitted to the curves resulted in an averaged distance of $x_{\mathrm{MC}} = 8.26 \pm 0.13$ µm (mean ± SEM, $N = 107$) for Müller cell processes and a similar value of $x_{\mathrm{cone}} = 8.93 \pm 0.11$ µm (mean ± SEM, $N = 125$) for cone photoreceptor segments. As demonstrated in the diagram, the curves do not follow a perfect Gaussian shape which reflects the random distribution of Müller cells and cone receptors that, as biological objects, are not always uniformly spaced. Furthermore, it should be noted that the cell densities slightly vary among the different retinal areas (Reichenbach and Robinson, 1995), thus, the data were collected only from a small peripheral region of the retina. Therefore, the results provide just a first indication of a possible connection between Müller cells and cone receptors.

Driven by these estimates, the spatial relation between Müller cells and cones was investigated in more detail. A cell type specific labeling of Müller cells and cone photoreceptor cells (see section 3.1.6) revealed that in fact both cell types were regularly arranged as pairs at the level of the outer plexiform layer (Figure 4.27; Agte et al., 2011). In this layer the outer processes of Müller cells were loaded by antibodies directed to vimentin, a protein specific to Müller cells, while the synaptic terminals of cones (pedicles) were identified by cone-specific peanut agglutinin.

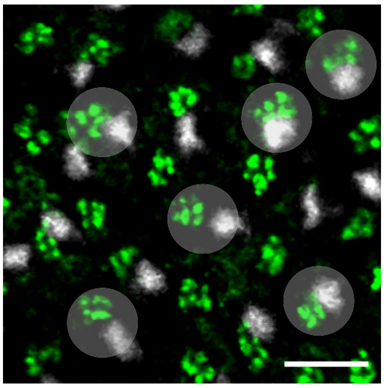

Figure 4.27: Colocalization of Müller cells and cone photoreceptors. Confocal image of a (immuno)-histochemically stained retina at the level of the outer plexiform layer. Müller cells, labeled by antibodies directed to vimentin (grey), and synaptic terminals of cone photoreceptors, labeled by fluorescent peanut agglutinin (green), are arranged as pairs (highlighted circles). Scale bar 10 µm.

Cone pedicles are located relatively far from the light-sensitive photoreceptor segments which the light has to pass to stimulate visual pigments (approximately 20 µm for guinea pig retina). Consequently, only a simultaneous detection of Müller cells and photoreceptor segments offers new approaches for a potential optical coupling. Accordingly, to visualize the orientation of elongated Müller cells together with cone photoreceptor segments within the vital retina, I used a special procedure combining a labeling of the tissue with FM1-43 and a subsequent treatment with another substance to suppress undesired fluorescences (see section 3.1.6). For deep tissue penetration from the retinal surface towards the opposing photoreceptor segment layer, a two-photon laser scanned thin optical sections to reduce disturbances induced by other retinal layers. Finally, a z-stack reconstruction (Figure 4.28) provided virtual slices through the retinal tissue. The membrane-sensitive dye FM1-43 predominantly stained the inner and outer segments of the cones, recognizable by the typical tapered shape of their outer parts. Furthermore, strong fluorescence occurred in the inner synaptic layer with the Müller cell processes as the only non-labeled structures. In fact, in many instances Müller cell processes, represented by long dark tubes, were aligned with the cone segments.

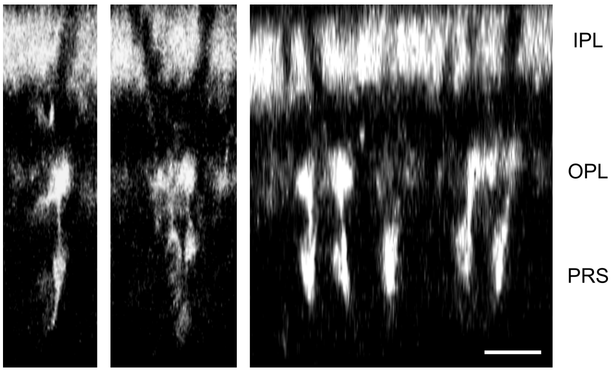

Figure 4.28: Co-alignment of Müller cells and cone photoreceptors. Virtual cross section of the retina generated by two-photon microscopy. The fluorescent dye FM1-43 labels cone photoreceptors in their entire length from the outer plexiform (OPL) to the photoreceptor segment layer (PRS) while non-stained Müller cells are visualized as dark tubes elongating through the inner plexiform layer (IPL). Scale bar 10 µm.

5 Discussion

The next chapter provides a comprehensive picture about the performed experiments and the obtained results in consideration of the current state of the research. First, I explain the advantages of the applied setup, developed to gain insights into the light guidance of Müller cells, compared to other known methods. A detailed description of light scattering across the different retinal layers is presented wherein all facts are put in context to previous findings and theoretical predictions from Mie theory. Then, the optical function of Müller cells is discussed regarding its relevance for each tissue layer and its role in terms of retina optics. Special attention is paid to the comparison of light guidance between Müller cells and photoreceptors in order to draw conclusions from the interactions of light with biological material. Finally, I elaborate an encompassing theory describing the meaning of Müller glial cells for the visual perception of vertebrates.

5.1 A New Method to Study the Müller Cell Light Guidance

Recent research activities of my lab with regard to the inverted design of the vertebrate retina revealed remarkable differences of the optical properties for Müller cells compared to other cellular structures of the retina. However, none of the developed setups was able to provide all necessary information to find clear evidence for the existence of light guiding Müller cells within the vital retinal tissue.

For this reason, I established a new method that combined and enhanced all previous approaches to gain an overall picture about the influence of Müller cells in the transretinal pathway of light (see section 4.1, Agte et al., 2011). The experimental setup offers the possibility to illuminate the vital retina with a laser beam, small enough to target light on individual Müller cells embedded within their natural environment. Besides a visualization of the incoming light, it also allows the detection of light propagation through each retinal layer whereas the optically relevant Müller glial cells and photoreceptors are separately marked by a vital dye. Simultaneously, it provides an imaging of the light transmission behind the tissue that represents the final visual stimuli arriving at the photoreceptor segments. A dynamic change of the illumination achieves an assignment of variations in the propagating and transmitted light structure with respect to Müller cells and thus completes the spatial behavior of light within the retinal tissue. In particular, all experiments were carried out on freshly dissociated retinaec which were treated under appropriate conditions to ensure the cellular vitality, i.e. the full physiological functioning during data aquisition.

As mentioned above, all previous methods involved technical drawbacks. In a first set of experiments, the back-scattering of light within a piece of a guinea pig retina was measured by using a confocal microscope in reflection mode (Franze et al., 2007, Reichenbach et al., 2012). The three-dimensional reconstruction of the scanned images visualized low-reflective cylindrical tubes which were unambiguously identified as Müller cells connecting the inner retinal surface with the light-sensitive photoreceptors. Figure 2.9 explains why this experimental arrangement was chosen. Actually, the dominant Müller cell processes within the inner part of the retina can only be observed if their endfeet are pointed towards the microscope objective since the tissue with vertical dimensions of around 100 - 150 μm is simply too thick to detect reliable data from the opposite surface. The distinct tubular shape of the processes is only maintained until the outer nuclear layer where the glial cell branches into thin cytoplasmic arms. An irregular orientation of photoreceptor segments additionally impedes the optical penetration from the photoreceptor side. Consequently, to directly examine the passage of light through Müller cell stem processes, the outer part of the retina including the photoreceptor cells has to be removed. This was done by a surgical procedure in another type of experiment from Franze et al. (2007) before the sample was placed on top of an inverted microscope stage (Reichenbach et al., 2012). Physiological illumination of a wide retinal surface region was mimicked by laser light coming from a multimode fiber above the sample. The aquired images taken from below revealed the negative pattern of the images detected in the previous back-reflection experiments. Hence, the long tubular Müller cell stalks relay light better than the cellular formations they are embedded in.

Based on these new fundamental findings, several methods were engaged to elucidate the Müller cell-dependent transport of light. First of all, a light source small enough to simulate the natural illumination of single Müller cell endfeet was needed. Thus, the previously used wide-field illumination was replaced by a small single mode fiber whose tiny beam waist and moderate divergence provided suitable conditions to fulfill the imposed requirements. To get an idea how light passes the tissue layers through a single Müller cell towards the light-sensitive photoreceptors, the single mode fiber was mounted vertically above the vital tissue and moved stepwise (stepsize 1 μm) in horizontal direction (Agte et al., 2011; Reichenbach et al., 2012). An inverted microscope recorded the illuminated photoreceptor segments. In contrast to the straight continuous positioning of the fiber, the illumination pattern on the opposite surface only jumped after every tenth fiber step. Interestingly, this distance was coinciding with the averaged spacing of Müller cells within guinea pig retina and thus additionally supported the hypothesis of a glial cell-dependent propagation of light.

To finally answer the question of the underlying mechanism for this transretinal light transport, it could be concluded that Müller cells merely have a lack of phase variations, i.e. of scattering particles (section 2.2.3), so that light is transmitted along their length only due to the transparency of the cell body. Another promising theory was that the transport mechanism is based on the physical principle of light guidance similar to photoreceptor segments which were already identified as living light fibers within the outermost part of the tissue (Figure 2.11).

As already introduced in section 2.2.3, the latter assumption was successfully demonstrated for isolated Müller cells (Figure 2.14; Franze et al., 2007). This proof was performed by means of an experimental setup based on a dual-beam laser trap where an increase of the light transmission served as indication for light guidance. As already discussed in 2.2.3, it is expected that such an increase of the transmitted light intensity is not specific to Müller cells since every suspended cell in this setup would yield a rise in the light transmission. Furthermore, an isolation of Müller cells from their natural environment is accompanied by a change of the optical properties since suspended cells are fragile and subject to osmotic variations (Barer, 1957; Beuthan et al., 1996). One can imagine, an osmotic swelling or shrinkage of Müller cells is associated with a reduction or increase of the refractive index. Moreover, a change of the Müller cell volume automatically changes the cell diameter which in turn behaves proportional to the V-parameter (see equation 2.29). But even if the preparation was perfect and the shape and optical nature of a Müller cell was maintained, the interstitial material, the cells are embedded in and which is crucial for a wave guiding behavior of Müller cells, cannot be imitated authentically for isolated cells (section 2.2.3).

In conclusion, up to this point either the physiological conditions did not meet the requirements, or the experimental configuration limited the detection of important data. In contrast to this, my setup ultimately offers a comprehensive impression about the Müller cell-dependent illumination, propagation and transmission of light which finally provides a detailed insight into the light guiding properties of Müller cells.

5.2 The Retina as Scattering Tissue

Light inside the retina gets scattered if laser light is applied onto the retinal surface whereas light is inhomogeneously distributed throughout the tissue resulting in a characteristic scattering pattern (Figure 4.6 c). While almost all scattering is concentrated within the two plexiform layers, only a small fraction of laser light comes from the three nuclear layers (see section 4.3).

This observation is an outcome of the distinctive size distribution of cellular components within the alternating plexiform and nuclear layers (Figure 2.9). The relationship between scattering and particle size was introduced in detail in section 2.1.3. Plexiform layers mainly consist of dendrites and synaptic contacts whose dimensions are close to the wavelength of visible light, i.e. of the laser used in the experiments (Figure 2.9 c). As schematically demonstrated in Figure 2.6 (f) and (g), this case falls into the so-called Mie regime where strong interactions occur due to interference effects (Figure 2.5). With respect to biological tissues, the scattering behavior can be compared with those of mitochondria, lysosomes, peroxisomes and other organelles in the same order of magnitude. As summarized in Table 2.1, those structures mainly contribute to scattering in an angular range from 40 - 170° which includes the angle of observation in my experiments ($\theta = 90°$). According to Table 2.1, scattering from nuclei is expected in angles of 5 to 40° which is consistent with the low intensities recorded in the nuclear layers. It should be noted that such an analogy is more meaningful than it may seem since the angular ranges listed in Table 2.1 were almost exclusively measured on suspensions consisting of isolated cells or organelles. The interaction of light with suspended particles can be approximated by Mie theory, which means an increasing volume of the object is accompanied with a prominent scattering in forward direction (see Figure 2.6). Only recently, it was successfully demonstrated that the ray optics approach, which represents a simple solution of Mie theory, is applicable to single suspended cells, i.e., the cell soma focuses light similar to an optic lens (Grosser, 2011). But as discussed in section 2.1.4, it is not a matter of course that cells in a tissue work with the same principle. Thus, several authors used theoretical FDTD simulations to analyze the passage of light through clusters of heterogeneous cells or nuclei. In fact, they achieved optimistic results showing that a lensing effect is also valid for cells embedded within biological tissue (Starosta and Dunn, 2009; Kreysing et al., 2010; Solovei and Joffe, 2010). Altogether, the low scattering intensity of nuclei in my experiments is most likely attributed to their size which considerably exceeds the wavelength of light and thus causes scattering in forward direction. A lensing effect might be the underlying mechanism.

Some publications reported similar findings about a non-homogeneous proportioning of light within the morphologically different layers of the vertebrate retina. It was common to most of the studies that particularly the small subcellular structures of the inner and outer plexiform layers were identified as main contributors to retinal light scatter (Boehm, 1940; Martins-Ferreira and Castro, 1966; Castro et al., 1985). For instance, in the previously mentioned back reflection experiments from Franze et al., 2007, the scattering was also primarily evoked by the synaptic layers. Additionally, they recorded scattering from axon bundles at the retinal surface which is conform with data from Knighton et al. (1989).

This effect seems to be less prominent in my data but can be explained by the fact that I used retinal pieces from peripheral regions where nerve fibers are less numerous. If axon bundles were located in the small illumination cone of the single mode fiber, scattering signals were detected (Figure 4.5, e and g). Furthermore, Knighton et al. (1992) found a high directional sensitivity of the light reflection from nerve fibers where the angular reflectance of the nerve fiber layer changes with the orientation of the nerve fiber bundles. This might be an additional reason for a varying degree of scattering intensities between the various methods that often differ in illuminating and viewing angles (Knighton et al., 1992). A later study by Knighton and Huang (1999) finally demonstrated that reflectance at wavelength below 570 nm arises from small cylindrical tubes with diameters smaller than the wavelength of light, i.e. by Rayleigh scattering on microtubules and neurofilaments in the nerve fiber layer.

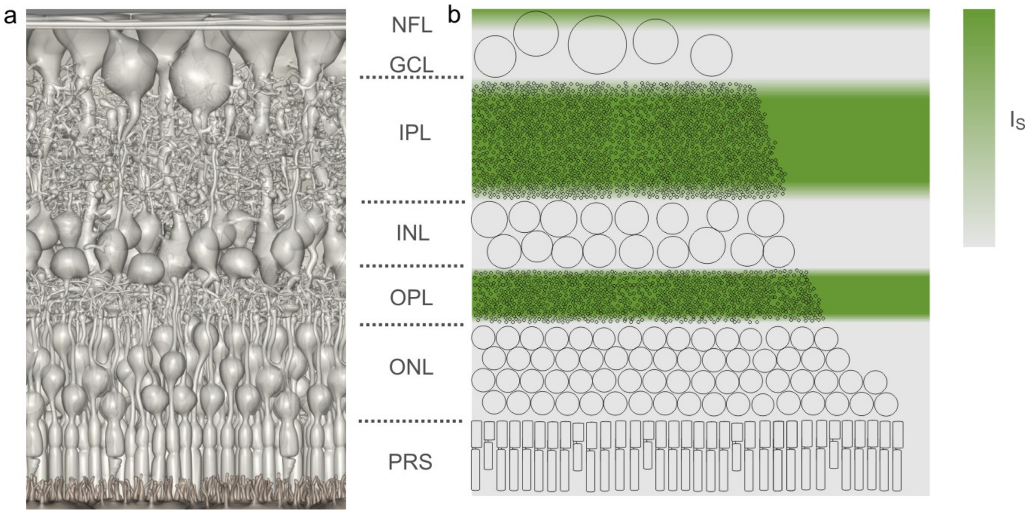

Figure 5.1: The retina as scattering tissue. Light inside the retina gets scattered in dependence on the size, shape and organization of the particles constituting the tissue layers. (a) Illustration of the retinal cross section. Image courtesy of J. Grosche. (b) Schematic drawing of the scattering distribution within the retina without the influence of Müller cells (I_S, scattering intensity, the darker the green the higher I_S). Particles are roughly approximated as spheres (circles), except for the photoreceptor segments. Particulary strong scattering (dark green) occurs within the two plexiform layers (IPL, OPL) and in the nerve fiber layer (NFL) due to cellular structures with dimensions in the order of the wavelength of visible light, i.e. microtubules, synapses or dendrites. The three nuclear layers (GCL, INL, ONL) and the photoreceptor segments (PRS) evoke less light scattering (light grey).

Besides this consideration, it should be noted that the retinal surface represents the border between two different refractive media. The mean refractive index of the retina was estimated to around 1.36 while the aqueous vitreous body with a value of around

1.335 is comparable to water (Valentin, 1879; Nordenson, 1934; Ajo, 1947; Chen, 1993; Franze et al., 2007). Indeed, literature reports about specular reflections from the inner limiting membrane which are obvious as fundus reflexes in ophthalmology (Charman, 1980; Gorrand, 1986; Reichenbach et al., 2012). Moreover, ophthalmic research also provides one of the most convincing arguments for an inhomogeneous scattering of light within the retina. Optical coherence tomography (OCT), widely used in clinical diagnostics, actually takes advantage of the different scattering efficiencies of various subcellular components to image individual retinal layers in intact eyes of human patients (Puliafito et al., 1995; Ko et al., 2004).

To conclude, the general behavior of retinal light scattering observed in my experiments is predetermined by the size of the scatterers (compare Figure 5.1 with Figure 2.9 b) and is consistent with theoretical predictions (see sections 2.1.3 and 2.1.4). The associated distribution of light very well corresponds to characteristic patterns found in literature. Altogether, the main constituents of the retina act as scattering objects.

5.3 Müller Cells Are Wave Guides within the Retinal Tissue

During a lateral shift between retina and light source, the characteristic scattering pattern described in the previous section was modified in dependence on the presence of Müller cells. If the cone of light solely illuminated an individual Müller cell, the scattering within the tissue was reduced (section 4.3). Simultaneously, the transmitted light behind the tissue was confined to a rather narrow area which indicates that light along the retinal path is hindered in its original divergence since it is trapped within the cylindical Müller cell volume (Figures 4.6 and 5.2 a). Both observations, i.e. a reduction in light scattering plus a conservation of the light divergence, are characteristic features of wave guides (Saleh and Teich, 1991; Bass, 1995). In other words, the recorded behavior unambiguously identified Müller cells as living light fibers within their natural neuronal environment (Agte et al., 2011; Reichenbach et al., 2012). In contrast, when the same experimental approach was applied to other biological tissues, e.g. liver tissue which is known for its pronounced scattering properties due to an extraordinary high number of mitochondria within hepatocytes (Figure 2.7 b), the resulting light structure was not subject to significant fluctuations. Neither the tissue scattering nor the light divergence varied during a stepwise change of the beam location (Figure 5.2, b and c). Since all biological materials generally consist of the same cellular components, only a special organization of structural inhomogeneities within Müller cells and the surrounding neuropil might be responsible for the observed guidance of light through the inverted vertebrate retina (see section 2.1.2).

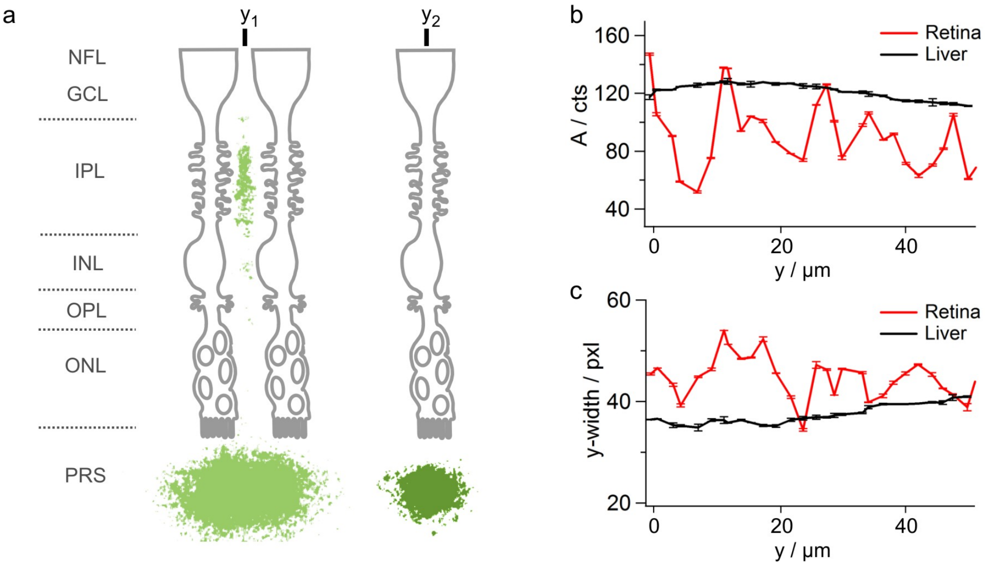

Figure 5.2: Müller cells are wave guides. (a) Retinal light path influenced by the Müller cell light guidance (y_1 and y_2, positions of the light source). The obtained scattering data are overlayed with schematic drawings of Müller cells. (b, c) Comparison of the tissue scattering (represented by the parameter A) and the final beam dimension (represented by the parameter *y-width*) between retina and liver tissue (150 µm slice) during a stepwise motion of the light source. Data were recorded with the optical fiber setup (section 3.2.1).

5.3.1 Influence of Cellular Morphology on the Interaction with Light

The impact of cell morphology on the behavior of light actually gets clearly visible by the layer-dependent light scattering (see section 5.2). Conversely, this implies that the need for a light guiding structure is quite different for each retinal layer. In fact, along the transretinal light path, I recorded a varying degree of the light guiding ability of Müller cells (section 4.3, Agte et al., 2011) which is most likely attributed to the complex Müller cell morphology and ultrastructure (Figure 2.12). Particularly, the prominent scattering of light within the inner plexiform layer was drastically diminished by up to 50 % (Figure 4.8 b). In this layer, the morphological shape of the inner stem processes of Müller cells most closely matches the design of industrial glass fibers (Figure 4.5) which in turn suggests that long cylindrical tubes seem to be an optimal solution to bypass accumulations of numerous strong scatters. However, not only the shape but also the anatomical composition of the Müller cell processes completely differs from the surrounding synaptic meshwork (see Figure 5.3). As already described in section 2.2.3, organelles with sizes similar to the visible wavelength are rare or even absent (Reichenbach, 1989). For instance, guinea pigs have an avascular retina where mitochondria are not evenly distributed across the Müller cell but are rather accumulated in its outermost part, i.e. in the end of the transretinal light path (Germer et al., 1998). Additionally, the nucleus is not symmetrically positioned in the center of the cell body as this is usual for elongated cells like photoreceptors or bipolar cells (compare Figure 2.9), instead the nucleus is laterally displaced from the cell axis (Figure 5.3 b). There is extensive literature concerning the influence of organelles in cellular light scattering. Section 2.1.4 gives detailed insights into the current state of the research. As visually summarized in Figure 2.7, the organelle volume fraction is mainly responsible for the scattering properties of biological cells and tissues. Thus, an elimination or just a displacement of organelles as in Müller cell processes may facilitate an unimpeded transport of light on the basis of light guidance. In order to study the influence of organelles with respect to Müller cell light guidance, the distribution of mitochondria could be experimentally regulated by an increase of the partial oxygen pressure which would finally lead to a migration of mitochondria in other parts of the glial cell (Reichenbach, 1999). Besides an almost organelle-free cytoplasm, another peculiar formation of cellular material within Müller cell endfeet and inner processes was found. Normally, intermediate filaments are randomly organized across the cell (Helfand et al., 2004), but intermediate filaments in Müller cells follow a straight orientation along the transretinal light path (Reichenbach, 1989; Reichenbach and Bringmann, 2010). Interestingly, the same alignment was found for the rigid rod-like microtubuli in the outer processes of the cell (Reichenbach, 1989; Pampaloni et al., 2006). To potentially analyze the involvement of intermediate filaments in the light guiding function, the use of genetically modified Müller cells lacking in vimentin or glial fibrillary acidic protein (GFAP) may be helpful (Pekny et al., 1999). So far, one can only speculate about a contribution of such an alignment to an elevated re-

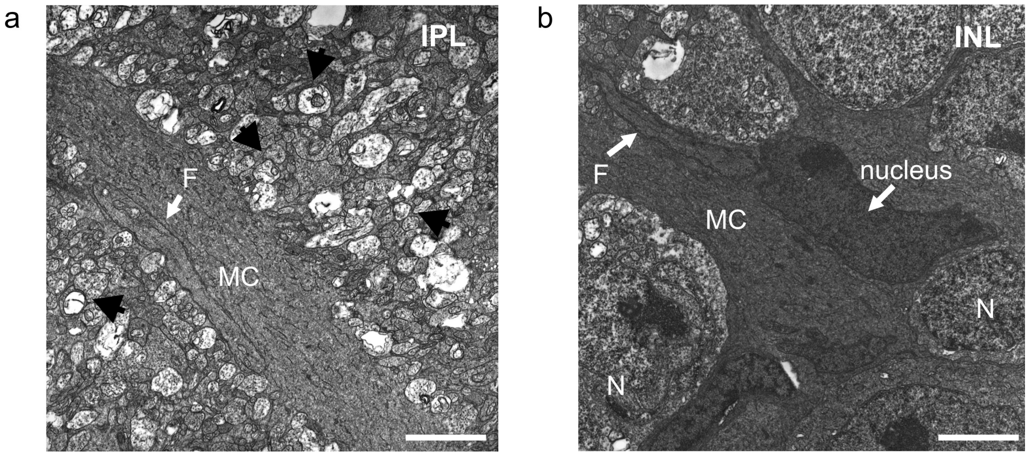

Figure 5.3: Müller cell ultrastructure. (a) Transmission electron micrograph of a guinea pig Müller cell (MC) passing synaptic particles (black arrows) in the inner plexiform layer (IPL). The cellular volume is devoid of organelles with sizes in the order of the visible light. Intermediate filaments (F) are oriented along the light path. (b) The nucleus in the inner nuclear layer (INL) is positioned laterally from the stem process (N, nucleus of neuron). Scale bars 3 μm. Images courtesy of M. Francke.

fractive index. Nevertheless, my experiments demonstrate that refractive index variations between Müller cells and their environment exist and therefore confirm previous refractive index measurements on isolated retinal cells from Franze et al. (2007) (Figure 2.13).

Based on these measurements from Franze et al. (2007), the key parameter for wave propagation also known as V-parameter (equation 2.29) was estimated to be around $V \approx 4$ for $\lambda = 500$ nm. This value is well above $V = 2.4$ since for $V < 2.4$ only the fundamental mode LP_{01} is guided while all other modes are cutoff, i.e., the fiber operates as single mode wave guide (Saleh and Teich, 1991). Conversely, this means that guinea pig Müller cells act as multimode fibers. However, the V-parameter most likely exceeds a value of 4. On the one hand, in their calculations Franze et al. (2007) used the maximum possible refractive index of the surrounding material, i.e. that of the neuronal soma (see section 2.2.3). The refractive index usually behaves linearly with the dry mass which is known to be densest in the cell nucleus or referred to the retina in the nuclear layers (Barer, 1957; Brunsting and Mullaney, 1974; Beuthan et al., 1996). Plexiform layers presumably have a lower refractive index resulting in an elevated wave guide parameter V for Müller cell processes. On the other hand, Müller cell processes in the plexiform layers extend numerous fine side branches to physiologically contact neighboring neurons or blood vessels (Figure 5.4 a; Reichenbach and Bringmann, 2010). From an optical point of view, one can imagine that the effective diameter of the wave guide d_{E} is probably larger than the diameter of the stem process d_{P} which in turn would contribute to an increased V-parameter. Given this assumption, the refractive index profile presumably would match the profile of graded index fibers where the refractive index has its peak in the center and gradually decreases with radial distance (Figure 5.4, b and c; Saleh and Teich, 1991). Index grading is a

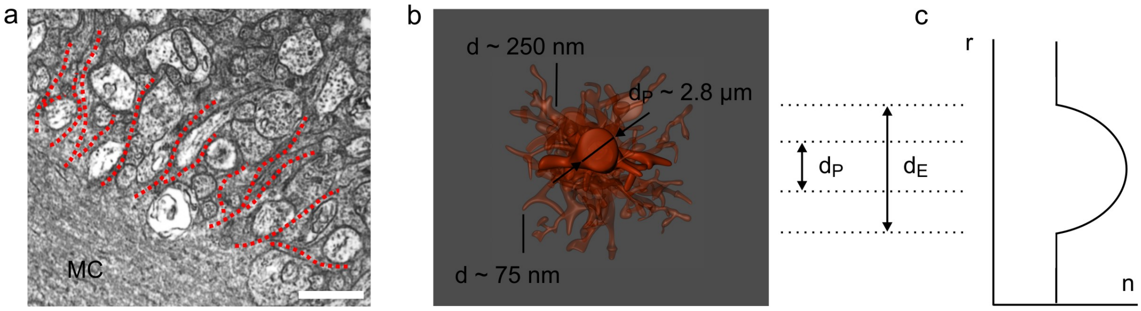

Figure 5.4: Cytoplasmic side branches of Müller cell stem processes potentially enhance the V-parameter. (a) Border of a Müller cell in the inner plexiform layer; numerous fine branches (red dotted lines) extend into the surrounding synaptic tissue. (b) Cross section of an inner Müller cell stem process. The side branches probably increase the diameter of the process d_{P} to an effective diameter d_{E}. (c) Assumed parabolic refractive index profile $r(n)$ which is comparable to that of graded index fibers. Image courtesy of J. Grosche.

method to reduce pulse spreading caused by modal dispersion in multimode fibers. In other words, it decreases the differences between the delay times of the modes travelling through the wave guide with different group velocities (Saleh and Teich, 1991). However, modal dispersion usually occurs for core diameters of around 50 µm and fiber lengths in the order of kilometers which is not comparable with microscopic Müller cell dimensions. Thus, further research is required to verify if the side branches indeed contribute to the optical function of Müller cells.

Based on several clinical and physiological observations it can be concluded that the light guiding function of Müller cells in fact plays a key role in retina optics. In retina pathology, many diseases, in which especially Müller cells were identified to loose their original shape and anatomical structure such as posterior uveitis (Deeg et al., 2006; Eberhardt et al., 2011) or retinal detachment (Wurm et al., 2006), are macroscopically accompanied by a turbid appearance of the retina (Reichenbach et al., 2012). During spreading depression, a phenomenon where extreme intra- and extracellular ion concentrations temporarily paralyze the retinal function, a spontaneous 'milky wave' is running across the surface of the tissue (Gouras, 1958). As described in section 2.2.3, Müller cells are mainly responsible to maintain the ion and water homeostasis of their neuronal environment. Large changes of ion concentrations drastically alter the osmotic conditions for Müller cells which might affect their refractive index and the associated light guiding function (Mori et al., 1976). Data from several studies finally provided direct evidence that spreading depression indeed changes the light scattering properties, especially the scattering within the inner plexiform layer remarkably increased (Figure 5.5; Martins-Ferreira and Castro, 1966; Castro et al., 1985). As shown in my experiments, the light guidance of Müller cells is particularly efficient within this retinal layer. Conversely, a loss of this feature would primarily result in an increase of the plexiform scattering. Taken together, a decline of the Müller cell light

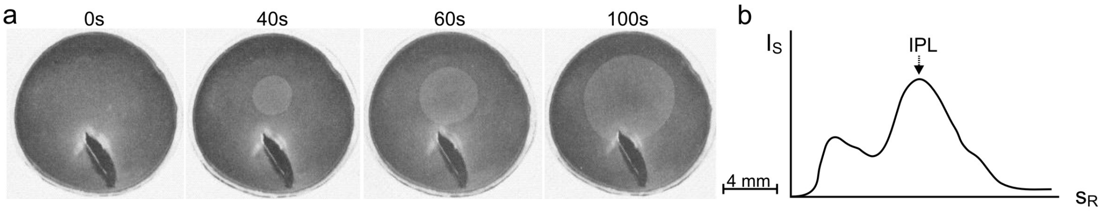

Figure 5.5: Spreading depression is accompanied by changes in light scattering. (a) Microphotographs of a chicken retina at different time points after stimulation of spreading depression. Strong changes of the retinal ion and water homeostasis, which is predominantly maintained by the Müller cell, are accompanied by changes in light scattering. Macroscopically, a circular wave propagates across the retina. (b) Light scattering I_S along the retinal layers (s_R, retinal depth). In particular, strong scattering occurs within the inner plexiform layer (IPL). Images adapted from Martins-Ferreira and Castro (1966).

guidance might be a possible explanation for the turbidity of the retinal tissue observed for several pathological phenomena which provides new impulses for further investigations.

As already stated, the influence of Müller glial cells in the scattering behavior is dependent upon the retinal layer. For instance, in any arbitrary position of the light source, the scattering at the tissue surface was less pronounced than in the inner plexiform layer. Nevertheless, if the beam was right centered in front of a Müller cell an additional decrease of the surface scattering was recorded (Figures 4.5, b and f, and 4.7). This result represents a direct proof that the retinal surface, i.e. the light-facing side of the tissue, is lined by a low-refractive material in order to reduce back reflections evoked at the border between vitreous and retina. In fact, the numerous Müller cell endfeet fuse into a smooth homogeneous matrix covering the entire surface of the retina (Figure 3.4). Moreover, Franze et al., 2007 detected a gradual decrease of the refractive index from the inner stem process towards the Müller cell endfoot, shown in Figure 2.13. The latter was estimated to be around 1.35 - 1.36 which is almost exactly the half between the refractory indices of the aqueous vitreous ($n = 1.335$) and the high-refractive portion of Müller cells ($n = 1.38$). Thus, this value is in an appropriate range to minimize surface reflections and, consequently, to guarantee a high efficient transfer of light into Müller cells. This might explain the additional decrease of the surface scattering if the light source was positioned in front of the endfoot center.

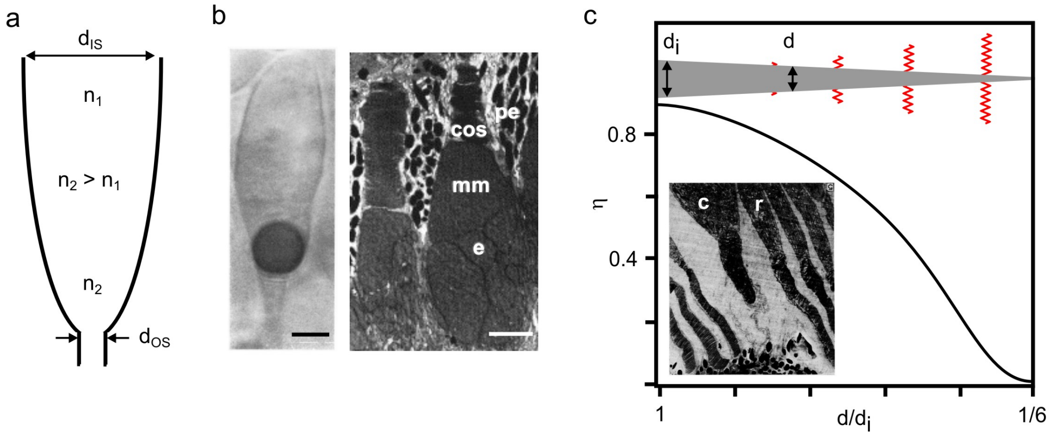

Figure 5.6: Tapered inner and outer segments of cone cells. (a) Inner segment of a cone cell with a ratio of 4.5 between entrance d_{IS} and exit aperture d_{OS}. The smaller the diameter the higher the refractive index (n_1 and n_2, refractive indices). (b) Inner segment of a large turtle cone with oil droplet (left). Scale bar 5 µm. Large cone of tree-shrew with megamitochondrion (mm). (cos, cone outer segment; e, ellipsoid; pe, pigment epithelium) Scale bar 2 µm. Images taken from Baylor and Fettiplace (1975) and Knabe et al. (1997). (c) Behavior of light for tapered outer segments without refractive index gradient. The smaller the diameter d of the wave guide the smaller the fraction of light η within the cell, i.e. the more light gets radiated (d_{i}, diameter of the entrance aperture). Inset: Transmission electron micrograph of cylindrical rod (r) and tapered cone outer segments (c) in the human retinal periphery. Image adapted from Miller and Snyder (1972).

Furthermore, the coupling of light into the cell is also favored by considering the gradient from the other direction, i.e. the stronger the tapering towards the stem process the higher the index of refraction. The same correlation was reported for the tapered inner segments of photoreceptor cells where a large mitochondrial content of the ellipsoid at the junction to the outer segment ($n \approx 1.40$) causes a higher refractive index than the surrounding myoid matrix ($n \approx 1.36$) (Sidman, 1957). Without this specific design, the light supposedly cannot be trapped within the tapered ellipsoidal region because the fraction of light inside a wave guide η depends on the V-parameter (equation 2.29) which in turn behaves proportional to the diameter and the numerical aperture of the light guiding structure (Miller and Snyder, 1972; Hoang et al., 2002). Thus, the only way to compensate a smaller diameter is a rise of the refractive index in order to guide the light more efficiently into the slender outer segments (Figure 5.6 a). In particular, the tapered shape of the cone cells became subject to several studies, e.g. morphological data on diurnal macaque, published by Hoang et al. (2002), have shown that 74 - 85 % of the ellipsoidal volume of cones is filled with mitochondria while rod ellipsoids have a mitochondrial content of only 54 - 66 %. Interestingly, cone inner segments often contain high refractive roundish bodies such as oil droplets (Baylor and Fettiplace, 1975), paraboloids ($n \approx 1.38$; Sidman, 1957) or megamitochondria ($n \approx 1.41$; Figure 5.6, b; Knabe et al., 1997). The photopic vision mediated by cone cells requires high light intensities (section 2.2.2). Thus, without a strong refraction towards the outer segments most of the light would be absorbed by the pigment epithelial cells in the spaces between the outer segments or it would reach neighboring cones what finally would lead to image distortion.

Apart from those discussions about receptor optics, the image arriving at the receptor array would be already distorted if the light, at the beginning of the transretinal light path, is not efficiently coupled into Müller cells. As depicted above, the current research provides strong indications for Müller cell endfeet working with the same principle as the tapered segments of photoreceptors. Nevertheless, it remains unclear what type of cellular structure generates the high refractive index. In general, an elevated concentration of any protein is required. As already mentioned, the huge amount of aligned intermediate filaments presumably contributes to such an optical formation. An additional explanation for the funnel-shaped ending of Müller cell light fibers might be the adaptation for a wide-angular acceptance of incoming light at the entrance aperture. Winston and Enoch (1971) published a simple geometrical model for the inner segment of cone cells and found that the tapered design is accompanied with an increased acceptance angle. However, this ray model is only applicable to relatively large cone cells of some species (Enoch et al., 1981), e.g., it fits surprinsingly well to experimental results obtained on turtle cones (Figure 5.6 b; Baylor and Fettiplace, 1975). Analogical speculations were made for the funnel-like terminations of light guiding siliceous spicules in marine sponges whose overall shape shows striking similarities with Müller cell endfeet (Brümmer et al., 2008).

Another theory does not consider the light trapped within the tapered structure but rather the amount of light which leaves the fiber if no refractive index gradient compensates the decrease in diameter. According to equation 2.29, Figure 5.6 (c) shows the fraction of light that remains within the receptor. Obviously, the smaller the dimension of the wave guide the less light is guided and the more modes may cease to be bound and are finally lost by radiation. In photoreceptor optics, Miller and Snyder (1973) suggested a potential benefit of the extreme taper of cone outer segments in the retinal periphery. The authors suggested all light that is not absorbed by the cone visual pigments gets uniformly distributed throughout the adjacent rod outer segments and thus enhances the sensitivity of the rod system at scotopic light levels (Figure 5.6 c; Miller and Snyder, 1973). Likewise, this theory might be applied to Müller cells at the border to the outer nuclear layer where the thick outer stem process (≈ 2 - 3 µm) tapers to numerous fine cytoplasmic extensions whose diameters of $d \leq 0.5$ µm are definitely too thin for a sufficient transport of light (Figures 4.1 and 5.7 b). However, if the light gets radiated, where does it go? Before it is captured by the light-sensitive segments, it still has to pass the outer nuclear layer which is particularly thick in the retina of night active animals due to the huge number of rod cells. In fact, only recently, Solovei et al. (2009) discovered a functional relationship between the light conditions of the animal lifestyle and the nuclear architecture of rod photoreceptors. They found that the chromatin pattern of rod nuclei from nocturnal mammals has an unique inverted design (Figure 5.7 a). In contrast to the conventional

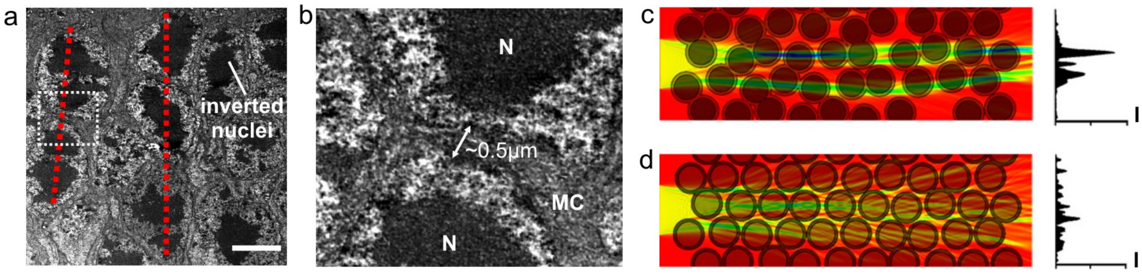

Figure 5.7: Optics of the outer nuclear layer. (a) Transmission electron micrograph of the outer nuclear layer of guinea pig retina. The rod nuclei have an inverted chromatin structure where the dense heterochromatin (black) is accumulated within their center. The nuclei are aligned in columns (red line). Scale bar 4 µm. (b) Inset of panel (a), indicated by the white box. The thin cytoplasmic Müller cell sheaths (MC) are too small for an efficient guidance of light. However, they are responsible for the structural organization of the columnar arrangement of the nuclei (N). Image courtesy of M. Francke. (c, d) FDTD-simulations of light propagation ($\lambda = 500$ nm) through stacks of conventional (d) and inverted nuclei (c). The intensity along the path is color coded. Diagrams show the resulting intensity profiles behind the different nuclei arrangements (I, intensity). Images adapted from Solovei et al. (2009).

architecture, the dense, i.e. high-refractive, material is positioned in the center of the roundish nuclei which gave reason to think of the nuclei as microscopic lenses in order to improve the photon yield during night vision. Therefore, a theoretical analysis based on numerical finite-difference time-domain and analytic Mie theory approaches was used to model the light propagation through stacks of photoreceptor cell nuclei. As a result, the transport of light through inverted nuclei was shown to be more efficient than for the conventional pattern in diurnal animals (Figure 5.7, c and d; Solovei et al., 2009). This efficiency was robust against several parameters like the irregularity of the columns, refractive index variations or the number of rod nuclei placed over each other. In other words, just the reorganization of only a single component within a cell may drastically influence the interaction with light. However it should be noted that the simulations are based on experimental data measured on isolated nuclei and thus do not represent the real conditions within the vital retina. Another critical aspect arises from the simplified modeling of the nuclear architecture since it was simulated as a spherical core surrounded by a peripheral shell, both with a homogeneous refractive index distribution. As shown in Figure 5.7 (a) and (b), these assumptions deviate from the original construction.

The data presented in this thesis provide first experimental insights into the propagation of light through the intact outer nuclear layer. Guinea pigs have a crepuscular to diurnal lifestyle (Krishnamoorthy et al., 2008) but about 95 % of their photoreceptor cells are the highly-sensitive rod cells (Reichenbach and Robinson, 1995) whose nuclear chromatin structure exhibits the same inverted architecture as found in nocturnal mammals. In accordance to the theoretical data from Solovei et al. (2009), I recorded low sideward scattering intensities from nuclei of photoreceptors (Figures 4.5 and 4.9 b). Even if Solovei et al. (2009) observed no remarkable differences in light scattering for varying degrees of nuclei arrangements, the conspicuous orientation in regular columns speaks for itself (see Figure 5.7 a). It might enhance the lensing effect. Interestingly, Müller cells are in close contact with the photoreceptor membrane via so-called adherens junctions whose contractile proteins play a crucial role in the retinal arrangement, i.e. also in the alignment of rod nuclei (Drenckhahn and Wagner, 1985; Reichenbach and Bringmann, 2010).

Furthermore, my measurements did not show considerable scattering within the layer of photoreceptor segments which appears quite reasonable considering their ability to guide light (section 2.2.3). Similar to Müller cells, the light within the tubular inner and outer segments propagates perpendicular to the microscope objective (Figures 2.11, 4.5 and 4.9 c).

To sum up, the Müller cell morphology and ultrastructure are adapted according to demand. The higher the risk of light scattering, e.g. in the inner plexiform layer, the more efficient the transfer of light due to a structural rearrangement of the cellular components in comparison to the conventional cell construction. Those variations to the standard are driven by selective pressure in order to increase the evolutionary benefits. The nervous system is of particular importance at the interface between morphology, physiology and the subsequent behavior of the organism (Niven and Laughlin, 2008). Consequently, a change of the molecular density and reorganization of structural inhomogeneities within Müller cells and photoreceptors represent an evolutionary success for vertebrate vision to compensate the scattering caused by an inversion of the retinal tissue.

5.3.2 Coupling Efficiency

To further characterize the wave guide behavior of Müller cells, my analysis was focused on the scattering signal at the level of the inner plexiform layer where the need for an efficient light guiding element is of particular importance. In this layer the Müller cell light guidance causes the most striking reduction of light scattering, as it was highlighted in the previous section. Similarly, the Müller cell-dependent light transmission was chosen for a detailed consideration. Thus, the light structure at both locations, i.e. within and behind the tissue, was parameterized to receive quantitative data representing the transport of light through the inverted retina (section 4.4). The evaluation revealed that the scattering evoked by the inner plexiform layer as well as the beam diameter arriving at the receptor cells behave contrary to the fluoresence intensity of Müller cells (Figures 4.13 and 4.14). The cell fluorescence and the maximum intensity of the transmitted light correlate in a positive manner (Figure 4.15). Furthermore, it was demonstrated that both, the intraretinal and the transmitted light structure change simultaneously as expected for light guiding cables (Figure 4.16). A statistical test procedure supplied the final evidence that the Müller cell-dependent changes indeed occur in a significant way. The averaged changes of the parameters amount to values of 7 and 18 percent, thus the averaged relative light guiding efficiency η_r is around 1.21 with a maximum of 1.36 (Figures 4.17, 4.18 and 4.21). Nevertheless, it should be noted that only the well-defined cases with a clear classification, i.e. either with or without a Müller cell, yielded significant results.

For the latter, a plausible explanation exists which by no means contradicts to the light guiding function of Müller cells but rather supports the described findings. In principle, the situation in my experiment corresponded to that in optic cable connectors where two fibers are brought in contact in order to couple light from one fiber end to the other. Figure 5.8 summarizes the most common factors affecting the connection between two step index multimode fibers. Coupling losses can be differentiated in intrinsic coupling losses occurring due to propagation characteristics of the fibers being joined and extrinsic coupling losses that arise from mechanical misalignments between the emitting and the receiving fiber, i.e. fiber 1 and 2 in Figure 5.8 (Thiel and Hawk, 1976).

Accordingly, discrepancies in the cores, i.e. mode field diameters, and the numerical apertures, i.e. refractive index differences between core and cladding material, belong to intrinsic losses. Panel (a) of Figure 5.8 illustrates the linear dependence of these losses to the core (a_1/a_2) and numerical aperture mismatches (NA_1/NA_2), respectively. For both cases, Thiel and Hawk (1976) reported that a discrepancy of already ± 1 % generates considerable losses. The mode field diameter of the light emitting fiber in my setup was 3.5 ± 0.5 µm whereas the mode field of a fiber is slightly larger than its core (Figure 3.13). Thus, the core diameter d_c is relatively close to the diameter of the inner process from guinea pig Müller cells of around 2 - 3 µm. In addition, the endfoot which is approximately 4 - 5 times larger might reduce the ratio a_1/a_2 and thus the associated losses. Taking the acceptance angles calculated for the used glass fiber and the Müller cell (see sections 3.2.2 and 3.2.5) the ratio NA_1/NA_2 reveals a value of around 0.79.

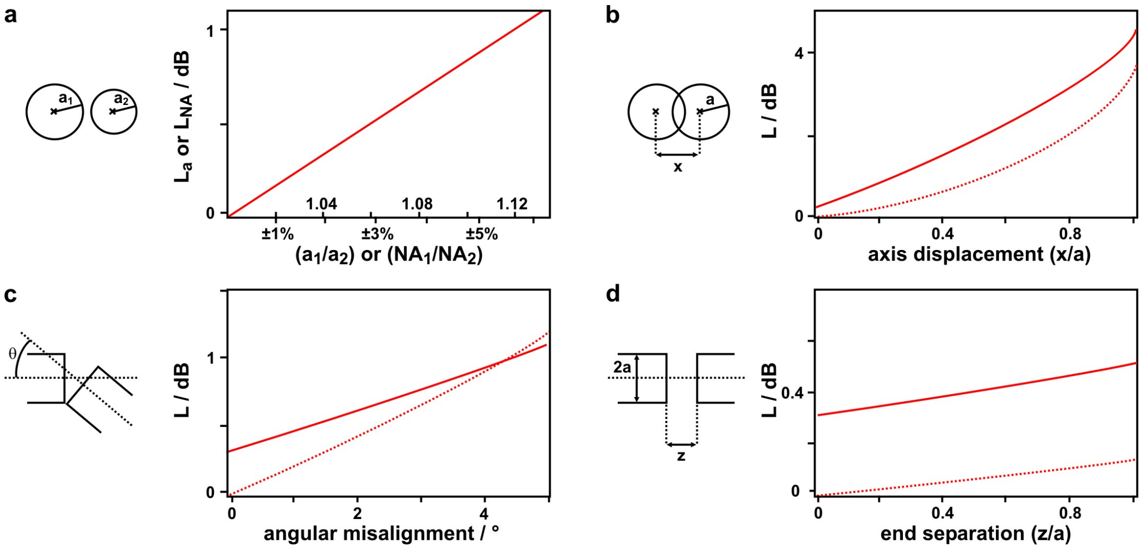

Figure 5.8: Intrinsic and extrinsic coupling losses between multimode step index fibers. (a) The intrinsic (fiber-related) losses L_a and L_{NA}, caused by mismatches in the core diameters and numerical apertures, linearly behave with a_1/a_2 and NA_1/NA_2, respectively. The index number 1 describes the emitting and number 2 the receiving fiber. (a, core radius; NA, numerical aperture) (b-d) Extrinsic (technique-related) losses due to lateral (x/a), angular and longitudinal (z/a) misalignments for $K = 1$ (solid line) and $K = 1.46$ (dashed line), where $K = n_c/n_0$ with n_c as refractive index of the core and n_0 of the medium between the fibers. (x and z, axis offsets in x and z-direction respectively) Images adapted from Thiel and Hawk (1976) and Tsuchiya et al. (1977).

Extrinsic losses attributable to radial offsets, i.e. lateral offsets in x and/or y-direction between two identical fiber cores are shown in Figure 5.8 (b). The coupling efficiency is very sensitive to lateral misalignments, losses are negligible only for minimal displacements of a few percent of the core diameter (Thiel and Hawk, 1976; Tsuchiya et al., 1977).

Conversely, displacements exceeding these small variations cause notable attenuations of the transferred light intensity whereas the ratio x/a implies that the described effect becomes more obvious for a smaller core diameter. Figure 3.4 reflects the three-dimensional orientation of elongated Müller cells within the retinal tissue. This impressively demonstrates that my experiments were most likely sensitive to axis displacements. Assuming an equal staining of Müller cells for each individual experiment, the probability of optimal coupling conditions increases with the fluorescence intensity (see profiles in Figures 4.13, 4.14 and 4.15). Consistently, Figures 4.20 and 4.21 illustrate the remarkable impact of lateral displacements.

Figure 5.8 (c) shows the connecting loss in terms of angular misalignments. Apparently, already a small tilt of some degrees between the fiber axes is sufficient to reduce the light transfer. In order to avoid these losses, I used the procedure described in Figure 4.2 (b) to align the fiber with respect to the retinal tissue. Nevertheless, the random distribution and orientation of Müller cells might produce slight angular discrepancies.

Also a longitudinal separation between the fiber ends affects the quality of the cable connection (Figure 5.8 d) since the amount of light coupled into the receiving core depends on the light divergence of the emitting fiber (see section 3.2.2). In my experimental setup such kind of possible artefacts were diminished as the distance between fiber and retinal surface was usually close to the Rayleigh range, i.e. the distance without a pronounced angular spreading of light. Furthermore, the large diameter of the endfoot favored the coupling conditions (Table 3.2). Generally, all extrinsic losses can be basically reduced if both fibers are embedded in index matching fluid. The physiological solution in my sample chamber provided a similar effect (Figure 5.8, b-d).

Other factors belonging to the group of extrinsic losses are caused by a nonideal surface preparation, for example the end face roughness may produce considerable light scattering (Thiel and Hawk, 1976). As shown in the previous sections, the funnel-shaped Müller cell endfeet form a smooth continuous film covering the vitreous surface presumably to counteract those types of losses (see section 5.2). If the retinal tissue was turned, so that the photoreceptor segments were directed towards the light source, no light guidance was observed, instead most of the light was scattered and reflected by the numerous irregular oriented photoreceptor segments. In line with this, the experiment from Franze (2007), shown in Figure 2.14, revealed satisfying results only if the endfoot was pointed towards the light emitting fiber.

Moreover, the fact that the relative relative light guiding efficiency of 1.36 for a single perfectly aligned Müller cell embedded in its natural surrounding (Figure 4.21) is still below the value of 1.90, measured on isolated cells by Franze (2007), provides further arguments for the wave guide nature of Müller cells. Those discrepancies can be most likely attributed to the different coupling conditions between the used setups. In contrast to cells in a tissue, each Müller cell in the experiment from Franze et al. (2007) was previously aligned by optical forces, so that the axes of the fibers and the cell were perfectly congruent. Before a measurement started every Müller cell was brought in contact with the fiber cores. In addition, the artificial surrounding probably increased the numerical aperture of the Müller cell, i.e. the numerical aperture NA_2. Most likely, this experimental procedure drastically reduced many of the above described losses so that the coupling efficiency was improved. Based on the collected data, the relative light guiding efficiency of Müller cells is presumably between 1.36 and 1.90.

Altogether, coupling of light into Müller cells is sensitive to the same sources known from losses in glass fiber connectors. Even if losses can be substantially diminished, they cannot be completely avoided, thus the coupling between two fibers remains susceptible to disruptions. In other words, this analogy in the coupling behavior further supports that Müller cells within their natural surrounding experience the appropriate conditions to operate on the principle of light guidance.

5.4 Significance for Vertebrate Vision

So far, my studies primarily focused on the light guiding capability of individual Müller cells embedded within the vital retina. This new finding led to the emerging question whether and how the light that is guided through the array of all Müller cells affects visual perception in vertebrates. Thus, an investigation of the illumination pattern at the level of the light-sensitive photoreceptor mosaic evolved as an additional item of the present work. In principle, the idea was experimentally realized by scanning a tiny light source along the retinal surface and a simultaneous recording of the respective light transmission which step-by-step contributes to an overall transmission image. In fiber experiments only the maximum intensity of the transmitted light behind a single Müller cell significantly changed whereas the total transmitted light intensity remained nearly unaffected (Figures 4.15 and 4.18). To describe it differently, light guided through individual glial cells experiences a redistribution. Despite such an unambiguous result, only an analysis of the interaction between at least two neighbor cells could answer the question if light gets non-uniformly spread throughout the receptor cells. In fact, a close neighbor analysis revealed that Müller cells are appropriately spaced to sustain an inhomogeneous distribution of light behind the retinal tissue (Figure 4.22). And indeed, a direct measurement of laser light entering the photoreceptor segments finally provided clear evidence that the illumination pattern, i.e. the actual visual stimuli of photoreceptors, is predetermined by the array of Müller glial cells (Figures 4.24 and 4.25).

In optics, a common method to determine the quality of an imaging system is to evaluate its limit of resolution (Hecht, 2002). As introduced in section 2.2.2, an object can be considered as a composition of point sources whereas each point is imaged as an individual point spread function (Figures 2.10, c and d). Accordingly, a fundamental description of the final intensity distribution resulting from all Airy patterns is given by the modulation transfer function (Bergmann and Schaefer, 1998; Hecht, 2002). With respect to the eye, it describes how reliable the details from an object, i.e. the spatial frequency of the point sources constituting the object, are transferred to the image arriving at the photoreceptor segments (Figure 5.9 a). One can imagine, the finer the details the lower the contrast of the image. Figure 5.9 (b) illustrates the modulation transfer functions of three types of species, measured by Artal et al. (1998). Without doubt there are considerable differences between the recorded curves for rodents and man. The graph for the human retina covers a broad range while the modulation transfer function of mouse and rat already falls off, especially the frequency where the modulation becomes zero is some order of magnitudes lower than for human ($\nu_\mathrm{h} > \nu_\mathrm{m}, \nu_\mathrm{r}$). This so-called cutoff frequency ν_co describes the limit of resolution caused by diffraction of light, also known as Rayleigh criterion (Figure 2.10 f).

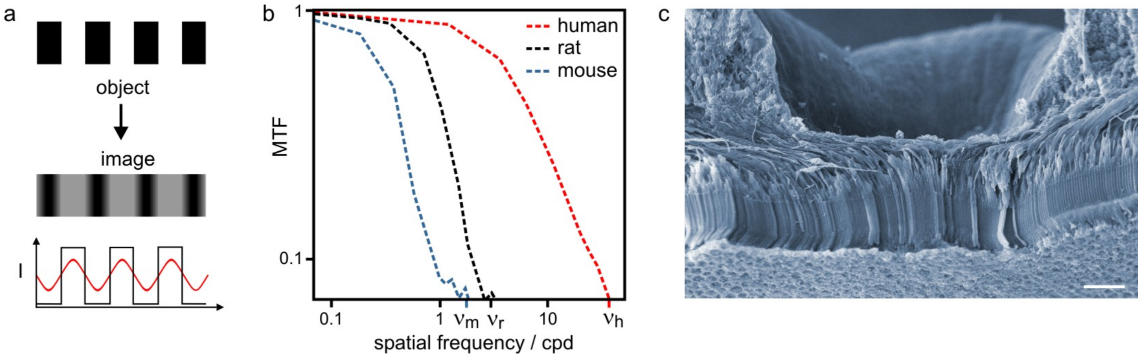

Figure 5.9: Contrast vision in vertebrates. (a) A high contrast object, represented by a regular intensity profile (black), passes an optical system and reveals a lower contrast image whose intensity appears as sinusoidal profile (red). (I, intensity) (b) Modulation transfer function (MTF) on logarithmic scales for mouse (blue), rat (black) and human (red) observers. Image modified from Artal et al. (1998). (c) Scanning electron micrograph of a fovea of a macaque monkey (Macaca fascicularis). Scale bar 100 µm. Image courtesy of J. Kacza.

From an optical point of view, the excellent image quality of man is based on a surprisingly simple principle. High acuity vision of humans and other primates is mediated by the cup shaped fovea centralis, a small central spot within the retina whose bottom is lined by densely packed cone receptors (Figure 5.9 c). In contrast to the conventional morphology of the inverted retina, photoreceptors are not obscured by any cellular structure (Rodieck, 1973; Pettigrew et al., 1986). Thus, light reaches the receptor cells without being scattered, i.e. without producing considerable noise. A direct consequence of this phenomenon is a high signal-to-noise ratio according to equation 2.28. Since a fovea can only be found in human and monkey eyes, its formation seems to demand an immense effort allowing specific skills that require extreme sharp vision, e.g. the use of tools which is exclusively reserved for primates. The unique design of the foveal pit additionally highlights the disadvantages of a retinal inversion as it impressively reflects the perturbing scattering behavior of the retina (see section 5.2). It also depicts that the resolution for animals without a fovea is not only limited by the eye's optical apparatus as described in section 2.2.2, but also depends on the retinal tissue in front of the receptors. Taking this into account, it seems to be worth to spend energy into a specific optical arrangement of cellular structures within the retina (see section 5.3.1). But despite the benefits of a fovea, the inverted retina is the common cellular construction the vision of vertebrates is generally based on. Actually, the fovea of primates only covers a tiny central area of about 0.5 - 1 mm in diameter. Apparently, it is rather favorable to equip the tissue with light guiding elements such as Müller glial cells, even if their impact on the scattering reduction is less pronounced. The new finding that light guidance of Müller cells undoubtfully increases the signal-to-noise ratio of the illumination pattern at the level of the receptor cells reinforces this statement.

Particularly, the fact that Müller cells and cones are arranged in series emphasize the importance of Müller cell light guidance in visual perception (section 4.8). This close co-alignment explains why an early morphological study from Police (1932) even misinterpreted Müller cells as elongated parts of cones cells. Only recently, it was discovered that Müller glial cells promote a rapid recycling of the cone chromophores and thus play a decisive role in the cone-specific visual cycle (Wang et al., 2009; Wang and Kefalov, 2011). Altogether, both cell types interact in a complex manner including biochemical, morphological and optical processes, the latter is illustrated in Figure 5.10 (a). Müller cells determine the projection of light onto the sensitive photoreceptor segments whereas all receptors belonging to the region of space, supplied with light guided through a single glia cell, are defined as so-called 'receptor field' (Agte et al., 2011). Figures 4.23 and 4.24 in conjunction with the morphological data, obtained from cones in Figure 4.27, indicate that each receptor field in guinea pig retina is composed of 1 cone and around 10 - 12 rod cells. This number coincides with the number of photoreceptors statistically belonging to one Müller cell in many mammalian retinae such as human (outside the fovea centralis), rabbit and others (Reichenbach and Robinson, 1995; Reichenbach and Bringmann, 2010). Interestingly, even if the number of rod cells increases, e.g. for animals with a nocturnal lifestyle, the densities of Müller cells and cone photoreceptor cells are usually almost identical. Consequently, a Müller cell guides the light to its receptor fields consisting of 1 cone and a species-specific number of rod photoreceptor cells. As already mentioned, a cone is not randomly positioned within the receptor field but rather occupies the central region directly behind a Müller cell, in other words, it receives the maximum intensity of light (Figures 4.15 and 4.28). Accordingly, Figures 5.10 (b) and (c) show the receptor mosaic in a vital preparation of the retina and the corresponding two-dimensional projection of light.

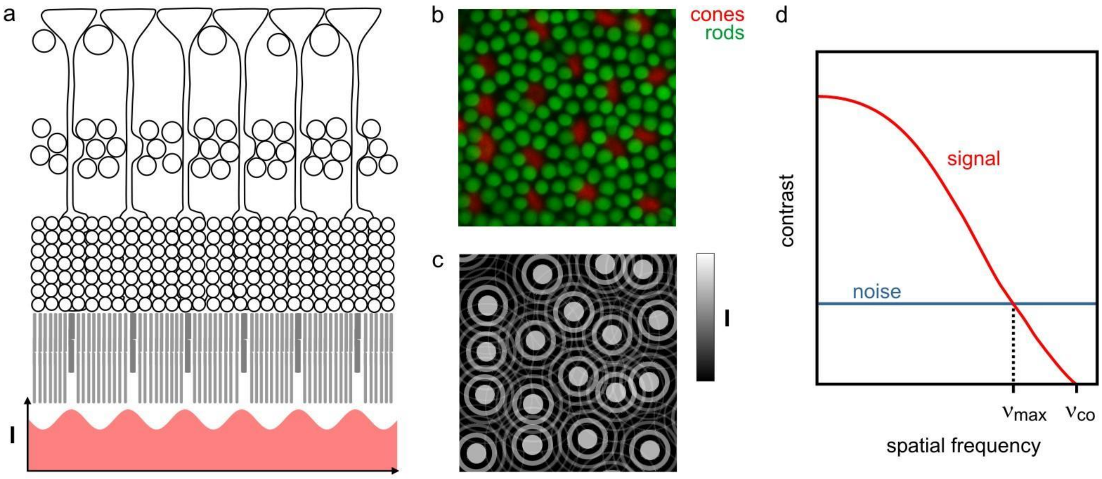

Figure 5.10: Müller cells increase the signal-to-noise ratio. (a) The array of Müller cells predetermines the actual visual stimuli of photoreceptors thereby each Müller cell delivers light to its own 'receptor field'. Below: Intensity distribution (I) at the receptor cells. (b, c) Confocal image of the hexagonal array of fluorescent labeled photoreceptor segments (green: rods, red: cones) and the corresponding illumination pattern. Cones receive the maximum intensity of light due to their favorable positioning behind the light guiding Müller cells. (d) Contrast loss due to noise. The maximum spatial frequency ν_{max} detectable by the eye corresponds to the spatial frequency at which signal (red curve) and noise (blue curve) are equal. (ν_{co}, cutoff frequency) Images adapted from Land and Nilsson (2002) and Warrant (1999).

What does this mean for vertebrate vision and what is the benefit behind? To find an explanation, I have to refer back to section 2.2.2 that already introduced the principal functions of retinal receptor cells. As shown in Figure 2.10 (e), cones are responsible for high acuity photopic vision, i.e. high spatial and temporal resolution under bright light conditions, which nicely illustrates why the primate fovea as the area with the highest density of cone cells provides the sharpest and most detailed information than anywhere else in the retina. Thinking of cones as separate detector channels, a scattering object in front of them would provoke remarkable crosstalk. The optical signal predetermined for a single cone channel would be scattered and finally would be spread across numerous detectors. Thus, each channel would receive tremendous background noise leading to a reduction of visual acuity, demonstrated by the contrast transfer function as shown in

Figure 5.10 (d) (Land and Nilsson, 2002). Graphically, the presence of noise is accompanied by raising the baseline of the diagram, so that the maximum detectable spatial frequency is limited to a fraction of the cutoff. This in turn limits the minimum detectable contrast corresponding to the value where the signal curve crosses the noise line (Warrant, 1999). Considering what happens to the contrast function if light passes a scattering tissue in front of the light detecting cones, it is useful to endow each cone photoreceptor cell with a private wave guide that confines the incoming light to a certain volume and thus prevents it from diverging (Figure 4.14). This would reduce the noise level and additionally enhance the light intensity, i.e. the optical signal per cone cell. Consequently, the signal-to-noise ratio will increase what finally improves contrast vision.

However, it should be remembered that the Müller cell specific receptor field primarily contains rod cells lying closely side by side around the central cone (Figure 5.10 b). As shown in Figure 4.25, the light intensity received by single rods remarkably increased only within specific areas whose dimensions are equivalent to the size of Müller cells. It can be assumed that the chosen rod cells presumably belong to different receptor fields. Further evidence for this idea was provided by a recent study of my lab. It could be demonstrated that contrary to the continuous movement of the light source along the vitreous surface, the field of illuminated photoreceptors frequently changed in jumps (Agte et al., 2011). As summarized in section 2.2.2, the rod system is extremely sensitive allowing to respond even to small amounts of light under dim and dark light conditions (Figure 2.10 b). Thus, scotopic vision mediated by rod cells is of particular importance for vertebrates with a crepuscular or nocturnal lifestyle. An intriguing discovery was made in 1942, Hecht et al. (1942) found that the absorption of only a single photon is sufficent to excite individual rod photoreceptor cells. Nevertheless, one must keep in mind that the visual cortex requires the input of several rod cells while each of them has to be excited by more than one photon in order to distinguish the actual signal from noisy flashes, i.e. so-called 'dark light', occurring due to spontaneous rhodopsin activations (Barlow, 1956; Pirenne, 1967). At luminance levels exceeding this threshold but still under scotopic conditions, the perception of contrasts will be enhanced. It is well known that even a dim spot of light within a dark environment allows to distinguish between different shades of grey (Land and Nilsson, 2002). For these circumstances, the Rose-deVries law provides a description of how many photons are required to detect a given contrast (Rose, 1948)

$$C > \frac{1}{\sqrt{N_\mathrm{P}}}. \tag{5.1}$$

It says the minimum detectable contrast C is proportional to the reciprocal of the square root of the intensity corresponding to the number of photons N_P absorbed per receptor cell (Land and Nilsson, 2002). Or expressed in a different manner, the ability of vertebrates to reliably detect visual information remarkably enhances with rising intensity (Figure 5.11 a). This fact emphasizes the positive impact of Müller cells for scotopic vision since a glial cell induced increase of photons falling onto individual photoreceptors raises the probability of photon absorption. Interestingly, mathematical simulations on an array of Müller cells yielded a slightly optimized guiding efficiency for wavelengths between 500 - 600 nm that matches the absorbance spectrum of chromophores in rod photoreceptors and thus presumably contributes to vision in darkness where every photon is essential (compare Figures 3.1 and 5.11 b; Labin and Ribak, 2010). Nevertheless, further work is necessary to experimentally analyze the wavelength dependence of Müller cells within the living tissue.

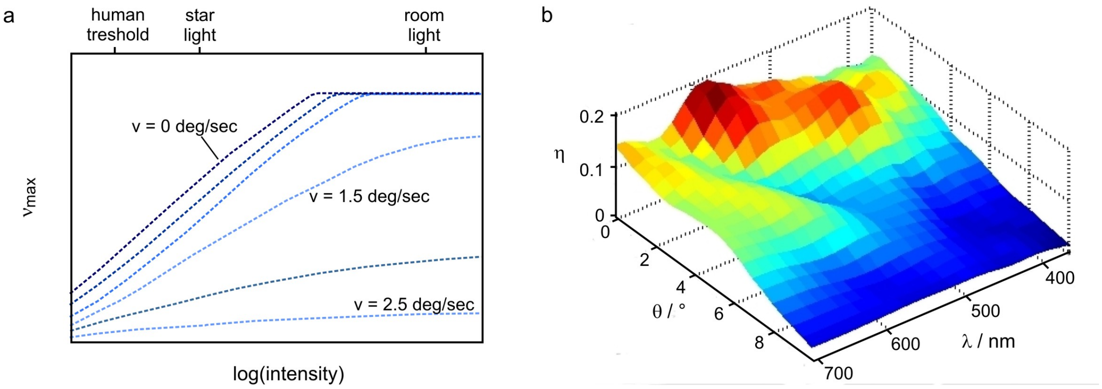

Figure 5.11: Parameters describing the visual performance. (a) The maximum detectable frequency $\nu_{\max}$ increases with improved photon catch. The data are based on an analytical model for the nocturnal toad eye, it was developed to study the visual performance at specified light intensities and image velocities v. (b) Simulation of the light guiding efficiency η of a Müller cell embedded within the retinal tissue for 23 visible wavelength λ and 21 incidence angles θ. Images adapted from Warrant (1999) and Labin and Ribak (2010).

Ultimately, I would like to point out the influence of Müller cells in motion detection since seeing is not a stationary process, instead eyes rather have to deal with permanent fluctuations of light intensities caused by movements of external objects or of the organism itself. Very often, one is not aware that motion is a fundamental source of visual processing in the perception of the environment, but it usually attracts the most attention of the observer. For example, searching for people in a crowd is much easier if the requested person waves the arms in the air. Especially predators have a well-developed ability to recognize even the smallest variations within their field of view explaining nicely why prey animals such as deers remain thoroughly quiet in emerging danger. In principle, every moving object produces quickly changing images projected onto the retina whereas an increasing picture rate is accompanied by a loss of spatial resolution also known as ‘motion blur' (Figure 5.11 a). This effect occurs due to the finite integration time a receptor cell requires to fully respond to a pulse of light, the response time is limited by the speed of the transduction cascade (Hateren, 1993; Warrant, 1999; Land and Nilsson, 2002). If the image velocity is high, i.e. the duration of the light pulse on a single receptor is short, the photoreceptor is not able to generate a maximum response to the flash of light, in other words, the image gets blurred. Vertebrate animals developed a simple but effective way to diminish those artefacts. Contrary to invertebrates, they are able to move their eyes which allows them to follow objects in motion. Such a tracking reduces the relative velocity between object and eye and thus increases the duration of visual stimulation (Eckert and Buchsbaum, 1993; Warrant, 1999; Burr and Morrone, 2011). Another strategy to prolong the stimulation time takes place on a cellular level, namely by broadening the receptor's field of view due to an increased acceptance angle on the basis of its light guiding capability (Land and Nilsson, 2002). One can imagine, the larger the area of photon catch the longer the light stimuli is present. However, this way to improve the temporal resolution is achieved at the expense of spatial resolution, especially if a sufficient signal-to-noise ratio is not a matter of course in view of the scattering tissue layers in front of the receptor cells. Therefore, Müller cells help to sustain the acceptance range of photoreceptors and contribute to tolerate higher image velocities without motion blur. Future approaches should address a direct measurement of the acceptance angle of Müller cells, in particular, the wide endfoot needs to be analyzed regarding its function as entrance structure.

In conclusion, the array of Müller cells represents an important part of the optical construction in front of the light-sensitive receptor cells supporting the visual performance of the rod and the cone system in vertebrate vision.

6 Conclusion

The present thesis provides the evidence that Müller glial cells are living light fibers within the vital retinal tissue. To clearly assign this light guiding capability to the Müller cells, a simultaneous monitoring of multiple parameters was required. Those parameters are the imaging of all retinal layers together with a precise localization of the light entering the tissue, its propagation throughout the varying cellular structures and its arrival at the sensory receptor cells. The newly established fiber setup fulfills all these requirements and offers a comprehensive set of data constituting the basis for a detailed evaluation. In contrast to approaches focusing on a more limited selection of parameters, the established experimental procedure is less susceptible to misinterpretations and provides a higher reliability and explanatory power.

For the first time the natural path of light through the inverted construction of the vital retina from the vitreous surface up to the outer photoreceptor segments could be visualized. Earlier studies were limited to only a part of the light path. They were either based on measurements or theoretical simulations on single cells or certain cellular regions. To achieve a broad impression about the optics of the entire retinal structure, all observations obtained in this thesis were put in context with those from previous publications. Figure 6.1 summarizes all available data to an overall picture which fundamentally contributes to the understanding of how light propagates through the retina of vertebrates. After passing the eye's optical apparatus the light initially enters the retinal tissue via the smooth Müller cell endfoot before it is guided through the thick process of the glia cell (Agte et al., 2011). Subsequently, stacks of consecutive rod photoreceptor nuclei focus the light onto the segments of a single cone and a species-specific number of rod cells (Solovei et al., 2009; Agte et al., 2011). The wave guiding function of the inner and outer receptor segments finally transports the light towards the light-sensitive pigments (Enoch, 1963). The schema in Figure 6.1 highlights the particular significance of Müller cells in preventing the scattering of light, most likely evoked by the structures within the two plexiform layers. Hence, Müller cells carry out a major task in retina optics and represent the missing link to understand how light reaches the receptor cells.

In addition, Figure 6.1 emphasizes another central item of the present work - the optical function of the retinal tissue in its entirety. Even if the neurons surrounding the Müller cells are not actively involved in the transportation of light, their optical impact plays a decisive role in maintaining the required refractive index gradient for light guidance. Interestingly, a general concept in glia research is that a central Müller cell and its neighboring neurons represent the smallest functional unit of the retinal tissue (Reichenbach and Robinson, 1995). As shown in this thesis, also the image quality arriving at the receptor cells and thus the optical task of the retina can be attributed to the interplay between a large number of such repetitive columnar units. This finding allows to elaborate a comprehensive theory how Müller cell light guidance as central element of retina optics improves the visual perception of vertebrates. In summary, the present work offers profound insights into the long-standing paradoxon arising from the contradiction between the well-developed vision of vertebrates and the unfavorable construction of their retinal tissue. The inverted retina represents a sophisticated optical system that demonstrates how nature compensates for disadvantages resulting from an inversion. From this perspective, retina optics can be considered an evolutionary benefit.

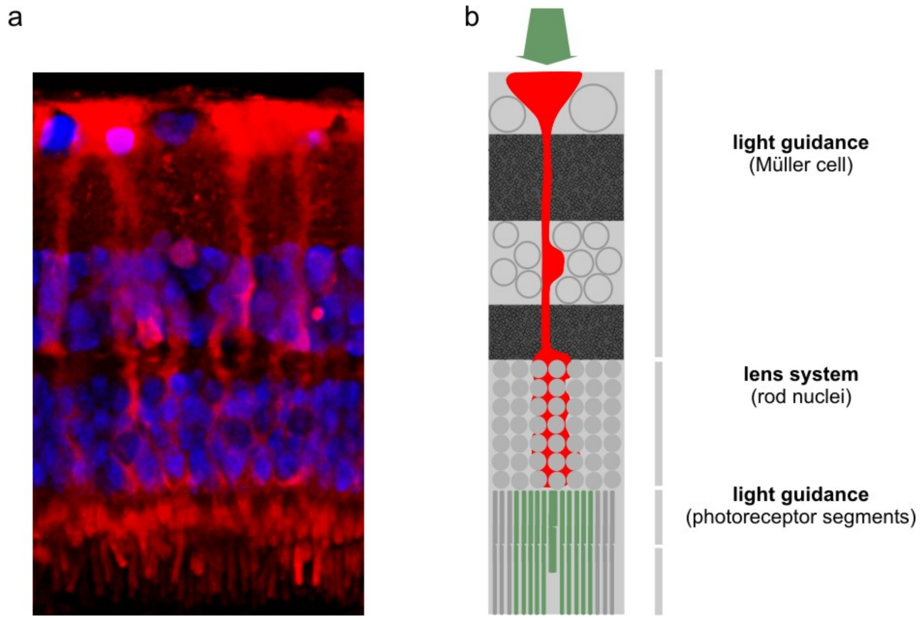

Figure 6.1: Retina optics. (a) Confocal image of a guinea pig retina. (red, Müller cells and photoreceptor segments; blue, nuclei of neurons) (b) Pathway of light within the inverted vertebrate retina. The Müller cell guides the incoming light (green) through the scattering tissue which obscures the photoreceptor cells. In particular, the two plexiform layers consist of numerous strong scatterers (dark grey). Finally, a lens system of rod nuclei focuses the light onto the light guiding segments of 1 cone and a species-specific number of rod cells (around 10 for guinea pig). (Enoch, 1961, Enoch, 1963, Franze et al., 2007, Solovei et al., 2009 and Agte et al., 2011).

Furthermore, this work addresses the more global issue of how morphological structures of cells embedded within their natural environment influence the interaction with light. The current lack of knowledge regarding the behavior of light within living biological tissues is a limiting factor in microscopy and for optical diagnostic methods. A better understanding of the relationship between cell structure and light scattering will enhance the accurate assessment of obtained data.

In spite of all new findings still more work has to be done to answer remaining open questions. It is not yet solved on which specific structures the principle of light guidance within Müller cells is generally based. For this purpose, the spatial resolution of the method has to be improved to specifically characterize the scattering behavior of the intracellular structures, including the dependency on parameters like wavelength and intensity. Also a biochemical change of the concentration or an induced functional and structural disorder of organelles like the aligned intermediate filaments within Müller cells could help to understand the underlying mechanism. Moreover, prospective studies are necessary to develop new sophisticated techniques in order to reliably measure the refractive index distribution within living biological tissues. Also, learning more about the interplay of all elements participating in retina optics, shown in Figure 6.1, should be another goal of future experiments. From a physical perspective, the transition of light between the different optical systems needs to come into the focus of further approaches.

“There is grandeur in this view of life, with its several powers, having been originally breathed into a few forms or into one; and that, whilst this planet has gone cycling on according to the fixed law of gravity, from so simple a beginning endless forms most beautiful and most wonderful have been, and are being, evolved.”

(Last sentence from Darwin’s “The Origin of Species”; Darwin, 1859)

Bibliography

Agte, S., S. Junek, S. Matthias, E. Ulbricht, I. Erdmann, A. Wurm, D. Schild, J. A. Käs, and A. Reichenbach (2011). Müller glial cell-provided cellular light guidance through the vital guinea-pig retina. *Biophysical Journal*, 101(11), 2611–2619.

Ajo, A. (1947). On the refractive index of the retina. *Acta Physiologica Scandinavica*, 13(1-2), 130–149.

Alberts, B., A. Johnson, J. Lewis, M. Raff, K. Roberts, and P. Walter (2002). Molecular biology of the cell. New York: Garland Science.

Artal, P., P. d. Herreros Tejada, C. Muñoz Tedó, and D. G. Green (1998). Retinal image quality in the rodent eye. *Visual Neuroscience*, 15(4), 597–605.

Barer, R. (1957). Refractometry and interferometry of living cells. *Journal of the Optical Society of America*, 47(6), 545–556.

Barlow, H. B. (1956). Retinal noise and absolute threshold. *Journal of the Optical Society of America*, 46(8), 634–639.

Bass, M. (1995). Volume I: fundamentals, techniques, and design. USA: McGraw-Hill.

Baylor, D. A. and R. Fettiplace (1975). Light path and photon capture in turtle photoreceptors. *The Journal of Physiology*, 248(2), 433–464.

Beauvoit, B. and B. Chance (1998). Time-resolved spectroscopy of mitochondria, cells and tissues under normal and pathological conditions. *Molecular and Cellular Biochemistry*, 184(1-2), 445–455.

Beauvoit, B., T. Kitai, and B. Chance (1994). Contribution of the mitochondrial compartment to the optical properties of the rat liver: a theoretical and practical approach. *Biophysical Journal*, 67(6), 2501–2510.

Beauvoit, B., S. M. Evans, T. W. Jenkins, E. E. Miller, and B. Chance (1995). Correlation between the light scattering and the mitochondrial content of normal tissues and transplantable rodent tumors. *Analytical Biochemistry*, 226(1), 167–174.

Bennett, A. H., H. Osterburg, H. Jupnitz, and O. W. Richards (1951). Phase microscopy: Principles and applications. New York: Wiley.

Bergmann, L. and C. Schaefer (1998). Optics of waves and particles. Berlin: Walter de Gruyter.

Beuthan, J., O. Minet, J. Helfmann, M. Herrig, and G. Müller (1996). The spatial variation of the refractive index in biological cells. *Physics in Medicine and Biology*, 41(3), 369–382.

Boehm, G. (1940). Über ein neues entoptisches Phänomen im polarisierten Licht. »Periphere« Polarisationsbüschel. *Acta Ophthalmologica*, 18(2), 143–169.

Bohren, C. F. and D. R. Huffman (1983). Absorption and scattering of light by small particles. New York: Wiley.

Bolin, F. P., L. E. Preuss, R. C. Taylor, and R. J. Ference (1989). Refractive index of some mammalian tissues using a fiber optic cladding method. *Applied Optics*, 28(12), 2297–2303.

Boucher, F., R. M. Leblanc, S. Savage, and B. Beaulieu (1986). Depth-resolved chromophore analysis of bovine retina and pigment epithelium by photoacoustic spectroscopy. *Applied Optics*, 25(4), 515.

Bowmaker, J. K. and H. J. Dartnall (1980). Visual pigments of rods and cones in a human retina. *The Journal of Physiology*, 298, 501–511.

Bowmaker, J. K., S. Astell, D. M. Hunt, and J. D. Mollon (1991). Photosensitive and photostable pigments in the retinae of Old World monkeys. *The Journal of Experimental Biology*, 156, 1–19.

Brümmer, F., M. Pfannkuchen, A. Baltz, T. Hauser, and V. Thiel (2008). Light inside sponges. *Journal of Experimental Marine Biology and Ecology*, 367(2), 61–64.

Brunner, C. (2011). Origin and Spatial Distribution of Forces in Motile Cells. PhD thesis. Leipzig: University of Leipzig.

Brunsting, A. and P. F. Mullaney (1974). Differential light scattering from spherical mammalian cells. *Biophysical Journal*, 14(6), 439–453.

Burr, D. C. and M. C. Morrone (2011). Spatiotopic coding and remapping in humans. *Philosophical Transactions of the Royal Society of London. Series B, Biological Sciences*, 366(1564), 504–515.

Buttery, R. G., C. F. Hinrichsen, L. L. Weller, and J. R. Haight (1991). How thick should a retina be? A comparative study of mammalian species with and without intraretinal vasculature. *Vision Research*, 31(2), 169–187.

Castro, G. O. d., H. Martins-Ferreira, and P. F. Gardino (1985). Dual nature of the peaks of light scattered during spreading depression in chick retina. *Anais da Academia Brasileira de Ciências*, 57(1), 95–103.

Charman, W. N. (1980). Reflection of plane-polarized light by the retina. *The British Journal of Physiological Optics*, 34, 34–49.

Chen, E. (1993). Refractive indices of the rat retinal layers. *Ophthalmic Research*, 25(1), 65–68.

Cheong, W., S. Prahl, and A. Welch (1990). A review of the optical properties of biological tissues. *IEEE Journal of Quantum Electronics*, 26(12), 2166–2185.

Choi, S.-Y., B. Borghuis, R. Rea, E. S. Levitan, P. Sterling, and R. H. Kramer (2005a). Encoding Light Intensity by the Cone Photoreceptor Synapse. *Neuron*, 48(4), 555–562.

Choi, S.-Y., S. Zejuan, and R. H. Kramer (2005b). Imaging light-modulated release of synaptic vesicles in the intact retina: Retinal physiology at the dawn of the post-electrode era. *Vision Research*, 45(28), 3487–3495.

Cote, R. H., M. D. Bownds, and V. Y. Arshavsky (1994). cGMP binding sites on photoreceptor phosphodiesterase: role in feedback regulation of visual transduction. *Proceedings of the National Academy of Sciences of the United States of America*, 91(11), 4845–4849.

Darwin, C. (1859). On the origin of species by means of natural selection, or, the preservation of favoured races in the struggle for life. London: John Murray.

Deeg, C. A., D. Pompetzki, A. J. Raith, S. M. Hauck, B. Amann, S. Suppmann, T. W. F. Goebel, U. Olazabal, H. Gerhards, S. Reese, M. Stangassinger, B. Kaspers, and M.

Ueffing (2006). Identification and functional validation of novel autoantigens in equine uveitis. *Molecular & Cellular Proteomics*, 5(8), 1462–1470.

Di Francia, G. T. (1949). The radiation pattern of retinal receptors. *Proceedings of the Physical Society. Section B*, 62(7), 461–462.

Dirckx, J. J., L. C. Kuypers, and W. F. Decraemer (2005). Refractive index of tissue measured with confocal microscopy. *Journal of Biomedical Optics*, 10(4), 44014.

Dreher, Z., S. R. Robinson, and C. Distler (1992). Müller cells in vascular and avascular retinae: a survey of seven mammals. *The Journal of Comparative Neuroscience*, 323(1), 59–80.

Drenckhahn, D. and H. J. Wagner (1985). Relation of retinomotor responses and contractile proteins in vertebrate retinas. *European Journal of Cell Biology*, 37, 156–168.

Drezek, R., A. Dunn, and R. Richards-Kortum (1999). Light scattering from cells: finite-difference time-domain simulations and goniometric measurements. *Applied Optics*, 38(16), 3651–3661.

Dunn, A. and R. Richards-Kortum (1996). Three-dimensional computation of light scattering from cells. *IEEE Journal of Selected Topics in Quantum Electronics*, 2(4), 898–905.

Eberhardt, C., B. Amann, A. Feuchtinger, S. M. Hauck, and C. A. Deeg (2011). Differential expression of inwardly rectifying K+ channels and aquaporins 4 and 5 in autoimmune uveitis indicates misbalance in Müller glial cell-dependent ion and water homeostasis. *Glia*, 59(5), 697–707.

Ebrey, T. and Y. Koutalos (2001). Vertebrate photoreceptors. *Progress in Retinal and Eye Research*, 20(1), 49–94.

Eckert, M. P. and G. Buchsbaum (1993). Efficient coding of natural time varying images in the early visual system. *Philosophical Transactions of the Royal Society of London. Series B, Biological Sciences*, 339(1290), 385–395.

Eckmiller, M. S. (2004). Defective cone photoreceptor cytoskeleton, alignment, feedback, and energetics can lead to energy depletion in macular degeneration. *Progress in Retinal and Eye Research*, 23(5), 495–522.

Elshereef, R., H. Budman, C. Moresoli, and R. L. Legge (2010). Probing protein colloidal behavior in membrane-based separation processes using spectrofluorometric Rayleigh scattering data. *Biotechnology Progress*, 26(3), 772–780.

Enoch, J. M. (1963). Optical properties of the retinal receptors. *Journal of the Optical Society of America*, 53(1), 71–85.

Enoch, J. M. (1961). Visualization of wave-guide modes in retinal receptors. *American Journal of Ophthalmology*, 51, 1107–1118.

Enoch, J. M. and L. E. Glisman (1966). Physical and optical changes in excised retinal tissue. Resolution of retinal receptors as a fiber optic bundle. *Investigative Ophthalmology & Visual Science*, 5(2), 208–221.

Enoch, J. M. and F. L. Tobey (1978). Use of the waveguide parameter V to determine the difference in the index of refraction between the rat rod outer segment and the interstitial matrix. *Journal of the Optical Society of America*, 68(8), 1130–1134.

Enoch, J. M., F. L. Tobey, and H. E. Bedell (1981). Vertebrate photoreceptor optics. Berlin and New York: Springer.

Faude, F., S. Wendt, B. Biedermann, U. Gärtner, J. Kacza, J. Seeger, A. Reichenbach, and P. Wiedemann (2001). Facilitation of artificial retinal detachment for macular translocation surgery tested in rabbit. *Investigative Ophthalmology & Visual Science*, 42(6), 1328–1337.

Flock, S. T., B. C. Wilson, and M. S. Patterson (1987). Total attenuation coefficients and scattering phase functions of tissues and phantom materials at 633 nm. *Medical Physics*, 14(5), 835–841.

Franze, K., J. Grosche, S. N. Skatchkov, S. Schinkinger, C. Foja, D. Schild, O. Uckermann, K. Travis, A. Reichenbach, and J. Guck (2007). Müller cells are living optical fibers in the vertebrate retina. *Proceedings of the National Academy of Sciences of the United States of America*, 104(20), 8287–8292.

Franze, K. (2007). Mechanical and Optical Properties of Nervous Tissue and Cells. PhD thesis. Leipzig: University of Leipzig.

Germer, A., B. Biedermann, H. Wolburg, J. Schuck, J. Grosche, H. Kuhrt, W. Reichelt, A. Schousboe, G. Paasche, A. F. Mack, and A. Reichenbach (1998). Distribution of mitochondria within Müller cells — I. Correlation with retinal vascularization in different mammalian species. *Journal of Neurocytology*, 27(5), 329–345.

Glaser, A. N. (2001). High-yield biostatistics. Philadelphia: Lippincott Williams & Wilkins.

Goldsmith, T. H. (1990). Optimization, constraint, and history in the evolution of eyes. *The Quarterly Review of Biology*, 65(3), 281–322.

Gorrand, J. M. (1986). Separation of the reflection by the inner limiting membrane. *Ophthalmic & Physiological Optics*, 6(2), 187–196.

Gouras, P. (1958). Spreading depression of activity in amphibian retina. *The American Journal of Physiology*, 195(1), 28–32.

Grosser, S. (2011). Validity of the Ray Optics Model for the Passage of Light through Biological Cells. PhD thesis. Leipzig: Universität Leipzig.

Guck, J., R. Ananthakrishnan, H. Mahmood, T. J. Moon, C. C. Cunningham, and J. Käs (2001). The optical stretcher: a novel laser tool to micromanipulate cells. *Biophysical Journal*, 81(2), 767–784.

Hammer, M., A. Roggan, D. Schweitzer, and G. Müller (1995). Optical properties of ocular fundus tissues–an in vitro study using the double-integrating-sphere technique and inverse Monte Carlo simulation. *Physics in Medicine and Biology*, 40(6), 963–978.

Hateren, J. H. van (1993). Spatiotemporal contrast sensitivity of early vision. *Vision Research*, 33(2), 257–267.

Hecht, E. (2002). Optics. Amsterdam: Addison-Wesley.

Hecht, S., S. Shlaer, and M. H. Pirenne (1942). Energy, quanta, and vision. *The Journal of General Physiology*, 25(6), 819–840.

Helfand, B. T., L. Chang, and R. D. Goldman (2004). Intermediate filaments are dynamic and motile elements of cellular architecture. *Journal of Cell Science*, 117(Pt 2), 133–141.

Hestrin, S. and J. I. Korenbrot (1990). Activation kinetics of retinal cones and rods: response to intense flashes of light. *The Journal of Neuroscience*, 10(6), 1967–1973.

Hielscher, A. H., J. R. Mourant, and I. J. Bigio (1997). Influence of particle size and concentration on the diffuse backscattering of polarized light from tissue phantoms and biological cell suspensions. *Applied Optics*, 36(1), 125–135.

Hoang, Q. V., R. A. Linsenmeier, C. K. Chung, and C. A. Curcio (2002). Photoreceptor inner segments in monkey and human retina: mitochondrial density, optics, and regional variation. *Visual Neuroscience*, 19(4), 395–407.

Hollis, V. S. (2002). Non-Invasive Monitoring of Brain Tissue Temperature by Near-Infrared Spectroscopy. PhD thesis. London: University of London.

Hoppe, W., W. Lohmann, H. Markl, and H. Ziegler (1982). Biophysik. Berlin: Springer.

Hulst, H. C. van de (1981). Light scattering by small particles. New York: Dover Publications.

Jackson, J. D. (1999). Classical electrodynamics. New York: Wiley.

Kandel, E. J., J. H. Schwartz, and T. M. Jessell (1999). Principles of neural science. New York: McGraw-Hill Companies.

Karl, A., A. Wurm, T. Pannicke, K. Krügel, M. Obara-Michlewska, P. Wiedemann, A. Reichenbach, J. Albrecht, and A. Bringmann (2011). Synergistic action of hypoosmolarity and glutamine in inducing acute swelling of retinal glial (Müller) cells. *Glia*, 59(2), 256–266.

Kennedy, B. and J. Malicki (2009). What drives cell morphogenesis: a look inside the vertebrate photoreceptor. *Developmental Dynamics*, 238(9), 2115–2138.

Knabe, W., S. Skatchkov, and H. J. Kuhn (1997). "Lens mitochondria" in the retinal cones of the tree-shrew tupaia belangeri. *Vision Research*, 37(3), 267–271.

Knighton, R. W. and X. R. Huang (1999). Directional and spectral reflectance of the rat retinal nerve fiber layer. *Investigative Ophthalmology & Visual Science*, 40(3), 639–647.

Knighton, R. W., C. Baverez, and A. Bhattacharya (1992). The directional reflectance of the retinal nerve fiber layer of the toad. *Investigative Ophthalmology & Visual Science*, 33(9), 2603–2611.

Knighton, R. W., S. G. Jacobson, and C. M. Kemp (1989). The spectral reflectance of the nerve fiber layer of the macaque retina. *Investigative Ophthalmology & Visual Science*, 30(11), 2392–2402.

Knüttel, A., S. Bonev, and W. Knaak (2004). New method for evaluation of in vivo scattering and refractive index properties obtained with optical coherence tomography. *Journal of Biomedical Optics*, 9(2), 265–273.

Ko, T. H., J. G. Fujimoto, J. S. Duker, L. A. Paunescu, W. Drexler, C. R. Baumal, C. A. Puliafito, E. Reichel, A. H. Rogers, and J. S. Schuman (2004). Comparison of ultrahigh- and standard-resolution optical coherence tomography for imaging macular hole pathology and repair. *Ophthalmology*, 111(11), 2033–2043.

Kopp, G. and J. L. Lean (2011). A new, lower value of total solar irradiance: evidence and climate significance. *Geophysical Research Letters*, 38, L01706.

Kreplak, L. and D. Fudge (2007). Biomechanical properties of intermediate filaments: from tissues to single filaments and back. *BioEssays*, 29(1), 26–35.

Kreysing, M., L. Boyde, J. Guck, and K. J. Chalut (2010). Physical insight into light scattering by photoreceptor cell nuclei. *Optics Letters*, 35(15), 2639–2641.

Krishnamoorthy, V., J. Varsha, C. Pitchaiah, B. Sonia, and D. K. Narender (2008). Intravitreal injection of fluorochrome-conjugated peanut agglutinin results in specific and reversible labeling of mammalian cones in vivo. *Investigative Ophthalmology & Visual Science*, 49(6), 2643–2650.

Labin, A. M. and E. N. Ribak (2010). Retinal glial cells enhance human vision acuity. *Physical Review Letters*, 104(15), 158102.

Land, M. F. and D.-E. Nilsson (2002). Animal eyes. New York: Oxford University Press.

Lehninger, A., M. M. Cox, and D. L. Nelson (2008). Lehninger principles of biochemistry. New York: W. H. Freeman.

Li, Y., L. A. Holtzclaw, and J. T. Russell (2001). Müller cell Ca2+ waves evoked by purinergic receptor agonists in slices of rat retina. *Journal of Neurophysiology*, 85(2), 986–994.

Liu, H., B. Beauvoit, M. Kimura, and B. Chance (1996). Dependence of tissue optical properties on solute-induced changes in refractive index and osmolarity. *Journal of Biomedical Optics*, 1(2), 200–211.

Lodish, H. F., A. Berk, C. A. Kaiser, M. Krieger, A. Bretscher, H. Ploegh, A. Amon, and M. P. Scott (2000). Molecular cell biology. New York: W. H. Freeman.

Loncar, D., B. A. Afzelius, and B. Cannon (1988). Epididymal white adipose tissue after cold stress in rats. I. Nonmitochondrial changes. *Journal of Ultrastructure and Molecular Structure Research*, 101(2-3), 109–122.

Loud, A. V. (1968). A quantitative stereological description of the ultrastructure of normal rat liver parenchymal cells. *The Journal of Cell Biology*, 37(1), 27–46.

Lu, Y.-B, I. Iandiev, M. Hollborn, N. Körber, E. Ulbricht, P. G. Hirrlinger, T. Pannicke, E.-Q Wei, A. Bringmann, H. Wolburg, U. Wilhelmsson, M. Pekny, P. Wiedemann, A. Reichenbach, and J. A. Käs (2011). Reactive glial cells: increased stiffness correlates with increased intermediate filament expression. *The FASEB Journal*, 25(2), 624–631.

Lu, Y.-B., K. Franze, G. Seifert, C. Steinhäuser, F. Kirchhoff, H. Wolburg, J. Guck, P. Janmey, E.-Q. Wei, J. Käs, and A. Reichenbach (2006). Viscoelastic Properties of individual glial cells and neurons in the CNS. *Proceedings of the National Academy of Sciences of the United States of America*, 103(47), 17759–17764.

Marina, O. C., C. K. Sanders, and J. R. Mourant (2012). Correlating light scattering with internal cellular structures. *Biomedical Optics Express*, 3(2), 296–312.

Martins-Ferreira, H. and G. O. d. Castro (1966). Light-scattering changes accompanying spreading depression in isolated retina. *Journal of Neurophysiology*, 29(4), 715–726.

Masland, R. H. (2001). The fundamental plan of the retina. *Nature Neuroscience*, 4(9), 877–886.

Mie, G. (1908). Beiträge zur Optik trüber Medien, speziell kolloidaler Metallösungen. *Annalen der Physik*, 330(3), 377–445.

Miller, J. L. and J. I. Korenbrot (1994). Differences in calcium homeostasis between retinal rod and cone photoreceptors revealed by the effects of voltage on the cGMP-gated conductance in intact cells. *The Journal of General Physiology*, 104(5), 909–940.

Miller, W. H. and A. W. Snyder (1973). Optical function of human peripheral cones. *Vision Research*, 13(12), 2185–2194.

Miller, W. H. and A. W. Snyder (1972). Optical function of myoids. *Vision Research*, 12(11), 1841–1848.

Moores, C. A., M. Perderiset, C. Kappeler, S. Kain, D. Drummond, S. J. Perkins, J. Chelly, R. Cross, A. Houdusse, and F. Francis (2006). Distinct roles of doublecortin modulating the microtubule cytoskeleton. *The EMBO Journal*, 25(19), 4448–4457.

Mori, S., W. H. Miller, and T. Tomita (1976). Müller cell function during spreading depression in frog retina. *Proceedings of the National Academy of Sciences of the United States of America*, 73(4), 1351–1354.

Mourant, J. R., T. M. Johnson, V. Doddi, and J. P. Freyer (2002a). Angular dependent light scattering from multicellular spheroids. *Journal of Biomedical Optics*, 7(1), 93–99.

Mourant, J. R., M. Canpolat, C. Brocker, O. Esponda-Ramos, T. M. Johnson, A. Matanock, K. Stetter, and J. P. Freyer (2000). Light scattering from cells: the contribution of the nucleus and the effects of proliferative status. *Journal of Biomedical Optics*, 5(2), 131–137.

Mourant, J. R., J. P. Freyer, A. H. Hielscher, A. A. Eick, D. Shen, and T. M. Johnson (1998). Mechanisms of light scattering from biological cells relevant to noninvasive optical-tissue diagnostics. *Applied Optics*, 37(16), 3586–3593.

Mourant, J. R., T. M. Johnson, S. Carpenter, A. Guerra, T. Aida, and J. P. Freyer (2002b). Polarized angular dependent spectroscopy of epithelial cells and epithelial cell nuclei to determine the size scale of scattering structures. *Journal of Biomedical Optics*, 7(3), 378–387.

Mullaney, P. F. and P. N. Dean (1969). Cell sizing: a small-angle light-scattering method for sizing particles of low relative refractive index. *Applied Optics*, 8(11), 2361–2362.

Müller, H. (1851). Zur Histologie der Netzhaut. *Zeitschrift für Wissenschaft und Zoologie*, 3, 234–237.

Murakami, Y., A. Kawana, and H. Tsuchiya (1979). Cut-off wavelength measurements for single-mode optical fibers. *Applied Optics*, 18(7), 1101–1105.

Newman, E. and A. Reichenbach (1996). The Müller cell: a functional element of the retina. *Trends in Neurosciences*, 19(8), 307–312.

Newman, E. A. (2001). Propagation of intercellular calcium waves in retinal astrocytes and Müller cells. *The Journal of Neuroscience*, 21(7), 2215–2223.

Newman, E. A. (2005). Calcium increases in retinal glial cells evoked by light-induced neuronal activity. *The Journal of Neuroscience*, 25(23), 5502–5510.

Nilsson, A. M., C. Sturesson, D. L. Liu, and S. Andersson-Engels (1998). Changes in spectral shape of tissue optical properties in conjunction with laser-induced thermotherapy. *Applied Optics*, 37(7), 1256–1267.

Niven, J. E. and S. B. Laughlin (2008). Energy limitation as a selective pressure on the evolution of sensory systems. *The Journal of Experimental Biology*, 211(Pt 11), 1792–1804.

Nordenson, J. (1934). Über den Brechungsindex der Netzhaut. *Acta Ophthalmology Copenhagen*, 12, 171–175.

O'Brien, B. (1951). Vision and resolution in the central retina. *Journal of the Optical Society of America*, 41(12), 882–894.

Otori, Y., J. Y. Wei, and C. J. Barnstable (1998). Neurotoxic effects of low doses of glutamate on purified rat retinal ganglion cells. *Investigative Ophthalmology & Visual Science*, 39(6), 972–981.

Owczarek, F. R., G. E. Marak, and R. A. Pilkerton (1975). Retinal adhesion in light- and dark adapted rabbits. *Investigative Ophthalmology*, 14(5), 353–358.

Palade, G. E. (1953). An electron microscope study of the mitochondrial structure. *The Journal of Histochemistry and Cytochemistry*, 1(4), 188–211.

Palanker, D., P. Huie, A. Vankov, R. Aramant, M. Seiler, H. Fishman, M. Marmor, and M. Blumenkranz (2004). Migration of retinal cells through a perforated membrane: implications for a high-resolution prosthesis. *Investigative Ophthalmology & Visual Science*, 45(9), 3266–3270.

Pampaloni, F., G. Lattanzi, A. Jonás, T. Surrey, E. Frey, and E.-L. Florin (2006). Thermal fluctuations of grafted microtubules provide evidence of a length-dependent persistence length. *Proceedings of the National Academy of Sciences of the United States of America*, 103(27), 10248–10253.

Pannicke, T., I. Iandiev, A. Wurm, O. Uckermann, F. Vom Hagen, A. Reichenbach, P. Wiedemann, H.-P. Hammes, and A. Bringmann (2006). Diabetes alters osmotic swelling characteristics and membrane conductance of glial cells in rat retina. *Diabetes*, 55(3), 633–639.

Parry, J. W. and J. K. Bowmaker (2002). Visual pigment coexpression in guinea pig cones: a microspectrophotometric study. *Investigative Ophthalmology & Visual Science*, 43(5), 1662–1665.

Pask, C. and K. F. Barrell (1980). Photoreceptor optics I: introduction to formalism and excitation in a lens-photoreceptor system. *Biological Cybernetics*, 36(1), 1–8.

Pasternack, R. M., J.-Y. Zheng, and N. N. Boustany (2010). Optical scatter changes at the onset of apoptosis are spatially associated with mitochondria. *Journal of Biomedical Optics*, 15(4), 040504.

Pawley, J. B. (2006). Handbook of biological confocal microscopy. New York: Springer.

Pekny, M., C. B. Johansson, C. Eliasson, J. Stakeberg, A. Wallén, T. Perlmann, U. Lendahl, C. Betsholtz, C. H. Berthold, and J. Frisén (1999). Abnormal reaction to central nervous system injury in mice lacking glial fibrillary acidic protein and vimentin. *The Journal of Cell Biology*, 145(3), 503–514.

Pettigrew, J. D., K. J. Sanderson, and W. R Levick (1986). Visual neuroscience. Cambridge: Cambridge University Press.

Pirenne, M. H. (1967). Vision and eye. London: Chapman.

Police, G. (1932). Sull'interpretazione morfological delle fibre radiali nella retina del vertebrati. *Arch. Zool. (Torino)*, 17, 449–493.

Puliafito, C. A., M. R. Hee, C. P. Lin, E. Reichel, J. S. Schuman, J. S. Duker, J. A. Izatt, E. A. Swanson, and J. G. Fujimoto (1995). Imaging of macular diseases with optical coherence tomography. *Ophthalmology*, 102(2), 217–229.

Rea, R., J. Li, A. Dharia, E. S. Levitan, P. Sterling, and R. H. Kramer (2004). Streamlined synaptic vesicle cycle in cone photoreceptor terminals. *Neuron*, 41(5), 755–766, Reichenbach, A. (1989). Organelle-free cytoplasmic volume fraction of rabbit retinal Müller (glial) cells. *Journal für Hirnforschung*, 30(5), 513–516.

Reichenbach, A. and G. Birkenmeyer (1984). Preparation of isolated Müller cells of the mammalian (rabbit) retina. *Zeitschrift für mikroskopisch-anatomische Forschung*, 98(5), 789–792.

Reichenbach, A. and S. Robinson (1995). Phylogenetic constraints on retinal organisation and development. *Progress in Retinal and Eye Research*, 15(1), 139–171.

Reichenbach, A. (2008). Die Wirbeltiernetzhaut - ein merkwürdiges Sinnesorgan. Stuttgart and Leipzig: Hirzel.

Reichenbach, A. (1999). Neuroglia - das andere zelluläre Element im Nervensystem: Die Müllersche Gliazelle. Wessobrunn: SMV.

Reichenbach, A. and A. Bringmann (2010). Müller cells in the healthy and diseased retina. New York and London: Springer.

Reichenbach, A., K. Franze, S. Agte, S. Junek, A. Wurm, J. Grosche, A. Savvinov, J. Guck, and S. N. Skatchkov (2012). Live cells as optical fibers in the vertebrate retina. *Selected topics on optical fiber technology.* Ed. by M. Yasin, H. Arof, and S. W. Harun. Rijeka: InTech, 247–270.

Rillich, K., J. Gentsch, A. Reichenbach, A. Bringmann, and M. Weick (2009). Light stimulation evokes two different calcium responses in Müller cells of the guinea pig retina. *European Journal of Neuroscience*, 29(6), 1165–1176.

Rodieck, R. W. (1973). The vertebrate retina: principles of structure and function. San Francisco: W. H. Freeman.

Rose, A. (1948). The sensitivity performance of the human eye on an absolute scale. *Journal of the Optical Society of America*, 38(2), 196–208.

Saleh, B. E. and M. C. Teich (1991). Fundamentals of photonics. New York: Wiley.

Schmidt, F. E. W. (1999). Development of a Time-Resolved Optical Tomography System for Neonatal Brain Imaging. PhD thesis. London: University of London.

Schmidt, P. K. and G. W. Rayfield (1994). Hyper-Rayleigh light scattering from an aqueous suspension of purple membrane. *Applied Optics*, 33(19), 4286–4292.

Schmitt, J. M. and G. Kumar (1998). Optical scattering properties of soft tissue: a discrete particle model. *Applied Optics*, 37(13), 2788–2797.

Schmitt, J. M. and G. Kumar (1996). Turbulent nature of refractive-index variations in biological tissue. *Optics Letters*, 21(16), 1310–1312.

Seeliger, M. W., S. C. Beck, N. Pereyra-Muñoz, S. Dangel, J.-Y. Tsai, U. F. Luhmann, S. A. van de Pavert, J. Wijnholds, M. Samardzija, A. Wenzel, E. Zrenner, K. Narfström, E. Fahl, N. Tanimoto, N. Acar, and F. Tonagel (2005). In vivo confocal imaging of the retina in animal models using scanning laser ophthalmoscopy. *Vision Research*, 45(28), 3512–3519.

Shaw, G. and K. Weber (1984). The intermediate filament complement of the retina: a comparison between different mammalian species. *European Journal of Cell Biology*, 33(1), 95–104.

Sheppard, C. and D. Shotton (1997). Confocal laser scanning microscopy. Oxford and New York: BIOS Scientific.

Shlaer, S. (1937). The relation between visual acuity and illumination. New York: The Rockefeller University Press.

Sidman, R. L. (1957). The structure and concentration of solids in photoreceptor cells studied by refractometry and interference microscopy. *The Journal of Biophysical and Biochemical Cytology*, 3(1), 15–30.

Silver, F. H. and D. E. Birk (1984). Molecular structure of collagen in solution: comparison of types I, II, III and V. *International Journal of Biological Macromolecules*, 6(3), 125–132.

Snyder, A. W. and J. D. Love (1983). Optical waveguide theory. London and New York: Chapman and Hall.

Solovei, I. and B. Joffe (2010). Inverted nuclear architecture and its development during differentiation of mouse rod photoreceptor cells: a new model to study nuclear architecture. *Genetika*, 46(9), 1159–1163.

Solovei, I., M. Kreysing, C. Lanctôt, S. Kösem, L. Peichl, T. Cremer, J. Guck, and B. Joffe (2009). Nuclear architecture of rod photoreceptor cells adapts to vision in mammalian evolution. *Cell*, 137(2), 356–368.

Srienc, A. I., T. E. Kornfield, A. Mishra, M. A. Burian, and E. A. Newman (2012). Assessment of glial function in the in vivo retina. *Methods in Molecular Biology*, 814, 499–514.

Starosta, M. S. and A. K. Dunn (2009). Three-dimensional computation of focused beam propagation through multiple biological cells. *Optics Express*, 17(15), 12455–12469.

Stratton, J. A. (2007). Electromagnetic theory. New York: Wiley.

Taylor, K. M. and B. L. Anderson (1995). Misalignment losses in fiber optic joints due to angular misalignment for arbitrary energy distribution. *Optical Engineering*, 34(12), 3471–3479.

Tearney, G. J., M. E. Brezinski, J. F. Southern, B. E. Bouma, M. R. Hee, and J. G. Fujimoto (1995). Determination of the refractive index of highly scattering human tissue by optical coherence tomography. *Optics Letters*, 20(21), 2258.

Thiel, F. L. and R. M. Hawk (1976). Optical waveguide cable connection. *Applied Optics*, 15(11), 2785–2791.

Tobey, F. L. and J. M. Enoch (1973). Directionality and waveguide properties of optically isolated rat rods. *Investigative Ophthalmology*, 12(12), 873–880.

Tobey, F. L., J. M. Enoch, and J. H. Scandrett (1975). Experimentally determined optical properties of goldfish cones and rods. *Investigative Ophthalmology*, 14(1), 7–23.

Tsuchiya, H., H. Nakagome, N. Shimizu, and S. Ohara (1977). Double eccentric connectors for optical fibers. *Applied Optics*, 16(5), 1323–1331.

Uckermann, O., L. Vargová, E. Ulbricht, C. Klaus, M. Weick, K. Rillich, P. Wiedemann, A. Reichenbach, E. Syková, and A. Bringmann (2004a). Glutamate-evoked alterations of glial and neuronal cell morphology in the guinea pig retina. *The Journal of Neuroscience*, 24(45), 10149–10158.

Uckermann, O., I. Iandiev, M. Francke, K. Franze, J. Grosche, S. Wolf, L. Kohen, P. Wiedemann, A. Reichenbach, and A. Bringmann (2004b). Selective staining by vital dyes of Müller glial cells in retinal wholemounts. *Glia*, 45(1), 59–66.

Ullmann, J. F., B. A. Moore, S. E. Temple, E. Fernández-Juricic, and S. P. Collin (2012). The retinal wholemount technique: a window to understanding the brain and behaviour. *Brain, Behavior and Evolution*, 79(1), 26–44.

Valentin, G. (1879). Ein Beitrag zur Kenntnis der Brechungsverhältnisse der Thiergewebe. *Pflügers Archiv für die gesamte Physiologie der Menschen und der Tiere*, 19(1), 78–105.

Virchow, R. (1856). Gesammelte Abhandlungen zur wissenschaftlichen Medicin. Thrombose und Embolie. Gefässentzündung und septische Infektion. Frankfurt a. M.: Meidinger.

Vos, J. J. and M. A. Bouman (1964). Contribution of the retina to entoptic scatter. *Journal of the Optical Society of America*, 54, 95–100.

Wang, J.-S. and V. J. Kefalov (2011). The cone-specific visual cycle. *Progress in Retinal and Eye Research*, 30(2), 115–128.

Wang, J.-S., M. E. Estevez, M. C. Cornwall, and V. J. Kefalov (2009). Intra-retinal visual cycle required for rapid and complete cone dark adaptation. *Nature Neuroscience*, 12(3), 295–302.

Wang, M., W. Ma, L. Zhao, R. N. Fariss, and W. T. Wong (2011). Adaptive Müller cell responses to microglial activation mediate neuroprotection and coordinate inflammation in the retina. *Journal of Neuroinflammation*, 8, 173.

Warrant, E. J. (1999). Seeing better at night: life style, eye design and the optimum strategy of spatial and temporal summation. *Vision Research*, 39(9), 1611–1630.

Watson, D., N. Hagen, J. Diver, P. Marchand, and M. Chachisvilis (2004). Elastic light scattering from single cells: orientational dynamics in optical trap. *Biophysical Journal*, 87(2), 1298–1306.

Westheimer, G. (2006). Specifying and controlling the optical image on the human retina. *Progress in Retinal and Eye Research*, 25(1), 19–42.

Wilson, J. D. and T. H. Foster (2007). Characterization of lysosomal contribution to whole-cell light scattering by organelle ablation. *Journal of Biomedical Optics*, 12(3), 030503.

Wilson, J. D. and T. H. Foster (2005). Mie theory interpretations of light scattering from intact cells. *Optics Letters*, 30(18), 2442–2444.

Wilson, J. D., W. J. Cottrell, and T. H. Foster (2007). Index-of-refraction-dependent subcellular light scattering observed with organelle-specific dyes. *Journal of Biomedical Optics*, 12(1), 014010.

Winston, R. and J. M. Enoch (1971). Retinal cone receptor as an ideal light collector. *Journal of the Optical Society of America*, 61(8), 1120–1122.

Wurm, A., T. Pannicke, I. Iandiev, E. Bühner, U.-C. Pietsch, A. Reichenbach, P. Wiedemann, S. Uhlmann, and A. Bringmann (2006). Changes in membrane conductance play a pathogenic role in osmotic glial cell swelling in detached retinas. *The American Journal of Pathology*, 169(6), 1990–1998.

Zee, P. van der, M. E. Essenpreis, and D. T. Delpy (1993). Optical properties of brain tissue. *Photon migration and imaging in random media and tissues.* Ed. by B. Chance and R. R. Alfano. Vol. 1888. USA: Proc. SPIE, 454–465.

Zernike, F. (1955). How I discovered phase contrast. *Science*, 121, 345–349.

Acknowledgements

I would like to thank many kind people for their help. This work would not have been possible without them. First and foremost, I want to thank my supervisors Prof. Andreas Reichenbach and Prof. Josef Käs for giving me the opportunity to work on this interesting project. Thank you for your encouragement, inspiration, guidance and continuous support from the initial to the final level of this thesis.

Furthermore, I have to thank Dr. Stephan Junek for the help with the measurements on the both way imaging setup, Sabrina Matthias for the aid with the fiber experiments and Dr. Elke Ulbricht for helping me with the immunostaining procedures.

Moreover, I am grateful to all my fellow labmates from the Paul-Flechsig Institute and from the Soft Matter Physics department for the invaluable help I received during the past years. Thank you for your permanent willingness to support me with ideas, inspiring discussions and important advices. I would like to acknowledge Thomas Pannicke, Mike Francke, Elke Ulbricht, Petra Hirrlinger, Antje Grosche and Maik Raab for their help to get into the basics of glia research, Bernd Biedermann and Bernd Kohlstrunk for the numerous sophisticated technical solutions and Jens Grosche for the impressive images. A special thanks goes to the neuro group for all the useful suggestions and motivating discussions that strongly supported the progress of my work, in particular Melanie, Lydia, Philipp, Paul, Thomas, Valentina, Tina, Mareike and Wolfram. Once more I want to thank Thomas Pannicke and Valentina Dallacasagrande for the helpful comments while proofreading this manuscript as well as Thomas Fuhs for the valuable hints regarding TeX. Of course, there are many other people who made the last years an unforgettable time just thinking of all the wonderful PWM summer and winter schools, Rotkäppchen come togethers in PFI or the countless table tennis evenings. Thanks to Lysann, Nicole, Annett, Colle, Steffi, Kati, Martina, David, Tobias, Anatol, Steve, Carsten, Jörg, Susi, Franzi, Dan, Sebastian, Roland, Pico, Chris, but also the former members like Claudia, Karla, Florian, Regina, Qing and all the ones I forgot. Thank you for the great working athmosphere, it has been a pleasure to work with you.

I should not forget to extend my acknowledgement to the members of the graduate school InterNeuro for giving me a broad insight into neuroscience from an interdisciplinary perspective and, of course, for the long entertaining evenings in Schrebers Garten.

Moreover, my acknowledgement goes to some collaboration partners for the scientific groundwork and motivating discussions: Dr. K. Franze, Prof. J. Guck, Prof. A. Savvinov and Prof. D. Schild, but especially to Prof. S. N. Skatchkov for his inventive ideas such as the crazy idea that glial cells in the retina are able to guide light.

Furthermore, I am grateful to the people whose indispensable work always keeps the lab running: Claudia Brück, Ms. Jungmann, Elke Westphal, Undine Dietrich and Ms. Krenzlin. Particularly, I want to thank the technicians from the work shop for the professional equipment.

A very special thanks belongs to Christoph for the patience and support during the past years. Thank you for being there for me.

Last but not least, I would like to express my deepest gratitude to my family. Thank you for your love and the faith you always have in me.

Selbstständigkeitserklärung

Hiermit versichere ich, dass die vorliegende Arbeit ohne unzulässige Hilfe und ohne Benutzung anderer als der angegebenen Hilfsmittel angefertigt und dass die aus fremden Quellen direkt oder indirekt übernommenen Gedanken in der Arbeit als solche kenntlich gemacht wurden. Alle Personen, von denen bei der Auswahl und Auswertung des Materials sowie bei der Herstellung des Manuskripts Unterstützungsleistungen erhalten wurden, sind namentlich genannt. Außer den in der Arbeit Genannten waren keine weiteren Personen bei der geistigen Herstellung der vorliegenden Arbeit beteiligt. Insbesondere haben keine Personen von dem Bewerber oder in seinem Auftrag weder unmittelbar noch mittelbar geldwerte Leistungen für Arbeiten erhalten, die im Zusammenhang mit dem Inhalt der vorgelegten Dissertation stehen. Es wird weiterhin versichert, dass die vorgelegte Arbeit weder im Inland noch im Ausland in gleicher oder in ähnlicher Form einer anderen Prüfungsbehörde zum Zwecke einer Promotion oder eines anderen Prüfungsverfahrens vorgelegt und in ihrer Gesamtheit noch nicht veröffentlicht wurde. Es haben keine früheren erfolglosen Promotionsversuche stattgefunden.

Curriculum Vitae

Name	Silke Agte
Geburtstag	24.07.1980
Geburtsort	Halle/Saale

Schulausbildung

1987 - 1991	Grundschule Vatterode
1991 - 1999	Gymnasium Am Markt, Hettstedt
1999	Abitur

Studium

10/2000 - 10/2006	Studium der Medizinischen Physik an der Martin-Luther-Universität Halle-Wittenberg
10/2002	Vordiplom
08/2005 - 07/2006	Diplomarbeit: *„Einzelmolekül-Immunofluoreszenz mit evaneszenter Anregung“*
10/2006	Abschluß Diplom Physiker

Promotion

seit 05/2007	Promotion am Lehrstuhl für Experimentelle Physik I der Universität Leipzig
seit 05/2007	Mitglied im Graduiertenkolleg „InterNeuro“ der Universität Leipzig